UNIVERSITEIT
GENT

Faculteit Wetenschappen
Vakgroep Subatomaire en Stralingsfysica

Neutron induced reactions on ^{26}Al, ^{36}Cl and ^{41}Ca and their astrophysical implications

Liesbeth De Smet

Proefschrift ingediend tot het behalen van de graad van
Doctor in de Wetenschappen: Natuurkunde
Promotor: Prof. Dr. C. Wagemans

Academiejaar 2005-2006

Neutron induced reactions on ^{26}Al, ^{36}Cl and ^{41}Ca and their astrophysical implications

Cover illustration by Sarah Pillen

The measurements of this thesis were performed at the GELINA facility of the Institute for Reference Materials and Measurements (EC-JRC-IRMM) in Geel, Belgium.

UNIVERSITEIT
GENT

Faculteit Wetenschappen
Vakgroep Subatomaire en Stralingsfysica

Neutron induced reactions on ^{26}Al, ^{36}Cl and ^{41}Ca and their astrophysical implications

Liesbeth De Smet

Proefschrift ingediend tot het behalen van de graad van
Doctor in de Wetenschappen: Natuurkunde
Promotor: Prof. Dr. C. Wagemans

Academiejaar 2005-2006

Samenstelling examencommissie:

Prof. Dr. F. Callens	UGent, voorzitter
Prof. Dr. C. Wagemans	UGent, promotor (leescommissie)
Dr. P. Geltenbort	ILL Grenoble (leescommissie)
Dr. Ir. J. Heyse	IRMM Geel (leescommissie)
Prof. Dr. D. De Frenne	UGent (leescommissie)
Prof. Dr. K. Heyde	UGent
Prof. Dr. E. Jacobs	UGent

Ik loop door de jaren
Langs een eindeloos strand
En ik probeer te verklaren
Hoe ik hier ben beland
Hoe sterk is het toeval
Hoe sterk is het lot
Ben ik wie ik zijn wou
Is het dat wat ik zocht

Liedtekst uit ‘Witsand’
CD ‘Van Mpumalanga Tot Die Kaap’
Stef Bos, 2001.

Dankwoord

... Hoe ben ik hier beland ... Is het dit wat ik zocht ...

Ontelbare keren heb ik het me afgevraagd, vooral in het begin, nu iets meer dan 4 jaar geleden. Beetje bij beetje maakte de twijfel - ongemerkt bijna - plaats voor vertrouwen en enthousiasme. Dit was en is niet enkel mijn verdienste. De afgelopen 4 jaar heb ik het geluk gehad met verschillende mensen te mogen samenwerken. Zij hebben allen een belangrijke bijdrage geleverd, niet alleen aan dit eindwerk, maar ook aan mijn vorming. Ik wil dan ook graag een aantal mensen bedanken die me zijn gevolgd tijdens dit avontuur.

Eerst en vooral mijn promotor, Professor Cyriel Wagemans. Beste Cyriel, ik mocht als doctoraatstudent met je samenwerken, je hebt me binnengeloodsd en begeleid in de wereld van de experimentele fysica die ik ongedwongen mocht ontdekken. Het was niet altijd makkelijk voor me om met die vrijheid om te gaan en m'n eigen weg te zoeken. Waarschijnlijk zal ik pas later de waarde daarvan goed kunnen inschatten. Toch wist ik dat ik steeds bij jou kon binnenlopen als dat nodig was. Cyriel, bedankt voor je vertrouwen.

Als tweede wil ik Jan Heyse - zeg maar mijn begeleider voor de laatste 3 jaar, bedanken. Jan, ik heb je veel vragen gesteld en altijd een antwoord gekregen. Telkens als ik niet meer wist hoe het verder moest, kon ik bij jou terecht. Je gaf me nieuwe ideeën en heel veel van wat in deze thesis staat is samen met jou tot stand gekomen. Jan, ik heb zo veel van jou geleerd, zonder jou was het niet gelukt !

Ik mag zeker mijn bureaugenote - Sofie Vermote - niet vergeten in mijn lijstje. Sofie, je zorgde voor de ochtendbabbel. En de middagbabbel en de av... Het zijn die momenten die het leuk maken om te komen 'werken'. Tijdens mijn laatste maanden heb ik veel gezaagd en geklaagd, maar toch bleef je me opbeuren en stimuleren, je leek wel een eindeloos vat geduld. Sofie, bedankt omdat je er was en luisterde op die momenten wanneer ik het eventjes moeilijk had.

De eerste weken als 'groentje' werd ik 'opgevangen' door Gert Goeminne. Beste Gert, je hebt me niet enkel geholpen bij het begin van mijn doctoraat, maar je hebt me ook één van de belangrijkste levenswijsheden bijgebracht. Ik heb van jou geleerd me de tijd te gunnen en de tijd te nemen om me aan te passen aan iets nieuws. Het heeft me geholpen niet meer te verlangen naar vroeger.

Ook onze technieker, Jack Van Gils verdient een pluim. Beste Jack, je hebt me wegwijs gemaakt in al die vreemde elektronica en data acquisitie-toestanden. Wanneer iets moest opgesteld worden of wanneer er iets fout ging, stond je onmiddellijk klaar om te helpen. Ik bewonder nog steeds je manier van werken: rustig en uiterst secuur. Ik hoop dit in m'n verdere 'carrière' met me mee te kunnen nemen en aan anderen door te geven. Ik vergeet ook niet onze eindeloze praatjes over de sportgebeurtenissen. Toch iemand met wie ik kon discussiëren daarover ... En Jack: Justine Henin is gewoonweg de beste.

Hoewel ik 'niet van het IRMM' was, maar een langdurige bezoeker, heb ik nooit het gevoel gehad er niet bij te horen. Ik bedank graag Peter Rullhusen en iedereen van de Neutron Physics Unit om mij in hun groep op te nemen. Peter Siegler, Peter Schillebeeckx en Arjan Plompen, bedankt voor het beantwoorden van mijn talloze vragen. Ook een welgemeend dankjewel aan Wim Mondelaers en alle operatoren van GELINA, het is evident - waardoor het soms wel 'ns vergeten wordt - dat dit werk er zonder jullie niet was gekomen. Wanneer mijn 'stupid miserable device' van een computer niet meer deed wat ik wou, waren er gelukkig nog de mensen van de helpdesk, bedankt voor al die keren dat jullie me uit de nood hebben geholpen.

En wat zou een mens zijn zonder mensen om zich heen? Sofie, Jan, Alessandro, Ann, Marek, Peter, Raffaella, Christian, Gert, Jan, Ruud, Peter, Nina en Costa, jullie maakten mijn verblijf in dit 'boerengat' meer dan de moeite waard. Bedankt iedereen !

Ook Sarah Pillen wil ik hier nog hartelijk bedanken. Sarah, als kunstenaar heb jij het aangedurfd een wetenschapper te begrijpen. Het resultaat pronkt op de voorpagina van dit werk. Bedankt voor je tijd en inspiratie om voor mij die originele collage te maken. Het is uiteindelijk geworden wat ik wou.

Tot slot zijn er nog mijn ouders en zus. Mama, papa en Ann bedankt voor de steun en wijze raad. Jullie hebben me de vrijheid gegeven om m'n eigen keuzes te maken. Ik wist dat ik altijd welkom was en ben in Hotel Myrakee waar ik als een prinses in de watten wordt gelegd en aan niets meer hoef te denken. Die ene tegenslag heeft ons de zin van het leven doen inzien en mama ik ben zo blij dat jij er nog bent en dit samen met ons mag vieren.

Liesbeth.

Table of contents

Introduction

For ages people have been gazing towards the firmament. They were and are amazed and at the same time a lot of questions arise. It's typical for human beings that we want to understand and explain the things around us and in this way the legends and myths originated. For a long time it was a prevailing cultural belief that the heavens represented a perfect and therefore unchangeable creation by God. The only apparent change in the sky, the movement of the planets, was described by perfect cyclic motions, which have no start nor end. Only on the imperfect Earth change was permitted. Later on, theories explained the motion of the planets and measuring instruments were invented so that little by little and bit by bit more and more was explained. But every answer gave rise to new questions. We wanted to understand how the Sun and other stars shine and how they live their life. A related problem as well as one of the principal challenges of nuclear astrophysics is to understand the nuclear processes which produced the relative abundances of the elements and their isotopes in nature. It is only half a century ago that this age-old question of how the elements are generated was explained. In their famous paper *Synthesis of the Elements in Stars* of 1957, Burbidge, Burbidge, Fowler and Hoyle [Bur57] and independent of them Cameron [Cam57] laid out the framework of our understanding of the formation of the heavy elements: the majority of the chemical elements is produced through nuclear reactions in the hot interiors of stars.

Although nowadays the nucleosynthesis of most of the isotopes is taken as common knowledge, the origin of some isotopes is not yet clear. In this work, the problem about how and where the light isotopes ^{36}S and ^{26}Al are generated and subsequently destructed is highlighted. To determine their origin, nucleosynthesis calculations are necessary for which accurate cross section data for the reactions involved are required. For the origin of ^{36}S, improved cross section data on the ^{36}Cl(n,p)^{36}S and ^{36}Cl(n,α)^{33}P reactions are determined. The ^{36}Cl(n,p) reaction leads immediately to ^{36}S and therefore influences its abundance in a direct way. On the other hand, ^{36}Cl(n,α) causes a recycling to ^{33}P, which undergoes β^--decay to ^{33}S, which can still form ^{36}S through

successive n-captures. A third investigated reaction of importance for the ^{36}S origin is ^{41}Ca(n,α)^{38}Ar. ^{38}Ar may capture a neutron and form ^{39}Ar, the (n,α) branching at ^{39}Ar directly influences the ^{36}S production.
A second hot topic in astrophysics nowadays is the nucleosynthesis of radioactive ^{26}Al in our Galaxy, because it may give information on galactic evolution, on the birth of the solar system and on stellar nucleosynthesis. Many different stellar sites have been proposed as the birthplace of ^{26}Al. However, for a good understanding of the observed abundance, the destruction mechanisms have to be known. In this respect, the (n,p) and (n,α) reactions are key reactions and for that reason a good knowledge of the neutron induced reactions on ^{26}Al is very important. In this work the ^{26}Al(n,α)^{23}Na reaction is investigated.

As mentioned, in this work only neutron induced reactions on light nuclei are investigated. Although nuclides up to iron are produced in thermonuclear reactions, neutron induced reactions, responsible for the production of the elements beyond iron, are of importance to explain the abundance of some light neutron rich isotopes like ^{36}S, which are bypassed by the thermonuclear reactions. The measurements are performed at the linear electron accelerator GELINA of the IRMM in Geel, Belgium. In addition to the astrophysical relevance of the studied reactions, it is attempted to obtain nuclear physics information as resonance energy, partial and total level widths and spin of the excited state.

Therefore, the main aspects of neutron induced charged particle reactions are considered in chapter 1. Their typical resonant behaviour is treated in the framework of the compound nucleus theory. Chapter 1 is concluded with the introduction of the concept of Maxwellian Averaged Cross Section or MACS, of importance for the astrophysical part of this work.

The astrophysical relevance of the reactions investigated in this work is highlighted in chapter 2 after a short description of the stellar nucleosynthesis. Special attention is given to the s-process mechanism and to sites which are of interest in the search for the origin of ^{36}S. A second interesting astrophysical topic in this work is the origin and destruction of radioactive ^{26}Al in our Galaxy. This needs a detailed discussion of the working of Asymptotic Giant Branch or AGB stars and the nucleosynthesis in such stars.

In a second part, the main subject of the present work is discussed: (n,p) and (n,α) reactions on ^{26}Al, ^{36}Cl and ^{41}Ca as a function of the neutron energy. It has been mentioned already that the studies of these reactions are performed at the GELINA time-of-flight (TOF) facility of the IRMM. Starting from the GELINA properties, the following subjects for the experimental setup are scrutinized in chapter 3: the detection system used and its tuning, the data acquisition system and the TOF-technique, the data reduction to obtain cross sections as a function of the neutron energy and finally the neutron energy resolution. A prerequisite to perform cross section measurements is the availability of a sample. The preparation and mass determination of the samples used conclude the experimental setup chapter.

The last three chapters present the results for the ^{26}Al(n,α), ^{36}Cl(n,p), ^{36}Cl(n,α) and ^{41}Ca(n,α) measurements. In chapter 4 the data analysis to obtain differential cross sections as a function of the neutron energy is given in detail for the ^{26}Al(n,α)^{23}Na measurement. The energy position, the area and the total natural line width of the resonances of the compound nucleus are extracted from the obtained differential cross section through a fit and are compared with values taken from literature. However, the spin and the partial level widths of the levels could not be determined. To calculate them, additional information on the levels in the compound nucleus has to be known. They can be obtained through a total cross section measurement and through measurements leading to the same compound nucleus, e.g. ^{26}Al(n,γ)^{27}Al ^{26}Al(n,p)^{26}Mg or the inverse reactions. As this information was not available, the spin nor the partial level widths could be calculated. To conclude chapter 4, the astrophysical implications of the obtained cross section data are presented. Firstly, the MACS values are calculated by numerical integration. They are compared with other experimental values and with theoretical values. The impact of these improved MACS values on the destruction of ^{26}Al formed in our Galaxy finalizes chapter 4.

The same subjects are discussed in chapters 5 and 6 for the ^{36}Cl(n,p) + ^{36}Cl(n,α) and ^{41}Ca(n,α) measurements, respectively. These measurements are important in the quest for the origin of ^{36}S. The influence of the new MACS values for the ^{36}Cl measurements on the abundance of ^{36}S is discussed in detail at the end of chapter 6. As the ^{41}Ca(n,α) measurement is the only experimental result reported up to now and as a complementary measurement will be performed on a longer flight path at GELINA, the calculated MACS values are not yet used in astrophysical network calculations. Therefore, no discussion is given on the impact of the new MACS values on the origin of ^{36}S. Besides the importance in the search for the origin of ^{36}S, the recycling of ^{41}Ca towards ^{38}Ar is important for two other astrophysical implications. Firstly, the (n,α) branching at ^{41}Ca has its influence in explaining the solar ^{46,48}Ca abundances or the correlated isotopic Ca-Ti-Cr anomalies observed in inclusions of the Allende meteorite. This topic is not highlighted in this work. Secondly, the recycling of ^{41}Ca towards ^{38}Ar is important in dating the age of the chemical elements. A short description of the ^{40}K cosmic clock is given at the end of chapter 6.

Finally, some conclusions and an outlook finalize this work on neutron induced reactions on ^{26}Al, ^{36}Cl and ^{41}Ca.

Part I

Theoretical background

Chapter 1

Nuclear physics

1.1 Neutron induced reactions

1.1.1 The neutron

Around 1920 it was believed that all nuclei were built out of protons and ‘neutral doublets’ formed from closely bound protons and electrons. This ‘neutral doublet’ - called neutron by Ernest Rutherford - would be uncharged but with a mass slightly greater than the proton. This could explain both the mass and the charge that had been measured for different nuclei. Because this neutral doublet was uncharged, there would be no electrical repulsion of the ‘neutron’ when it passed through matter, making it difficult to detect.

It took until 1932 before James Chadwick finally found experimental evidence of the neutron, following discoveries made by Walter Bothe and Herbert Becker in Germany and Irène and Frédéric Joliot-Curie in France [neu, Gri03, Rho86].

Bothe and Becker found in 1930 that beryllium exposed to α-particles emitted a neutral radiation, which they assumed to be high-energy γ-rays.

In 1932 Irène and Frédéric Joliot-Curie put a block of paraffin wax behind the beryllium sample. They found that protons are emitted when the radiation hitted the paraffin. By measuring the speed of the emitted protons, they could calculate that the γ-rays would have to be incredibly energetic to knock the protons out of the paraffin.

Chadwick and Rutherford did not believe that γ-rays could account for the protons from the paraffin. They were convinced that the beryllium was emitting neutrons, which could knock protons out of the beryllium very easily because they have nearly the same mass as protons. Chadwick found that the paraffin could be replaced with other light substances like helium, lithium, beryllium, boron, carbon, nitrogen and hydrogen. In each case, the powerful 'beryllium radiation' knocked about the same amount of protons out of each element. If this beryllium radiation consisted of γ-rays, increasing foton energy would be needed as the mass of the struck atoms increases. He found that γ-rays could not explain the energy of the protons and the only good explanation for his result was a neutral particle. To prove that the particle was indeed the neutron, Chadwick calculated its mass on the basis of an experiment with boron as a target. It was slightly bigger than the mass of a proton, proving the neutral radiation was indeed the long-sought neutron.

But if that neutron indeed consists of a proton and an electron, then hydrogen atoms should sometimes turn into neutrons. However, Chadwick learned, while trying to find the neutron, that it was very difficult to make neutrons out of protons and electrons. His findings were quickly accepted and Werner Heisenberg then showed that the neutron could not be a proton-electron pairing, but had to be its own unique particle. Finally, he concluded that the atomic nucleus was made out of protons and neutrons and all of the electrons in the atom were outside the nucleus.

This new idea dramatically changed the picture of the atom and accelerated discoveries in nuclear physics. Physicists soon realized that the neutron was an ideal 'bullet' for bombarding other nuclei. Unlike charged particles, it was not repelled by nuclear charges and could therefore probe the nucleus.

Nowadays, the Standard Model catalogues the neutron as a baryon, composed of 3 quarks: 1 u (up) and 2 d (down).

An in depth discussion about the discovery of the neutron can be found in [Rho86].

1.1.2 Compound nucleus reactions

In nuclear physics, the concept of 'cross section' is important. It is a measure for the probability that a projectile interacts with a nucleus. This probability is used to determine how many reactions occur per unit time and unit volume and hence, provides important information on energy production in stars.

In this work neutron induced charged particle reactions, i.e. (n,p) and (n,α), are studied on low mass nuclei in the neutron energy range from some eV up to a few 100 keV. The resulting reaction cross section as a function

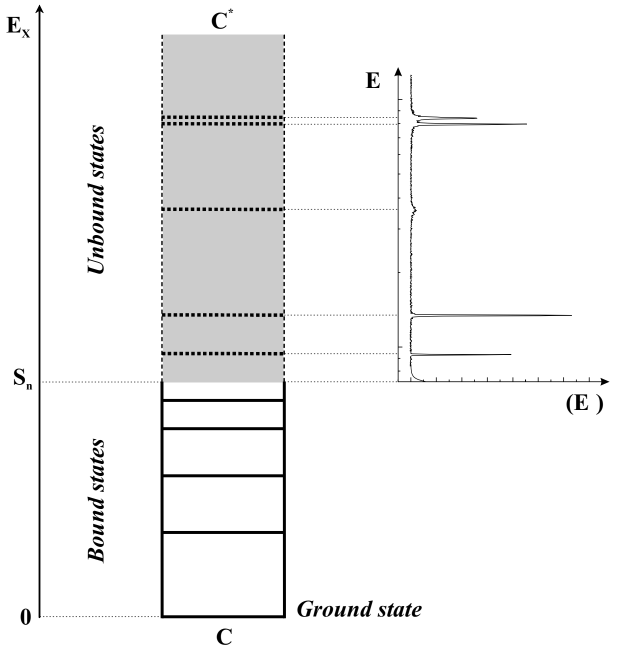

Figure 1.1: Schematic view of the compound nucleus formed after interaction of a neutron with a target nucleus. The dashed levels represent the excited states of the system 'neutron + nucleus' (expanded scale).

of neutron energy is characterized by a resonance structure. To explain this energy dependence, Niels Bohr proposed the compound nucleus model in 1936 [Boh36]. Nuclear reactions are explained as a two-stage process consisting of the formation of a relatively long-lived intermediate nucleus C (in an excited state C^*) and its subsequent decay:

$$X + n \longrightarrow C^* \longrightarrow Y + b. \tag{1.1}$$

First, the incident neutron, with kinetic energy E_n, interacts with the target nucleus X with mass number A and forms the so-called compound nucleus with atomic mass A+1. The neutron shares its energy with the other nucleons and becomes part of a new, highly excited unstable nucleus, represented by C^*. The excitation energy E_x of this compound nucleus is equal to the neutron separation energy S_n increased with the kinetic energy E_μ of the incident neutron in the center of mass (COM) system (see figure 1.1):

$$E_x = S_n + E_\mu. \tag{1.2}$$

In the second step, after a relatively long period of time (10^{-19} - 10^{-15} s) [Ber04], the compound nucleus decays through different possible exit channels. In Bohr's assumption the compound nucleus lives long enough to 'forget' the way in which it was formed and the deexcitation to the final products only depends on the energy, angular momentum and parity of the quantum state of the compound nucleus. Or, in other words, the break-up of the compound nucleus through different exit channels is only dependent on the properties of the compound nucleus and not on its formation mode.

As a consequence of this independence hypothesis, the reaction cross section of the reaction X(n,b)Y can be written as:

$$\sigma(n,b) = \sigma_{CN}(n,X)P(b), \tag{1.3}$$

with $\sigma_{CN}(n,X)$ the cross section for the formation of the compound nucleus C^* from projectile n and target X and $P(b)$ the probability that the formed compound nucleus emits a particle b, leaving a residual nucleus Y.

Another particularity about compound nucleus reactions is that the emitted particles should have an isotropic angular distribution in the COM system.

The resonances in the reaction cross section can now be considered as excited levels of the compound nucleus, which are unbound states with a relatively long lifetime τ (see figure 1.1). Such a quasi-bound level has a level width Γ corresponding with the uncertainty on the level energy ΔE. Making use of Heisenberg's uncertainty principle, τ and Γ are correlated:

$$\Delta E \Delta t = \Gamma\tau \approx \hbar. \tag{1.4}$$

Because a level can decay through different channels, the total level width Γ is the sum of the partial level widths Γ_i [Ber04]:

$$\Gamma = \sum_i \Gamma_i, \tag{1.5}$$

where equation 1.4 is also valid for the partial level widths:

$$\Gamma_i \tau_i \approx \hbar. \tag{1.6}$$

The probability $P(b)$ in equation 1.3 can now be replaced by $\frac{\Gamma_b}{\Gamma}$:

$$\sigma(n,b) = \sigma_{CN}(n,X)\frac{\Gamma_b}{\Gamma}, \tag{1.7}$$

and only an expression for $\sigma_{CN}(n,X)$ is needed to describe the resonant behaviour of the cross section.

1.1.3 The Breit-Wigner formula

A particular level with mean energy E_{res} and width Γ can be represented by a wave function of the form [Bur63, Eva55, Sat90]:

$$\begin{aligned} \psi &= \psi_0\, e^{-\frac{\Gamma t}{2\hbar}}\, e^{-i\frac{E_{res}t}{\hbar}} \\ &= \psi_0\, e^{-\frac{i}{\hbar}E't}, \end{aligned} \tag{1.8}$$

with $E' = E_{res} - i\frac{\Gamma}{2}$ and ψ_0 independent of time. The lifetime τ of the level is $\hbar/\Gamma$ and the probability of finding this compound state at time t is given by:

$$|\psi|^2 = |\psi_0|^2\, e^{-\frac{t}{\tau}}. \tag{1.9}$$

The wave function (1.8) is not a stationary state, but may be built up of a superposition of stationary states with different energies E spread around E_{res} and can be expressed as a Fourier integral [Bur63]:

$$\psi\left(\frac{t}{\hbar}\right) = \int_{-\infty}^{+\infty} B(E)\, e^{-iE\frac{t}{\hbar}}\, dE, \tag{1.10}$$

where $B(E)$ is the amplitude of the state with energy E. The probability of finding the energy E in the state ψ or in other words the cross section for the formation of the compound nucleus $\sigma_{CN}(n,X)$ in the resonant state with energy E is now proportional to $|B(E)|^2$. By inversion of equation 1.10 and assuming that the energy range is going from 0 to ∞, $B(E)$ becomes:

$$\begin{aligned} B(E) &= \frac{1}{2\pi}\int_0^{+\infty} \psi\left(\frac{t}{\hbar}\right) e^{i\frac{t}{\hbar}E}\, \frac{dt}{\hbar} \\ &= \frac{\psi_0}{2\pi}\int_0^{+\infty} e^{\left(-iE_{res}+iE-\frac{\Gamma}{2}\right)\frac{t}{\hbar}}\, \frac{dt}{\hbar} \end{aligned}$$

$$\begin{aligned} &= -\frac{\psi_0}{2\pi}\,\frac{1}{i(E-E_{res})-\frac{\Gamma}{2}} \\ \Rightarrow |B(E)|^2 &= \frac{\psi_0^2}{4\pi^2}\,\frac{1}{(E-E_{res})^2+\left(\frac{\Gamma}{2}\right)^2} \\ \Rightarrow \sigma_{CN}(n,X) &= \frac{C}{(E-E_{res})^2+\left(\frac{\Gamma}{2}\right)^2}. \end{aligned} \tag{1.11}$$

Based on statistical arguments, it may be proven [Bur63, Sat90] that C becomes:

$$C = \pi\frac{\Gamma_n\Gamma}{k^2}, \tag{1.12}$$

with k the wave number, related to the neutron momentum p via:

$$p = \hbar k. \tag{1.13}$$

Combination of equations 1.7, 1.11 and 1.12 eventually leads to an expression for the reaction cross section of the reaction X(n,b)Y with formation of a compound nucleus:

$$\begin{aligned} \sigma(n,b) &= \frac{\pi}{k^2}\,g\,\frac{\Gamma_n\Gamma}{(E_n-E_{res})^2+\left(\frac{\Gamma}{2}\right)^2}\,\frac{\Gamma_b}{\Gamma} \\ &= \frac{\pi}{k^2}\,g\,\frac{\Gamma_n\Gamma_b}{(E_n-E_{res})^2+\left(\frac{\Gamma}{2}\right)^2}. \end{aligned} \tag{1.14}$$

This expression is known as the Breit-Wigner expression for a resonant cross section. To take into account the contribution of the different spins of the particles, the cross section 1.14 contains the statistical factor g:

$$g = \frac{2J+1}{(2s+1)(2I+1)}, \tag{1.15}$$

with J the total angular momentum of the compound nucleus, formed by the target spin I and the neutron with spin s and orbital angular momentum ℓ:

$$\vec{J} = \vec{s} + \vec{\ell} + \vec{I}. \tag{1.16}$$

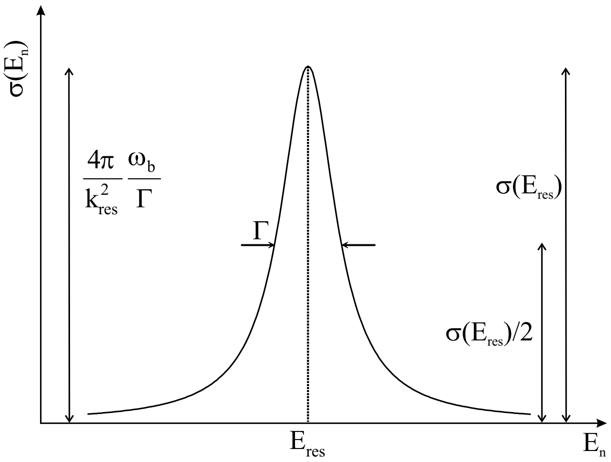

Figure 1.2: A Breit-Wigner shape is characterized by three parameters: the resonance energy at peak position E_{res}, the full width at half maximum represented by the total resonance width Γ and the resonance area A_{res}.

1.1.4 Properties of neutron induced reactions

For the reactions studied in this work, four different partial widths Γ_b are possible: Γ_n, Γ_γ, Γ_p and Γ_α, in which the compound nucleus emits respectively a neutron with the same energy as the incident neutron, one or more γ-rays, a proton or a α-particle.

The maximum cross section in equation 1.14 is obtained at $E_n = E_{res}$:

$$\begin{aligned} \sigma_{max} &= \frac{4\pi}{k^2}\, g\, \frac{\Gamma_n \Gamma_b}{\Gamma^2} \\ &= \frac{4\pi}{k^2}\, \frac{\omega_b}{\Gamma}, \qquad (1.17) \\ & \qquad\qquad\qquad (1.18) \end{aligned}$$

with ω_b the resonance strength.

By replacing E_n with $E_{res} \pm \frac{\Gamma}{2}$ in equation 1.14, $\sigma(n,b)$ falls to half maximum, which means that Γ represents the full width at half maximum (FWHM) (see figure 1.2).

The area under a resonance can be calculated by integration of equation 1.14. Assuming that partial and total level widths are energy independent, the area becomes:

$$\begin{aligned} A_{res} &= \frac{\pi}{k_{res}^2}\, g\, \Gamma_n\, \Gamma_b \int\limits_0^{+\infty} \frac{1}{(E_n - E_{res})^2 + \left(\frac{\Gamma}{2}\right)^2} dE_n \\ &= \frac{\pi}{k_{res}^2}\, g\, \Gamma_n\, \Gamma_b\, \frac{\pi}{\frac{\Gamma}{2}} \\ &= 2\left(\frac{\pi}{k_{res}}\right)^2 g\, \frac{\Gamma_n \Gamma_b}{\Gamma} \\ &= 2\left(\frac{\pi}{k_{res}}\right)^2 \omega_b; \end{aligned} \tag{1.19}$$

k_{res} can be calculated as follows [Mac65]:

$$k_{res}^2 \left[\frac{1}{b}\right] = 4.826 \times 10^{-6}\, E_{res}\, [eV]. \tag{1.20}$$

In this calculation of the area, the neutron width Γ_n was taken to be independent of the neutron energy. This is only true in the neighbourhood of a resonance. To use the Breit-Wigner formula for broader energy intervals, the penetrability through the centrifugal barrier, determined by the orbital momentum of the neutron, has to be taken into account. The energy dependence of Γ_n can then be expressed as [Frö00, Mug81]:

$$\Gamma_n(E_n) = \Gamma_n^{\ell}\, \frac{P_\ell}{ka_c} \sqrt{\frac{E_n}{1\, eV}}, \tag{1.21}$$

with Γ_n^ℓ the reduced neutron width, P_ℓ the penetration factor as a function of the channel radius a_c and the wave number k, which is energy dependent. The penetration factor for $\ell = 0$, 1 and 2 is listed as a function of ka_c in [Frö00, Mug81]. For $\ell = 0$ or s-wave neutrons $P_0 = ka_c$ and $\Gamma_n(E_n)$ becomes:

$$\Gamma_n(E_n) = \Gamma_n^0 \sqrt{\frac{E_n}{1\, eV}} \sim v. \tag{1.22}$$

For p-wave (ℓ=1) neutrons $P_1 = \frac{(ka_c)^3}{1+(ka_c)^2}$, leading to:

$$\Gamma_n(E_n) = \Gamma_n^1 \sqrt{\frac{E_n}{1\, eV}} \left(1 + \frac{11369}{A^{2/3} \frac{E_n}{1000}}\right)^{-1}. \tag{1.23}$$

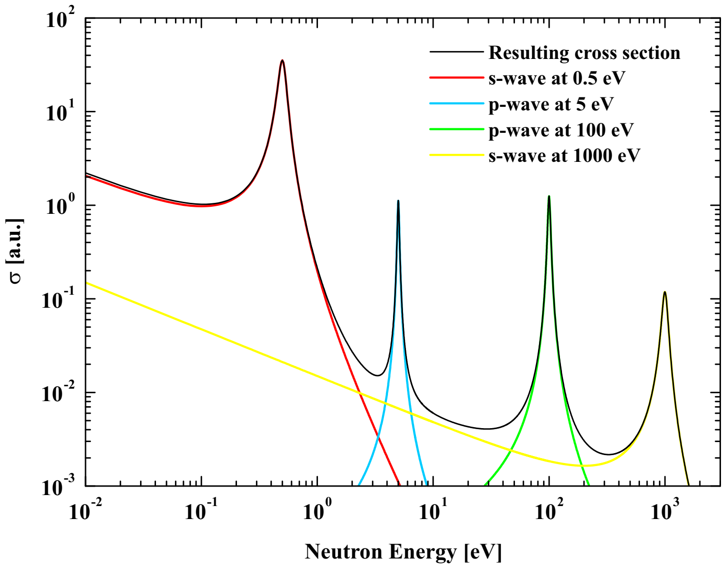

Figure 1.3: Cross section formed by four Breit-Wigner shapes with arbitrary resonance parameters. Two of the four resonances are s-wave resonances, while the other two are p-wave. The thermal cross section at 0.0253 eV is composed of the tails of the two s-wave resonances.

Higher neutron waves are neglected in the neutron energy range covered in this work because the penetrabilities for larger ℓ-values are too small.

At low energies $(E_n - E_{res})^2 >> \left(\frac{\Gamma}{2}\right)^2$. In the case of s-wave neutrons and by substituting formula 1.22 into formula 1.14, the neutron cross section σ shows the well-known $\frac{1}{v}$-behaviour for low neutron energies ($k^2 \sim v^2$). On the other hand, for p-wave neutrons, formula 1.23 has to be substituted into formula 1.14 and for low neutron energies the cross section σ is proportional to v. Consequently, p-wave neutrons have no contribution at low neutron energies.

Figure 1.3 shows the Breit-Wigner expression for four different sets of arbitrary resonance parameters. It illustrates that for low energies, only s-wave resonances show the $\frac{1}{v}$-shape.

A widely used reference point in neutron physics is the neutron cross section at thermal energy E_n = 0.0253 eV (at T = 293.6 K). It is clear from figure 1.3 and formula 1.22 that the thermal cross section is composed of the $\frac{1}{v}$-tails of the different s-wave resonances. On the other hand, figure 1.3 and formula 1.23 show that p-wave resonances do not contribute to the thermal cross section. With the help of formulas 1.14, 1.19, 1.20 and 1.22, the contribution of s-wave resonances to the cross section at thermal energy can be calculated and is approximately given by:

$$\begin{aligned}\sigma(E_{th})[b] &= 4.099 \times 10^6 \, \frac{g\,\Gamma_n^0\,\Gamma_b}{E_{res}^2} \\ &= \frac{1}{2\pi\sqrt{E_{th}}}\frac{\Gamma_{res}\,A_{res}}{E_{res}^{3/2}} \\ &\sim \frac{\Gamma_{res}\,A_{res}}{E_{res}^{3/2}}, \end{aligned} \tag{1.24}$$

with Γ_{res}, E_{res} and E_{th} in eV and A_{res} in b.eV.

1.1.5 Resonance parameters

The experimental neutron induced reaction cross section can be parameterized with resonance parameters. A resonance is characterized by the resonance energy E_{res}, the total natural line width Γ, the partial widths Γ_b, the spin of the state J and the orbital momentum of the incoming neutron ℓ. A resonance analysis aims at determining these parameters. As a first step to obtain them, the experimental data can be fitted with a Breit-Wigner curve. Such a Breit-Wigner shape is characterized by three fit parameters: the resonance energy E_{res}, the full width at half maximum represented by the total resonance width Γ and the resonance area via the resonance strength ω_b. An example of a Breit-Wigner curve is shown in figure 1.2. Experiments on other nuclei with different entrance or exit channels, leading to the same compound nucleus provide additional information on Γ_b, J and ℓ. These values together with the values of the Breit-Wigner fit can be used in a second step to determine the remaining resonance parameters. They can be extracted from the experimental data using Resonance Shape Analysis (RSA) codes, such as REFIT [Mox91] or SAMMY [Lar03], which are based on multi-level R-matrix reaction theory [Lan58].

1.2 The Maxwellian Averaged Cross Section

The concept of 'Maxwellian Averaged Cross Section' or MACS has to be introduced for the astrophysical part of this work.

The reaction rate is defined as the number of reactions per projectile-target nucleus pair and per second. It can be calculated from the measured cross section by folding it with the velocity distribution of the reacting particles:

$$\langle \sigma v \rangle = \int_0^{+\infty} \sigma(v)\, v\, \varphi(v)\, dv, \tag{1.25}$$

where $\varphi(v)dv$ represents the velocity distribution or the probability that the relative velocity v between the projectile and the target nucleus has a value between v and $v + dv$. The total reaction rate r is given by:

$$r = N_A N_n \langle \sigma v \rangle, \tag{1.26}$$

with N_A and N_n the total number of target nuclei and projectiles (neutrons in this work) per cm^3, respectively.

In the stellar conditions relevant for this work (s-process, see chapter 2) the stellar gas is not degenerated, is in thermodynamic equilibrium and the nuclei move non-relativistically. The relative velocity between the neutrons and the target nuclei then complies with the Maxwell Boltzmann velocity distribution [Rol88]:

$$\varphi(v) = 4\pi v^2 \left(\frac{\mu}{2\pi kT}\right)^{\frac{3}{2}} e^{-\left(\frac{\mu v^2}{2kT}\right)}, \tag{1.27}$$

with k the Boltzmann constant and μ the reduced mass $\mu = \frac{m_A m_n}{m_A + m_n}$, where m_n and m_A are the mass of the neutron and target nucleus, respectively.

In s-process nucleosynthesis it is common to define a Maxwellian Averaged Cross Section (MACS) by deviding the reaction rate by the mean velocity $v_T = \sqrt{\frac{2kT}{\mu}}$ at temperature T:

$$\langle \sigma \rangle = \frac{\langle \sigma v \rangle}{v_T} = \frac{\mu^2}{\sqrt{\pi}} \frac{1}{(kT)^2} \int_0^{+\infty} \sigma(v)\, v^3 e^{-\frac{\mu v^2}{2kT}}\, dv. \tag{1.28}$$

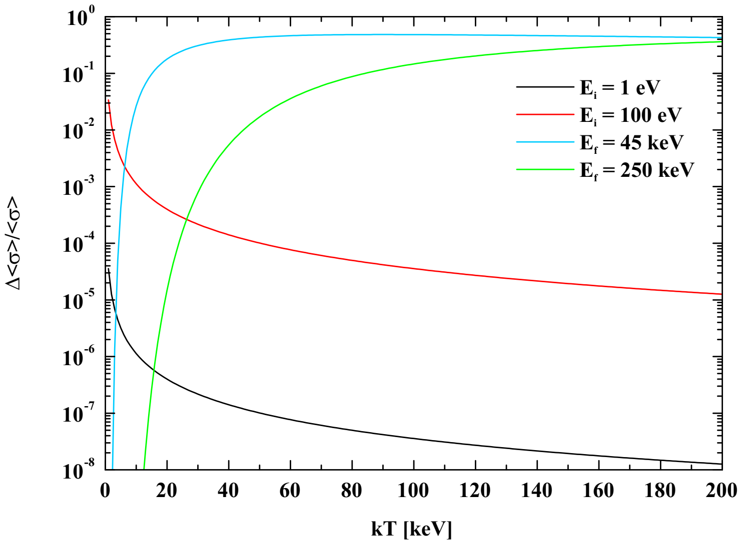

Figure 1.4: Uncertainties on the MACS as a result of the experimental energy limits as a function of kT. Two different lower and upper limits are chosen, the upper limits are relevant for this work.

Making use of the center of mass neutron energy $E_\mu = \frac{1}{2}\mu v^2$, the MACS can be written as a function of the center of mass neutron energy:

$$\langle\sigma\rangle = \frac{2}{\sqrt{\pi}} \frac{1}{(kT)^2} \int\limits_0^{+\infty} \sigma(E_\mu)\, E_\mu\, e^{-\frac{E_\mu}{kT}}\, dE_\mu. \tag{1.29}$$

However, the cross section from zero to infinite energy is not available. By taking a finite energy interval, imposed by the energy limits of the experiment, the integration (1.29) can be calculated numerically for a certain temperature kT. By doing so, the limited integration zone gives rise to systematic uncertainties in the calculated MACS. Beer *et al.* [Bee92] estimated these uncertainties arising from the chosen values for the lower (E_i) and upper (E_f) integration limit:

$$\left(\frac{\Delta\langle\sigma\rangle}{\langle\sigma\rangle}\right)_{E_i} \quad \leq \quad \frac{2}{\sqrt{\pi}}\sqrt{\frac{E_i}{kT}}\left(1 - e^{-\frac{E_i}{kT}}\right) \tag{1.30}$$

$$\left(\frac{\Delta\langle\sigma\rangle}{\langle\sigma\rangle}\right)_{E_f} = \frac{2}{\sqrt{\pi}}\sqrt{\frac{E_f}{kT}}\,e^{-\frac{E_f}{kT}}. \tag{1.31}$$

In figure 1.4 both uncertainties are plotted as a function of the temperature kT. It shows that the uncertainty introduced by the upper energy limit dominates almost the whole temperature interval.Besides, the figure demonstrates that the total uncertainty due to the limited energy interval is lower when the upper energy limit is higher. Therefore, it is important to know the cross section in a broad energy interval.

If the widths of the resonances in the measured cross section are much smaller than the kT-value, the resonances can be described as Dirac δ-functions. The integral in formula 1.29 can then be replaced by a sum over the areas for all the observed resonances:

$$\langle\sigma\rangle_{res} = \frac{2}{\sqrt{\pi}}\,\frac{1}{(kT)^2}\sum_{res} A_{res}\,E_{res}\,e^{-\frac{E_{res}}{kT}}, \tag{1.32}$$

with kT in eV, A_{res} in b.eV and E_{res} the laboratory resonance energy in eV. The areas can be calculated from the resonance parameters (see sections 1.1.4 and 1.1.5). To include the contribution of the $\frac{1}{v}$-component at low energies, originating from the tails of the s-wave resonances (see section 1.1.4), a second term has to be added to the resonance part. It can be calculated on the basis of the thermal velocity v_{th}:

$$v_{th} = \sqrt{\frac{2\times 0.0253\,eV}{\mu}}. \tag{1.33}$$

The cross section $\sigma(v)$ in formula 1.28 can now be replaced by:

$$\sigma(v) = \frac{\sigma_{th}\,v_{th}}{v}. \tag{1.34}$$

Making use of $\int\limits_0^{+\infty}\sqrt{x}\,e^{-x}dx = \frac{\sqrt{\pi}}{2}$ the $\frac{1}{v}$-part becomes:

$$\langle\sigma\rangle_{1/v} = \sigma_{th}\sqrt{\frac{0.0253}{kT}}, \tag{1.35}$$

with kT in eV and σ_{th} in b. This leads to the useful analytical expression of the MACS [Mac65, Bee92]:

$$\langle\sigma\rangle = \langle\sigma\rangle_{1/v} + \langle\sigma\rangle_{res} = \sigma_{th}\sqrt{\frac{0.0253}{kT}} + \frac{2}{\sqrt{\pi}}\,\frac{1}{(kT)^2}\sum_{res} A_{res}\,E_{res}\,e^{-\frac{E_{res}}{kT}}. \tag{1.36}$$

By deriving this equation to the temperature kT, one can show that a resonance at an energy E_{res} has its maximum contribution to the MACS at $kT = \frac{E_{res}}{2}$. This means that, if the cross section is known up to an energy E_f, MACS values above $\frac{E_f}{2}$ are mainly originating from resonances at energies higher than E_f. Therefore, the calculated MACS values should be regarded as lower limits above $\frac{E_f}{2}$. Once again this shows that the energy range covered by the experiment must be as broad as possible. It must be stressed that, to use this analytical expression, the cross section in the low energy region may not deviate from a $\frac{1}{v}$-shape.

When no experimental data are available, a theoretically calculated cross section is used to determine the MACS values at certain stellar temperatures. Theoretical cross sections are based on statistical Hauser-Feshbach calculations [Hau52, Rau97]. In such an approach, the cross section is averaged over all the resonances. So, to obtain a reliable cross section, a high level density in the compound nucleus is required. As the MACS values are integrations of the cross section over a wide energy range, the structure from the cross section is averaged out and the theoretically determined cross section will give good MACS values in most of the cases. However, for the low mass isotopes studied in this work, the used level densities may be too low for reliable statistical model calculations, making a comparison with the experimentally obtained MACS values difficult.

1.3 Mean lifetime

A last issue of this chapter is the definition of the mean lifetime τ_n of a nucleus against neutron capture. The mean time between subsequent neutron captures is inversely proportional to the neutron density N_n and to the reaction rate. The decay constant λ_n is then, in analogy with radioactive decay, the inverse of the lifetime:

$$\tau_n = \frac{1}{\lambda_n} = \frac{1}{N_n \langle \sigma v \rangle}. \tag{1.37}$$

Chapter 2

Nuclear astrophysics

In the quest for the origin of the elements three main sites for nucleosynthesis are generally assumed:

1. Big Bang nucleosynthesis, responsible for the creation of the light elements H, He and Li;
2. Interstellar nucleosynthesis forming Li, Be and B;
3. Stellar nucleosynthesis forming all the elements from C up to U.

This last point, the nucleosynthesis occuring in stars, will be outlined in the following sections. A discussion of the first two points can be found in [Rol88].

2.1 Stellar nucleosynthesis

2.1.1 Thermonuclear fusion reactions

A protostar is formed at places in the interstellar medium where the density is high enough so that gas clouds, mainly consisting of the ashes of Big Bang H and He, contract under their own gravity. The conversion of gravitational energy into thermal energy leads to a continuous heating of the inner regions. When the temperature in the core is high enough, thermonuclear fusion of hydrogen starts and a new star is born. As these reactions are exothermic, they give off heat. In this way, the fusion reactions provide enough thermal energy to counteract the contraction caused by gravity and establish hydrostatic equilibrium.

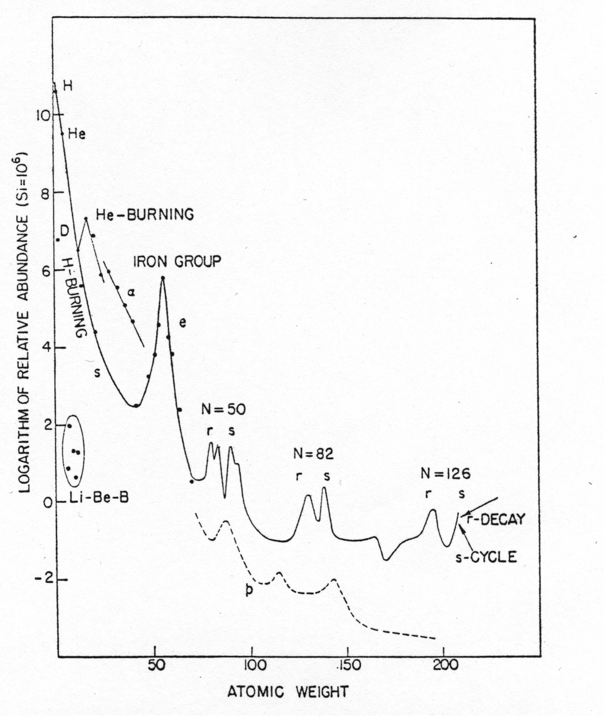

Figure 2.1: Cosmic abundance curve of the elements as a function of the atomic weight [Bur57].

When the hydrogen in the core is exhausted, thermal pressure falls and contraction starts again. This causes a heating of a hydrogen shell around the helium core. The hydrogen burning continues in this shell. As a consequence of the contraction the core temperature rises allowing helium burning to ignite. Carbon and oxygen are now produced and a new equilibrium establishes. Several stages of fuel exhaustion, contraction, rising of the core temperature and fusion reactions of the ashes of previous contractions follow each other, continuously producing heavier nuclei. After every phase, the burning stage migrates to a shell burning around the core. This way of producing elements does not last forever. As the charge of the newly formed nuclei increases, the coulomb barrier gets higher, and higher temperatures are needed to start the next stage of fusion reactions. The effect of rising of the coulomb barrier with mass can be seen in the sharp drop in the elemental abundances from Z = 1 to 40 (figure 2.1). The peak around the iron elements forms an exception because the binding energy per nucleon reaches top values there. For nuclei beyond the iron group, the binding energy per nucleon drops with higher mass. These reactions become endothermic and consequently need energy. In addition, the temperatures needed to overcome the coulomb barrier are so high that photodesintegration impedes the formation of heavier nuclei by charged particle fusion reactions.

2.1.2 Neutron induced reactions

Because neutrons are not hindered by the coulomb barrier, it is generally accepted that neutron induced reactions are responsible for the production of the elements beyond iron. In figure 2.1 the cosmic abundances of the heavy elements are shown. Narrow peaks appear at the mass numbers related to closed neutron shells which is a strong evidence that heavy nuclei are indeed produced by neutron induced reactions. The occurence of broader peaks for nuclei with 4 to 10 atomic weight units below the closed neutron shells, historically led to the definition of two nucleosynthesis scenarios: the s or slow process and the r or rapid process. They appear in different astrophysical environments with completely different neutron fluxes. For both processes the heavier elements are produced by a succession of neutron captures and β-decays on existing seed nuclei. The difference between the s- and r-process is the relative lifetime for neutron capture and β-decay: in the case of the s-process, $\tau_n > \tau_\beta$, while for the r-process $\tau_n << \tau_\beta$.

If an unstable nucleus is encountered in the neutron capture chain during the s-process, β^--decay is much faster than another neutron capture. This ensures that the neutron capture path for the s-process will follow the β-stability line, which is shown in figure 2.2. On the other hand, stable isotopes in the neutron capture chain with small neutron cross sections will build up large abundances and act as bottlenecks in the reaction chain. Isotopes with magic neutron numbers N = 50, 82 and 126, have very small neutron cross sections explaining the sharp s-process peaks in the abundance chart. s-process nucleosynthesis comes to a halt when the heaviest stable nucleus, ^{209}Bi, is formed. Heavier nuclei synthesised in these environments will rapidly decay via α-decay.

The r-process takes place at stellar phases where the neutron density is extremely high, so that $\tau_n << \tau_\beta$. Therefore, neutron capture processes will

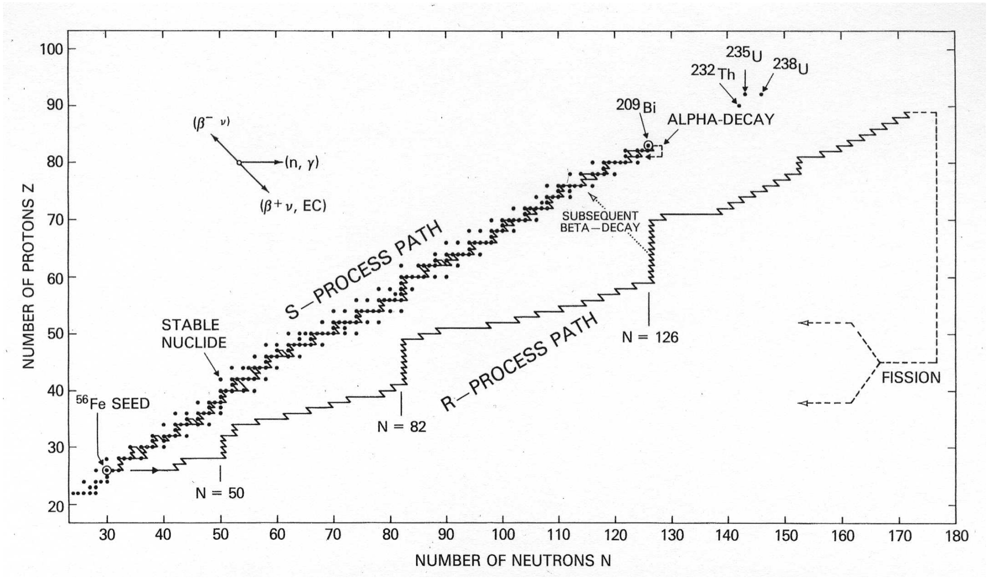

Figure 2.2: Neutron capture chain for the s- and r-process in the (N,Z) plane [Rol88].

succeed each other up to the neutron drip line where the neutron binding energy becomes close to zero. Only then, β-decay can compete with the neutron capture reactions to increase the nuclear charge by one unit. Once the neutron flux ceases, the neutron rich nuclei evolve to the region of stability by several β-decays. During the r-process the closed neutron shells are encountered in the neutron rich region at lower proton numbers. The next neutron capture will provide an isotope with N+1 neutrons, which has a very small neutron binding energy and relatively long half-life. So, nuclei with closed neutron shells are so-called waiting points for the r-process. After neutron capture and β-decay the (Z,N) nucleus is transmuted to (Z+1,N), again a nucleus with the same closed neutron shell. Therefore, several waiting points with the same closed neutron shell but higher Z are encountered. This sequence lasts until the resulting nucleus is sufficiently close to the β-stability line so that the neutron binding energy becomes large enough to break through the magic neutron bottleneck and the normal sequence of neutron capture will resume (see figure 2.2). After β-decay to the stability valley, the abundance peaks of the formed nuclei with closed neutron shells will appear at lower neutron numbers than the s-process peaks, N = 46, 76 and 116. This explains the second broader peak in the abundance chart at lower A number. The r-process will stop after formation of isotopes with mass number $A \cong 270$ through (n,f), spontaneous fission or β-delayed fission and may be held responsible for the formation of neutron rich elements far from the stability line. The existence of uranium and thorium in addition to the double peaks, is one of the major indications for the r-process.

For the sake of completeness one has to mention that there is need for a third nucleosynthesis process: the p-process, responsible for the formation of the, much less abundant, proton rich elements. The s- as well as the r-process bypass these proton rich nuclei along the valley of stability. The p-process involves positron production and capture, proton capture and (γ,n) or (p,n) reactions starting from s- and r-isotopes as seed nuclei.

One concludes that the elements beyond iron are produced in three essentially different processes. The slow process is assumed to occur mainly inside stars during the hydrostatic stage of their life while the rapid process must take place in an explosive environment like a supernova explosion. Finally, the proton rich elements, which are bypassed by the previous processes, are produced during the p-process.

2.1.3 The Hertzsprung-Russell diagram

Data of thousands of stars are available. In a Hertzsprung-Russell (HR) diagram, stars are represented as a function of their luminosity and their temperature. An example of such a HR-diagram is depicted in figure 2.3. Immediately it is noticed that there is order: stars are not arbitrary scattered over the diagram, but appear in groups. Each group has its own name and properties:

- *main sequence*: the bulk of the stars are lying on the main sequence. Burning hydrogen in their cores, stars on the main sequence spend their infancy and adulthood there;

- *white dwarfs*: they are located in the left down corner of the diagram. These stars are small, hot, their luminosity is low and they have a high density. The matter of a white dwarf is degenerated;

- *giants*: these are bright, cool stars, located at the upper right of the HR-diagram and burn elements heavier than hydrogen in their core.

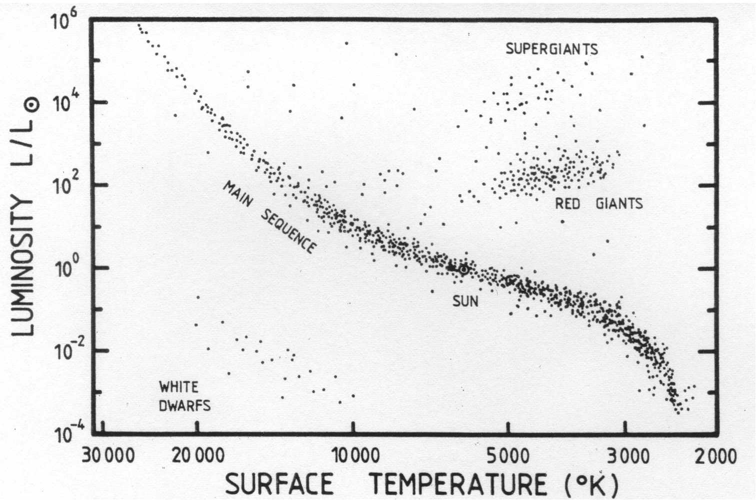

Figure 2.3: A Hertzsprung-Russell diagram [Rol88]. Note that the temperature scale is going from right to left.

2.1.4 Stars die as well

Depending on the initial mass of the star and thus its available gravitational energy, none, some or all the different burning stages will follow each other defining the end of the life of a star. The different possibilities, depending on the initial mass of the star, are listed in the following classification and are taken from [Kau99].

- Protostars with a mass lower than 0.08 $M_\odot$, where $\odot$ refers to the Sun, are not able to ignite hydrogen burning. They will evolve to brown dwarfs.
- Stars with a mass lower than 4 $M_\odot$ will not produce enough pressure or temperature to ignite carbon or oxygen. On the contrary, the star ejects its outer layers and a carbon-oxygen core surrounded by gas shells is left, forming a planetary nebula. The core starts to cool and forms a white dwarf.
- In stars with initial mass between 4 $M_\odot < M < 8\ M_\odot$ carbon burning may occur but will be the last burning stage. This leads again to a

planetary nebula and the core will become a white dwarf. However, it is possible that stars with initial mass between 5 $M_\odot < M < 8 M_\odot$ end their life with a supernova explosion instead of forming a planetary nebula [Zei88].

- The biggest stars with mass higher than 8 $M_\odot$ will die inconceivably violent in a supernova explosion. As mentioned before, several stages of contraction, rising of the core temperature and fusion reactions of the ashes follow each other until the iron elements are formed. Then, the thermonuclear fuel is exhausted in the center of the star. With no elements left to burn to maintain hydrostatic equilibrium, the star can not prevent the implosion of its own core. The contraction holds on until nuclear densities are reached in the center of the imploding star. The matter in the core can not be compressed more and the core will bounce. A shock wave starts to move outward, compressing the matter on its path and causing new nuclear reactions which form elements heavier than iron. Finally, the shock wave will throw off the envelope of the star leaving behind a neutron star or black hole.

So, there is a cycling process in which matter is transferred back and forth between stars and the interstellar medium. Each cycle enriches the interstellar medium with the produced elements. This leads to the abundance distribution observed nowadays.

Stars are thus the cooking pots of the elements. Although nucleosynthesis theory is quite well understood, questions about how and where some of the elements are generated still remain. The origin of ^{36}S and ^{26}Al are two of the remaining problems relevant for the reactions investigated in this work. For the first one it is necessary to explain the s-process in more detail in section 2.2. For the origin and subsequent destruction of ^{26}Al, an explanation of Asymptotic Giant Branch or AGB stars is required, which is given in section 2.4.

2.2 The s-process

2.2.1 Mechanism

As stated above, the s-process track traverses the chart of isotopes along the β-stability valley from ^{56}Fe as seed nucleus up to ^{209}Bi, the last stable nucleus. For a real understanding of the ongoing processes it is necessary to calculate the s-process nucleosynthesis quantitatively, which means solving a set of differential equations with an abundance pattern as outcome. A first attempt to do this led to the formulation of the classical s-process in the paper of Burbidge *et al.* [Bur57]. More information on the s-process can be found in [Rol88, Käp89, Cla68].

For the classical s-process one has to assume that there exists a steady neutron flux, low enough so that β-decay is faster than neutron capture. Now, a pre-existing seed distribution has to be exposed to this neutron irradiation. The change in time of the abundance N_A of an element with atomic mass A and charge number Z can be written as:

$$\begin{aligned} \frac{dN_{A,Z}}{dt}(t) &= \sum \textit{creation terms} - \sum \textit{destruction terms} \\ &= \lambda^n_{A-1,Z}(t)\,N_{A-1,Z}(t) + \lambda^\beta_{A,Z-1}(t)\,N_{A,Z-1}(t) \\ &\quad - \lambda^n_{A,Z}(t)\,N_{A,Z}(t) - \lambda^\beta_{A,Z}(t)\,N_{A,Z}(t), \end{aligned} \tag{2.1}$$

with λ^n and λ^β the neutron capture and β-decay rate, respectively. λ^n is defined in section 1.3 as:

$$\lambda^n_A(t) = \frac{1}{\tau_n(t)} = n_n(t)\,\langle\sigma v\rangle_A, \tag{2.2}$$

where $n_n(t)$ denotes the neutron density. The β-decay rate $\lambda^\beta(t) = \frac{1}{\tau_\beta(t)}$ must be considered only if the isotope is unstable. Under stellar conditions, the β-decay lifetime is time dependent via its dependence on the temperature.

When an unstable isotope ${}^{A}_{N}\mathrm{X}_Z$ is formed by neutron capture of the previous formed stable isotope ${}^{A-1}_{N-1}\mathrm{W}_Z$, all the formed X will decay to the next isotope in the s-process path ${}^{A}_{N-1}\mathrm{Y}_{Z+1}$. Thus, the abundance of ${}^{A}\mathrm{Y}$ is completely determined by the neutron capture rate of ${}^{A-1}\mathrm{W}$. Therefore, equation 2.1 can be rewritten as:

$$\begin{aligned} \frac{dN_A}{dt}(t) &= \lambda^n_{A-1}(t)\,N_{A-1}(t) - \lambda^n_A(t)\,N_A(t) - \lambda^\beta_A(t)\,N_A(t) \\ &= \lambda^n_{A-1}(t)\,N_{A-1}(t) - N_A(t)\left(\lambda^n_A(t) + \lambda^\beta_A(t)\right). \end{aligned} \tag{2.3}$$

Equation 2.3 leads to a set of coupled differential equations, which unfortunately can not be solved for the most general cases. Therefore, some simplifications are generally adopted:

1. *The stellar temperature is constant during the s-process.*
   Then the capture cross section is well defined:

   $$\langle \sigma v \rangle_A = \sigma_A \, v_T, \tag{2.4}$$

   with σ_A the MACS for an isotope with atomic mass A and v_T the mean thermal neutron velocity. This does not mean that the s-process can only occur at one particular temperature, it can take place at another astrophysical site with a different temperature. But at a specific site, the temperature changes very little, because the stellar region where it takes place burns with nearly constant temperature until the neutron producing fuel is exhausted.

2. *Either $\lambda^\beta >> \lambda^n$ or $\lambda^n >> \lambda^\beta$.*
   In the first case the formed radioactive nucleus decays rapidly and its abundance can be neglected, while in the latter case, the formed nucleus can be treated as stable and λ^β can be neglected. Only at branching points, where $\lambda^\beta \cong \lambda^n$, a seperate approach is needed.

With these two assumptions equation 2.3 can be reduced for a stable nucleus to:

$$\frac{dN_A}{dt}(t) = v_T \, n_n(t) \left(\sigma_{A-1} \, N_{A-1} - \sigma_A \, N_A \right). \tag{2.5}$$

By defining a new quantity, the neutron exposure τ, which represents the time integrated neutron flux:

$$\tau = \int\limits_0^t \phi(t) \, dt = v_T \int\limits_0^t n_n(t) \, dt, \tag{2.6}$$

where $\phi(t)$ is the neutron flux, defined as:

$$\phi(t) = v_T \, n_n(t), \tag{2.7}$$

the differential equation can eventually be rewritten:

$$\frac{dN_A}{d\tau}(t) = \sigma_{A-1} \, N_{A-1} - \sigma_A \, N_A. \tag{2.8}$$

The processes described by this set of coupled differential equations have the tendency to be self-regulating. This means that they try to minimize the difference between $\sigma_{A-1}N_{A-1}$ and $\sigma_A N_A$, or that after sufficiently long irradiations an equilibrium between the destructing and formation terms establishes, leading to $\frac{dN_A}{d\tau}(t) = 0$ or:

$$\sigma_A\, N_A = \sigma_{A-1}\, N_{A-1} = constant. \tag{2.9}$$

The plateaus in figure 2.4 show that this relation is valid in the mass region between closed neutron shells (A =90 - 140 and A = 140 - 206) where a local equilibrium is established. This implies that a nucleus with a small neutron capture cross section must have a large abundance to maintain continuity in the s-process path. Nuclear shell structure introduces the steps at A = 84, 138 and 208, which correspond to magic neutron numbers and which lead to the s-process abundance peaks observed in figure 2.1. For these nuclei, the neutron capture cross section is very small. With a finite amount of neutrons available, σN must drop to a new plateau. However, the presence of these steps and the behaviour at A $<$ 80 clearly indicate that equilibrium is not reached over the whole s-process path from ^{56}Fe to ^{209}Bi. Searching for an explanation, Clayton *et al.* [Cla61] concluded that the observed abundances of the isotopes which are exclusively produced during the s-process (s-only) cannot be reproduced by a single irradiation of the iron seed nuclei. The abundance curve is therefore a superposition of different neutron fluxes exposed to a different amount of iron seed nuclei, assuming that the total abundance of an isotope is not influenced by interruption in time or difference in location of the exposures.

2.2.2 Neutron sources and s-process sites

It turned out that three different neutron exposure distributions are required for a complete description of the observed s-process abundances [Cla67, Cla74, Bee85, Käp82]. The main component, which is responsible for the synthesis of the isotopes with atomic mass A $>$ 90, the weak component, which accounts for the isotopes below A $\sim$ 90 and finally a strong component explaining the lead-bismuth abundance peak. Each component takes place in different stages during the life of a star and different reactions produce the neutrons needed.

- *The main component*: It is responsible for the production of the isotopes with A $>$ 90 and is assumed to take place in the convective He-burning shell of low mass stars during the Asymptotic Giant Branch (AGB) phase of their life. The AGB phase will be highlighted in section 2.4.

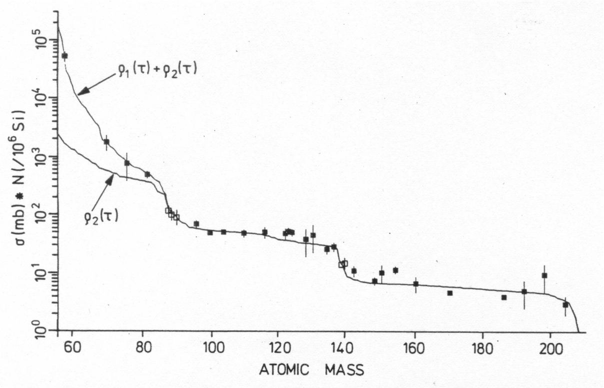

Figure 2.4: The product of the MACS at 30 keV times the solar system abundance as a function of atomic mass for s-only isotopes [Rol88].

The convective He-shell (rich in carbon) mixes with the hydrogen rich envelope and neutrons may be produced by this reaction sequence:

$$^{12}C(p,\gamma)^{13}N(e^{+},\nu)^{13}C(\alpha,n)^{16}O. \tag{2.10}$$

The ^{13}C(α,n)^{16}O reaction is already ignited at kT = 8 keV.

- *The weak component*: It has been ascribed to the core He-burning in massive stars at a temperature of 25 - 30 keV and is needed to explain the abundance of the isotopes below A $\sim$ 90. The neutrons come from the ^{22}Ne(α,n)^{25}Mg reaction which is ignited at the end of the He-core burning phase. The ^{22}Ne necessary for the neutron production is produced by the following reaction chain:

$$^{14}N(\alpha,\gamma)^{18}F(e^{+},\nu)^{18}O(\alpha,\gamma)^{22}Ne. \tag{2.11}$$

When the ^{22}Ne supply is not completely exhausted, subsequent C-shell burning at 86 keV may also be considered as s-process site for the weak component [Rai93]. C-core burning and all the following core burnings can be excluded as production sites because the region where these processes take place will remain as stellar remnant or neutron star after the supernova explosion. All elements in the neutron star are trapped and are not released in the interstellar medium. Therefore, they do not participate in the galactic chemical enrichment. Taking into account some seed nuclei below ^{56}Fe, the weak component may be responsible for the production of some light neutron rich isotopes like ^{36}S (see section 2.3).

- *The strong component*: This component is necessary to explain the abundances of the lead and bismuth isotopes at the end of the s-process path. He-core flashes in low mass stars seem to be the place where the strong component is active. The ^{13}C(α,n)^{16}O reaction should be responsible for the neutron delivery.

  Another suggestion for the missing abundance of the lead and bismuth isotopes during the main component has been proposed by Gallino ([Gal90, Rat04] and references therein). It should take place in low metallicity (= all elements apart from H and He) AGB stars during the thermal instabilities. More details about the AGB phase can be found in section 2.4. Again the ^{13}C(α,n)^{16}O reaction produces the neutrons. However, ^{13}C is synthesized from H and He and therefore metal independent. This means that when the metallicity is decreased, the same amount of ^{13}C and thus the same amount of neutrons will be produced, yet they will irratiate less seed nuclei. The result seems to be that with decreasing metal content, the lead and bismuth isotopes will be increased dramatically. On the other hand, this decrease has no effect on the s-only isotopes produced during the main component.

2.3 The origin of ^{36}S

In section 2.1 it is shown that the elements up to iron are generated during the hydrostatic and explosive burning stages of a star via charged particle reactions. However, there are a few rare neutron rich isotopes which are not efficiently produced in these scenarios. One of these rare isotopes is ^{36}S. An alternative mechanism for the production of part of the ^{36}S is the weak component of the s-process in massive stars [Bee87]. An additional, but smaller contribution may come from He-shell burning in low mass AGB stars during the main s-process [Str95, Gal98]. The suggestion of a s-process origin for ^{36}S is supported by the detection of ^{36}S bearing molecules in the interstellar medium where the ^{34}S/^{36}S ratio of 115 ± 17 [Mau96] was far below the solar ratio of 288 [Din01]. This difference indicates that ^{36}S must be produced in a process different from that of the other sulphur isotopes.

To verify the s-process hypothesis, nucleosynthesis network calculations are

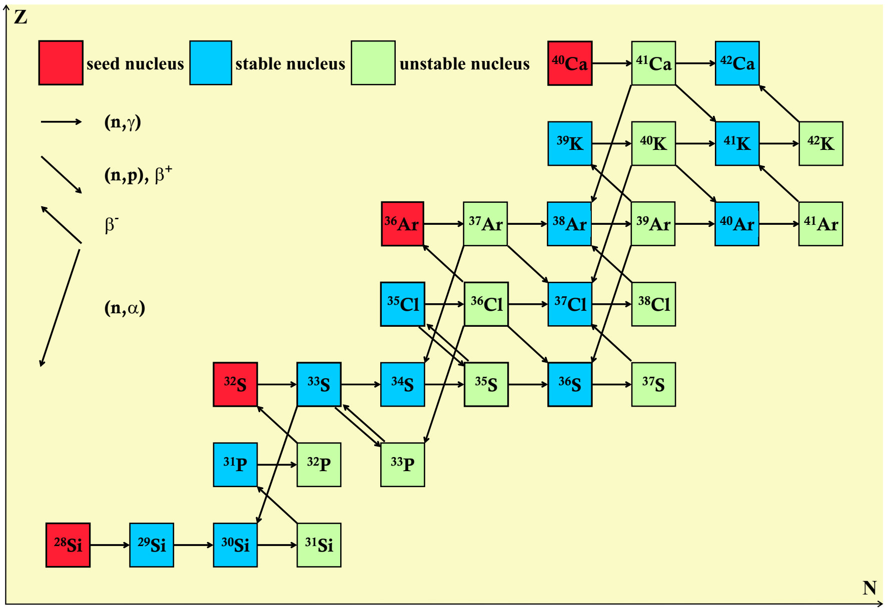

Figure 2.5: s-process synthesis path in the mass region $28 \leq A \leq 42$.

necessary. For the ^{36}S production, a s-process network with masses between $28 \leq A \leq 42$ is sufficient. An example of such a s-process network is depicted in figure 2.5. It shows that there are three reactions leading directly to ^{36}S and therefore influencing its abundance in a direct way:

1. ^{35}S(n,γ)^{36}S;
2. ^{36}Cl(n,p)^{36}S;
3. ^{39}Ar(n,α)^{36}S.

All three isotopes are unstable, but because ^{36}Cl is long-living the neutron induced reactions will be active during He-core as well as during C-shell burning. The other two reactions on the contrary will only be ignited during C-shell burning when the neutron density is high enough. From figure 2.5 it is clear that there are important branchings in the reaction chain at ^{33}S, ^{35}S and ^{36}Cl influencing the ^{36}S production. The ^{33}S(n,α)^{30}Si reaction is hampering the ^{36}S production because most of the reaction flow from the ^{32}S seed nucleus is recycled to the lighter element ^{30}Si. The ^{35}S branching to ^{35}Cl is not so important, because the subsequent ^{36}Cl(n,p)^{36}S reaction is the dominant channel at the ^{36}Cl branching. Anyway, the ^{34}S(n,γ) reaction turns out to be the most important reaction towards ^{36}S [Sch95, How72]. The experimentally determined ^{34}S(n,γ) cross section is very low [Rei00], causing a bottleneck effect for the reaction flow from ^{34}S to ^{36}S. So, the main effect of the small ^{34}S cross section is a significant suppression of the mass flow from the abundant seed nuclei ^{28}Si and ^{32}S. Consequently, the rarer isotope ^{35}Cl is replacing ^{34}S as important seed for the ^{36}S production. Figure 2.5 shows the (n,α) branching at ^{41}Ca towards ^{38}Ar. This recycling influences the ^{36}S production through the ^{39}Ar(n,α)^{36}S branching.

With the experimental data at their disposal in 2000, Schatz *et al.* [Sch95] concluded that the s-process cannot be responsible for the complete ^{36}S production and only part of its abundance can be accounted for by the s-process. However, other proposed sites such as supernova explosions do not appear to be very promising at the moment. A consequence of this conclusion together with the ^{34}S bottleneck cancels the probability for ^{36}S as being a neutron flux monitor for He and C-burning in massive stars.

The influence of the updated ^{36}Cl(n,p), ^{36}Cl(n,α) and ^{41}Ca(n,α) reaction cross sections on the ^{36}S production will be discussed in section 6.5.2.

2.4 AGB stars and nucleosynthesis

In this section the stellar evolution of low and intermediate mass stars, $M \leq 8\ M_{\odot}$, will be discussed. In particular the period near the death of the star: the Asymptotic Giant Branch or AGB phase of its life. In the last decades, a lot of research has been dedicated to the understanding of AGB stars. A brief summary of its characteristics and rich nucleosynthesis is given in this section, without pretending to be complete. An in depth discussion can be found in the work of Mowlavi [Mow98], Lattanzio [Lat, Lat02], Straniero [Str05], Wasserburg [Was05] and references in these articles.

As mentioned in section 2.1 a main sequence star uses all the hydrogen in its core. The aged star then leaves the main sequence. Once core hydrogen burning ceases, the core shrinks, heating the surrounding hydrogen and triggering hydrogen burning. This energy release causes the outer layers of the star to expand, causing a decrease in surface temperature: the star becomes a red giant. During this stage, the convective envelope penetrates in the region

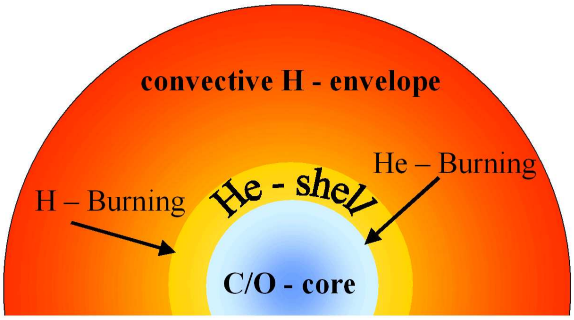

Figure 2.6: Schematic view of the structure of a star at the beginning of the AGB stage [Hei03].

above the H-shell, enriching the surface composition with the ashes of proton captures from the main sequence; this is a first dredge up of synthesized elements to the surface of the star. Next, the helium rich core shrinks and heats until eventually core helium burning begins through the triple α-process. When all the helium in the core has been converted into carbon and oxygen, core helium burning ceases. Without thermonuclear reactions to maintain the core's internal pressure, the core again contracts until it is stopped by degenerate electron pressure. Any further compression would violate the Pauli exclusion principle. Because the electrons can not come closer together, they produce a powerfull pressure that resists further core contraction. This degenerate pressure, unlike the pressure of an ideal gas, does not depend on temperature. The contraction releases heat into the surrounding helium rich gases and a new stage of helium burning begins in a thin shell around the core. Because the helium core burning stops, the outer layers expand again and the star ascends for a second time into the red giant region of the HR-diagram, this time with a greater luminosity than during its first red giant phase. The star is now at the beginning of the AGB stage of its life. A schematic view of its structure is given in figure 2.6. The envelope penetrates in the deep layers and in stars more massive than about 4 $M_\odot$, the products of H-burning are transported for the second time to the surface: second dredge up.

One of the characteristics of the AGB phase is the thermally unstable He-burning shell, resulting in periodic thermal pulses or shell flashes. Shell flashes are divided into four phases; a schematic picture of an AGB star during this

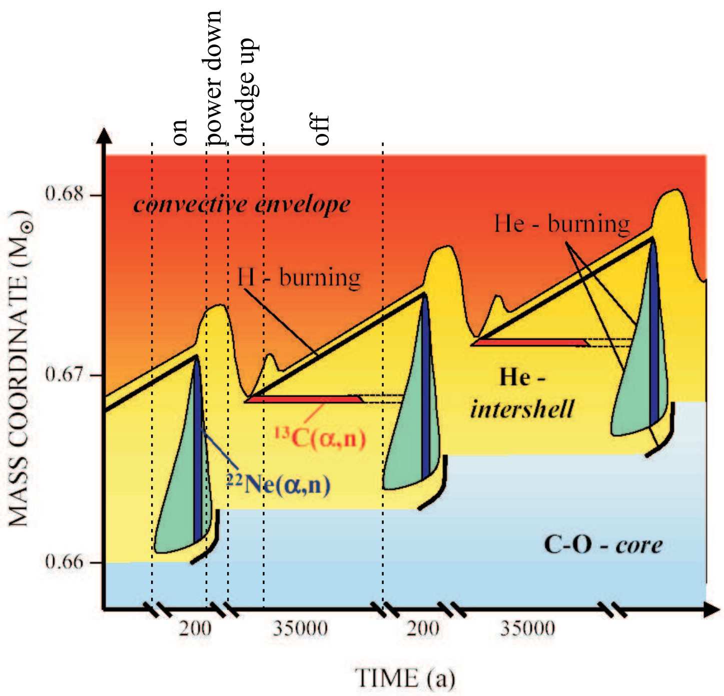

Figure 2.7: Schematic view of the evolution of the positions of the inner border of the convective envelope, the H-burning shell and the He-burning shell during the thermally pulsing AGB phase [Hei03].

phase is shown in figure 2.7.

1. During the *on* phase, the He-shell burns very strongly and drives a convective zone from the He-shell almost to the H-shell.

2. When the He-burning shell extinguishes, the *power down* phase starts, causing the convection to shut-off. As a response to the energy input from the He-shell burning, the star expands. This causes the outer regions to cool and the H-shell burning is extinguished.

3. The convective envelope, in response to the cooling of the outer layers, extends inward during the *dredge up* phase and can penetrate the region which was previously part of the intershell convective zone. This brings

^{12}C, produced by the He-shell burning and brought outward by the flash-driven convection, to the surface of the star by the envelope convection.

4. Finally, the dredge up stops and the star contracts again, leading to the re-ignition of the H-shell burning. The structure of the star resembles the early AGB phase. The star stays for a long period in this *off* or *interpulse* phase.

This is called the third dredge up. Since the thermal pulses are repeated periodically, the third dredge up can happen many times while the star ascends the AGB. Eventually, enough carbon can be transposed to the surface of the star so that a carbon star is formed. The AGB evolution is stopped by mass loss. How exactly the star loses its envelope is one of the major uncertainties in the stellar models. After the ejection of the envelope, the degenerated carbon-oxygen-core is left over and becomes a white dwarf.

The importance of AGB stars lies in its very rich nucleosynthesis, demonstrated by astronomical observations showing enriched s-process elements in AGB stars. The most obvious nucleosynthesis site is the H-burning shell. During the interpulse phase it synthesizes helium and heavier elements through the p-p chain and the CNO-cycle. Both processes convert four H-atoms into one He-atom. An in depth discussion of both cycles can be found in [Rol88]. The synthesized particles are continuously brought to the stellar surface by the convective envelope.

The H-burning shell may leave some ^{13}C from the CNO-cycle in the upper region of the He-rich intershell. This ^{13}C can capture a α-particle and release a neutron: ^{13}C(α,n)^{16}O. These neutrons may be captured by Fe starting the s-process. However, this releases not enough neutrons to produce the observed s-process enhancements. A possible solution is partial mixing at the bottom of the H-envelope during the dredge up phase. Then some protons are deposited in the intershell region. During the subsequent contraction ^{12}C captures a proton and forms ^{13}C. But, not too many protons may be mixed in the intershell otherwise ^{13}C will capture a proton instead of a α-particle and form ^{14}N simply proceeding through the CNO-cycle. If this requirement is fulfilled, there will be a ^{13}C-pocket in which neutrons are produced, which can be captured by Fe and the s-process will occur. During the next pulse this zone with the synthesized s-elements is mixed into the convective intershell. Also the higher temperatures at the bottom of the intershell will ignite the ^{22}Ne(α,n)^{25}Mg reaction giving rise to a second neutron burst with a small exposure, but with a high peak neutron density. This modifies the final s-process composition at branchings along the s-process path, depending on the neutron density or temperature. The dredge up phase then brings the formed s-elements to the surface of the star where they are observed by spectroscopists. Due to the lack of a reliable description of the physical phenomena that govern the diffusion of protons into the He-intershell, the amount of ^{13}C in the AGB stellar models has to be taken as a free parameter.

If the stellar mass is sufficiently high, $M \geq 4\ M_{\odot}$, the bottom of the convective envelope extends into the top of the H-burning shell and some nuclear processes are active within the most internal layers of the convective envelope; this is called *hot bottom burning* or HBB. Note that this can stop a star from becoming a carbon star, as the ^{12}C brought to the surface during the dredge up will be converted into ^{14}N through the CNO-cycle at the bottom of the envelope.

Despite the difficulties encountered in AGB stellar models, it is clear that during the AGB phase, the star undergoes a very rich nucleosynthesis. AGB stars are very important for the chemical evolution in our Galaxy as after the dredge ups the synthesized elements are ejected in the interstellar medium through stellar winds.

2.5 ^{26}Al in our Galaxy

As mentioned in section 2.1, nowadays the origin and destruction of radioactive ^{26}Al in our Galaxy is an interesting astrophysical topic. It may give information on galactic evolution, on the birth of the solar system and on stellar nucleosynthesis.

^{26}Al decays to the first excited state of ^{26}Mg, which deexcites almost immediately to the ground state by emitting a 1.809 MeV γ-ray. This is illustrated in the decay scheme of figure 2.8. These γ-rays were detected for the first time by the HEAO-3 satelite [Mah84] and confirmed by many subsequent observations. The COMPTEL imaging telescope aboard the Compton γ-ray Observatory of the NASA provided the first-ever image of the sky in emission from radioactive ^{26}Al [Obe97] which is shown in figure 2.9. It illustrates that the 1.8 MeV emission is mainly concentrated towards the galactic plane, which demonstrates that the bulk of ^{26}Al is of galactic rather than local origin. How-

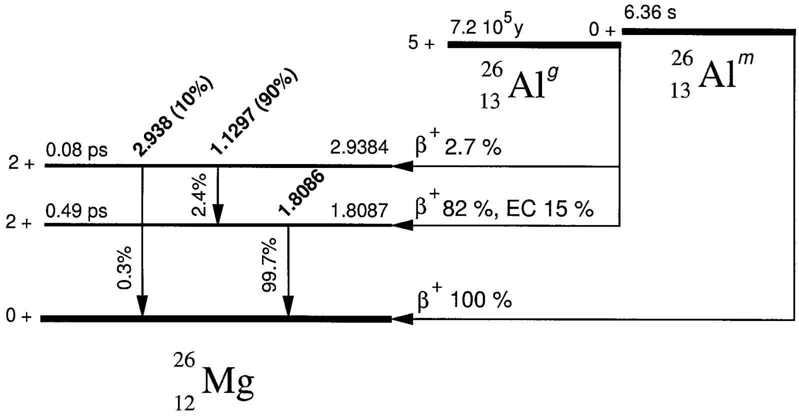

Figure 2.8: Decay scheme of ^{26}Al [Led78].

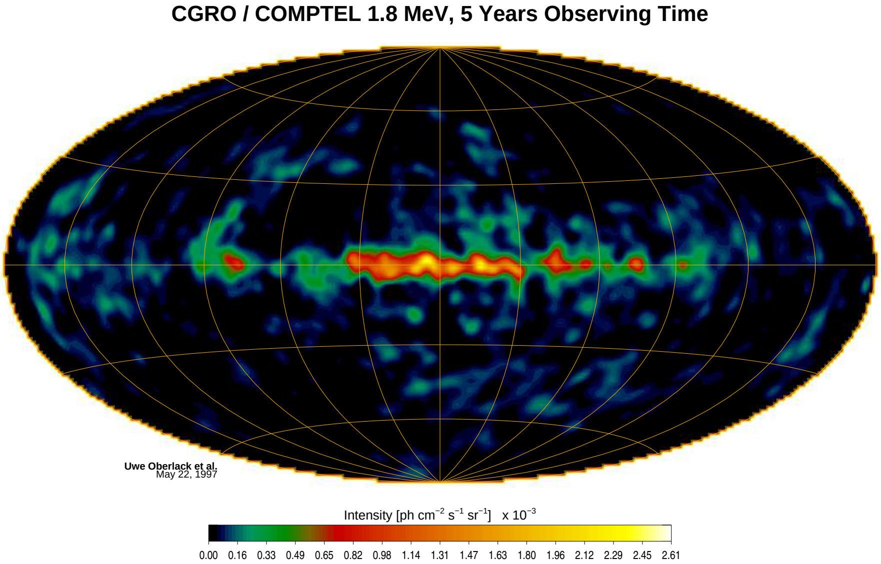

Figure 2.9: Image of the sky from the 1.8 MeV γ-rays from radioactive ^{26}Al; image taken from [Obe97].

ever, some distinct emission features are present, which is inconsistent with a smooth galactic emission profile. Since the half-life of ^{26}Al, $T_{\frac{1}{2}} = 7.17 \times 10^5$ y, is much shorter than the time scale for galactic evolution - the age of our Galaxy is of the order of 10^{10} years - this map reveals information on recent and ongoing nucleosynthesis in large and extended parts of our Galaxy.

^{26}Al is also held responsible for the ^{26}Mg over-abundances found in meteoritic material. Meteoroids[1] were formed when the solar system formed some 4.6×10^9 years ago and may be composed of grains of stardust. Each grain has condensed in the outflow from a single star, so it contains information on the composition of that star. By the time the solar system condensed, the material present in the solar nebula was thoroughly blended. In this way the solar isotopic composition is homogeneous, reflecting the average isotopic content of all the stellar debris and the primordial gases hydrogen and helium. However, the grains of stardust survived the formation of the solar system and thus preserve the elemental and isotopic composition of their stellar sources. When such a meteoroid falls on Earth its composition can be studied in a laboratory, which provides important information about stellar nucleosynthesis and physical and chemical conditions during the grain formation. When the isotopic composition of one or more elements in the grain differs a lot from the solar isotopic composition, such a grain can be considered as ancient stardust. However, it is impossible to know which grain originated in which kind of star.

In some meteorites abnormally high values of ^{26}Mg/^{24}Mg have been found, whereas ^{25}Mg/^{24}Mg was essentially solar. This indicates that ^{26}Al was present at the formation of the meteoroid, before the formation of the solar system. Its decay produced the ^{26}Mg excess. This and other isotopic anomalies in meteorites can provide information on stellar nucleosynthesis and on the birth of the solar system. For example it can indicate whether the formation of the solar system was aided by the explosion of a nearby supernova or by mass ejection from a nearby red giant star.

Now, the remaining question is where the ^{26}Al originated. To be observable in γ-ray spectra and to be present in meteorites in the form of ^{26}Mg excess, ^{26}Al has to be ejected in the interstellar medium before destruction. This can

---

[1] The difference between a meteoroid and a meteorite is the following: a meteoroid is a small rock or metallic object in orbit around the Sun or another star; when a meteoroid strikes the Earth or another large object, it is called a meteorite.

easily be achieved in explosive sites such as supernovae. On the other hand, stars suffering extensive mass loss through stellar winds such as AGB stars or Wolf-Rayet stars could also be possible candidates.

Wasserburg *et al.* [Was05] recently concluded that supernova explosions are no acceptable scenarios for providing the 'observed' ^{26}Al, while it could be produced in AGB stars. The production of ^{26}Al in Wolf-Rayet stars has not been examined in this work, more information can be found in the work of Meynet and Arnould [Mey93].

The aluminium isotopes are produced in three sites in AGB stars [Kar03]: in the H-burning shell, in the He-burning shell and at the bottom of the convective envelope through hot bottom burning. The first and the latter one produce ^{26}Al through the Mg-Al chain; more details about this chain can be found in [Rol88]. During He-shell burning, the temperature is higher and ^{26}Al is produced through α-capture on ^{22}Ne, which is apart from ^{12}C a He-burning product. In section 2.4 it is shown that during the interpulse phase of the third dredge up a rich nucleosynthesis occurs through the release of neutrons via the ^{13}C(α,n)^{16}O reaction. When the temperature is right, the ^{26}Al(n,α) or ^{26}Al(n,p) chains may open and destroy the formed ^{26}Al. In this way, ^{26}Al acts as a neutron poison for the synthesis of s-process elements. On the other hand, the ^{26}Al(n,p) reaction, which is expected to have a higher cross section than that of ^{26}Al(n,α), releases protons for the formation of the light elements. This makes clear that hot bottom burning, which occurs only in massive stars, is the most effective site in AGB stars for the production of ^{26}Al.

Obviously, a lot of work remains to be done before one can make any final conclusion about whether ^{26}Al is produced or not in AGB stars. For the moment a new ESA satelite INTEGRAL has been put into orbit round the Earth. It will provide clearer and more detailed maps of the γ-emission from ^{26}Al in the Galaxy. In this way one hopes to find the stellar source(s) responsible for the ^{26}Al production. Probably this will also help to improve stellar models.

Part II

Experiment

Chapter 3

Experimental setup

To perform neutron induced reactions a neutron source must be available. Three primary neutron sources exist: radioisotopes, nuclear reactors and accelerator-based neutron sources. Typical isotopic sources are ^{252}Cf, which decays via spontaneous fission and produces neutrons in this way, and AmBe, which produces neutrons via the α-decay of Am and subsequent ^{9}Be(α,n)^{12}C reaction. In the case of research reactors, the neutrons are usually in the thermal and epithermal energy region, depending on the temperature of the moderator. The beam can be pulsed by using a chopper. Finally, neutron sources based on accelerators may be generated in a variety of ways. Because neutrons have no charge, they cannot be accelerated. They must be produced as secondary particles in charged particle or gamma induced reactions. The most common accelerator based neutron source uses the t(d,n)^{4}He reaction. This reaction produces mono-energetic neutrons of 14 MeV, which may be slowed down by collisions in a moderator. In cyclotrons and synchrotrons neutrons are produced by (p,n) reactions. Proton accelerators use spallation sources to produce the neutron beam. As last example in the list of accelerator-based neutron sources, the electron accelerator is mentioned. The neutrons are produced via Bremsstrahlung in a heavy nucleus through (γ,n) reactions. If the target is even fissionable, also (γ,f) reactions will take place.

From the possible neutron sources listed above, neutron beams can be devided into two types: monochromatic beams where the neutrons have a fixed energy and polychromatic beams, where the neutrons have different energies. In analogy with optics, the latter one is known as a white neutron spectrum. In this case the energy of the neutron which causes the reaction has to be determined. This is achieved by pulsing the neutron beam and measuring the time a neutron needs to travel a known distance from its production site to the experimental setup. As the neutron itself cannot be detected because it caused the reaction, the reaction product is detected and serves as stop signal. This method is called the time-of-flight (TOF) technique.

The experiments described in this work are carried out at the GEel LINear Accelerator or GELINA, located in Geel, Belgium. It produces pulsed electron beams and uses an uranium target for the neutron production.

3.1 The GELINA neutron TOF-facility

The GELINA neutron TOF-facility was built in 1965 and subsequently upgraded in 1976, 1984, 1994 and 2004. It consists of four main parts: a linear electron accelerator, a compression system, a neutron production target with moderator and finally a TOF-facility [Sal86, Böc90].

Electrons with an energy of 100 keV are injected by a triode gun that produces bursts with a pulse length of about 10 ns. These electrons are accelerated in three sections: a 2 m standing wave accelerator section and two 6 m travelling wave sections. In the first section the electrons reach a velocity close to the speed of light and in the following 2 sections they mainly gain energy in the form of mass. This results in a maximum energy of 140 MeV.

The 10 ns time spread of the relativistic electrons leaving the accelerator sections is reduced using a unique post-acceleration compression magnet. The pulse width of the electrons is reduced to less than 1 ns (FWHM) with an associated peak intensity of about 100 A [Tro85].

These high energy electrons hit a mercury cooled rotating uranium target, in which they are slowed down and generate Bremsstrahlung. The neutrons are mainly produced via photonuclear reactions (γ,n) and (γ,2n) and via photofission reactions (γ,f) [Sal81]. To increase the number of slow neutrons, two water-filled beryllium moderators are placed above and below the uranium target. A picture of the uranium target with one moderator is shown in figure 3.1. Water and beryllium are good neutron moderators because neutrons are slowed down efficiently by collisions with low mass nuclei; moreover hydrogen has a very large neutron scattering cross section. The resulting neutron energy distribution is characterised by a Maxwellian distribution at thermal energy and a high energy tail with approximately a 1/E-shape.

These moderated neutrons are emitted in all directions and enter the 12

Figure 3.1: Picture of the target hall at the IRMM. The uranium target with the moderater above can be seen in the middle; the electrons are coming from the left. The orange tubes are beamstops in front of the flight paths, one beamstop is open.

different flight paths which lead to the measurement stations. The flight paths have lengths ranging from 8 m to 400 m. Depending on the repetition frequency of the linac (1 Hz to 800 Hz) and the flight path length, the experimentally usable neutrons have an energy range from a few meV up to some MeV. Since the moderated neutrons are emitted isotropically, the neutron flux at a certain distance L from the neutron target is proportional to $1/\mathrm{L}^2$.

The total neutron output is continuously monitored by several BF_3 proportional counters placed at different positions around the target hall. These monitors measure the energy-integrated neutron flux. Their output is used to monitor the stability of the accelerator and to normalize spectra to the same total neutron flux. These monitors are referred to further in the text as CM (Central Monitor).

3.2 Detection system

After travelling through the flight path, the neutrons which arrive at the sample can interact with the sample nuclei. As mentioned in the previous section, the reaction products, α-particles and protons in this work, have to be detected to calculate the TOF of the interacting neutrons. A variety of detectors is available for the detection of charged particles.

Ionization chambers are the oldest and easiest gas-filled radiation detectors. These detectors are based on sensing the direct ionization created by the passage of radiation. They were used for the discovery of cosmic rays in 1911 and to demonstrate the existence of the neutron in 1932. During the following decades the interest in ionization chambers decreased and more attention was given to solid state detectors, most commonly silicon and germanium semiconductors. One immediate advantage of these detectors is their dimension. Because the density of a solid is much higher than that of a gas, a solid state detector can be much smaller. Another advantage of solid state detectors is their better energy resolution. However, they are very sensitive to radiation, particularly to neutron radiation. Furthermore, it is very difficult to make a big solid state detector in order to detect charged particles over large solid angles. These disadvantages together with the versatility of ionization chambers led to a revival of these chambers during the last few years.

For the detection of the α-particles and protons in this work, a Frisch gridded ionization chamber is used. The function of the Frisch grid will be explained in the next subsection. The advantages of using an ionization chamber in this work are its 2π detection geometry, its high detection efficiency and its negligible sensitivity to neutron radiation.

3.2.1 The ionization chamber

In principle an ionization chamber is a closed vessel filled with an isolating gas. It consists of two electrodes, the anode and cathode, in between which an electric field is applied. When a charged particle passes through the gasvolume, it loses its kinetic energy by interacting with the gasmolecules until it is in thermal equilibrium with the gas, leaving ion pairs along its track and in this way ionizing the gas. Under the influence of the applied electric field the formed free electrons and positive ions will drift to the anode and cathode, respectively. This movement induces an electric current in the external measuring chain. This current needs to be amplified for further handling of the data.

If all the electrons as well as all the positive ions are collected, the produced signal will be independent of the place of ionization and moreover it will be proportional to the amount of charge created. A disadvantage of such a configuration results from the fact that the positive ions drift almost 1000 times

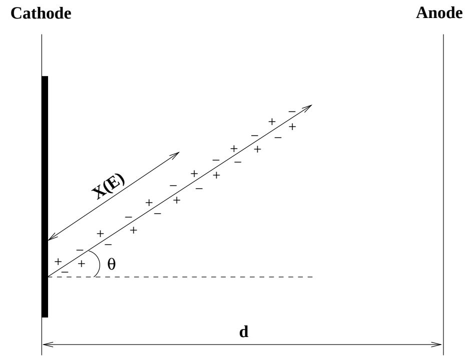

Figure 3.2: Schematic picture of the ionization process caused by a charged particle. Here the ionization chamber exists of two parallel plates with the sample mounted in the middle of the cathode.

slower towards the electrode than the corresponding electrons. Therefore such a configuration is not suitable for high count rates. To avoid this problem, the ionization chamber may be configured in such a way that the electrons drift to the anode within a time where the ions can be seen as static. These ions induce an electrostatic charge on the electrodes and the final collected charge is the one coming from the electrons minus the induced one from the ions. The latter is dependent on the place where the electron ion pair is produced, and thus so is the collected charge.

For the experiments in this work, the sample is placed in the middle of the cathode, which enables a 2π detection geometry. The anode is mounted parallel to the cathode. Both are aluminium foils fixed on a stainless steel frame. The charged particle leaves the sample under an angle θ with respect to the normal of the cathode, this is represented schematically in figure 3.2. As mentioned before, the signal registered will depend on the place of creation of the ionization and is given by [Ver90, BJ84]:

$$V = \frac{e\,N_0(E)}{C}\left(1 - \frac{X(E)}{d}\,cos\theta\right), \tag{3.1}$$

with:

- e the electron charge;
- N_0 the number of created electron ion pairs, depending on the energy of the charged particle;

- C the capacity of the ionization chamber;
- $X(E)$ the distance from the origin of the ionization track to the charge center of the ionization track;
- d the distance between the anode and the cathode;
- θ the angle between the ionization track and the normal of the cathode.

For mono-energetic particles with an isotropic angular distribution, the number of particles dN between θ and θ+dθ is proportional to:

$$dN \sim sin\theta \, d\theta. \tag{3.2}$$

Deriving equation 3.1 gives:

$$dV \sim sin\theta \, d\theta. \tag{3.3}$$

Combining 3.2 and 3.3 leads to:

$$\frac{dN}{dV} = c, \tag{3.4}$$

which shows that even mono-energetic particles with an isotropic angular distribution will cause a broad rectangular pulse heigth distribution [Ros49]. This situation is not very useful in order to seperate particles with different energies.

Frisch found a nice solution to this problem. He suggested to put a third electrode, the Frisch grid, between the anode and cathode on a suitable potential [Fri]. It typically consists of 0.1 mm thick steel wires, fixed in parallel at 1 mm intervals on a ring of stainless steel (see figure 3.3). The grid creates two completely independent electric fields in the chamber. As the sample is mounted on the cathode, the ionization should be limited to the region between cathode and grid. This can be acheived through the use of an optimal setup, as explained in the next subsection. A picture of the Frisch gridded ionization chamber used in this work is shown in figure 3.4. The grid shields the anode from the positive ions and in this way each created electron passes through the same potential difference between anode and grid and contributes equally to the anode signal pulse. Therefore, the amplitude of the signal will be independent of the position of formation of the original electron ion pair. The signal obtained is proportional to the total number of electron ion pairs formed along the track of the incident particle and corresponds to the energy of

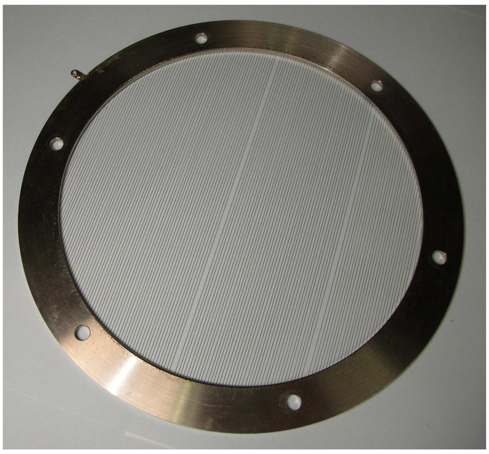

Figure 3.3: Picture of a Frisch grid.

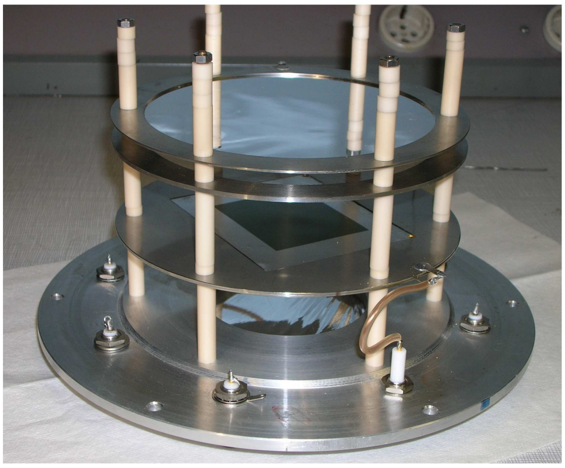

Figure 3.4: Picture of the ionization chamber used in most of the experiments of this work. The sample is mounted in the middle of the cathode, which is the lowest plate on the picture. The top plate is the anode and the plate in the middle is the Frisch grid.

the particle itself. Consequently, the anode pulse height signal V_A is expressed as [Ver90, BJ84]:

$$V_A = A_A \frac{e\,N_0(E)}{C} \sim E, \tag{3.5}$$

where A_A is the anode amplification factor.

The positive ions will induce a signal on the cathode proportional to formula 3.1:

$$V_C = A_C \frac{e\,N_0(E)}{C} \left(1 - \frac{X(E)}{d}\, cos\theta\right), \tag{3.6}$$

with A_C the amplification factor for the cathode.

3.2.2 Tuning of the detector

First of all, a suited detection gas should be chosen. To enhance the collection time of the electrons, the drift velocity in the gas must be as high as possible. A 'fast' detection gas is also important to reduce the hindrance of the γ-flash, which are the high energy γ-rays produced when the accelerated electrons hit the uranium target.

For ions in a gas, the drift velocity v can be accurately predicted from the relation [Kno89]:

$$v = \mu\,\frac{E}{P}, \tag{3.7}$$

with E the electric field strength, P the gas pressure and μ the mobility. The mobility tends to remain fairly constant over wide ranges of electric field and gas pressure. Pure methane has a high mobility for CH_4^+ ions: 2.26 (cm^2.atm)/(V.s) compared to 1.78 for an argon-methane mixture and even lower values for other gases or gas mixtures [Goe01]. Therefore, pure methane was chosen as detector gas. The electron drift velocity in methane and an argon-methane mixture is shown in figure 3.5. It shows that the electron drift velocity for methane has a saturation effect which permits different combinations of E and P without losing collection time. This leads to a first requirement for the setup of the ionization chamber when using CH_4:

$$\frac{E}{P} \geq 650 \left[\frac{V}{atm.cm}\right]. \tag{3.8}$$

Moreover, if the gas pressure is too high it can lead to recombination of the electrons and ions, leading to signal loss.

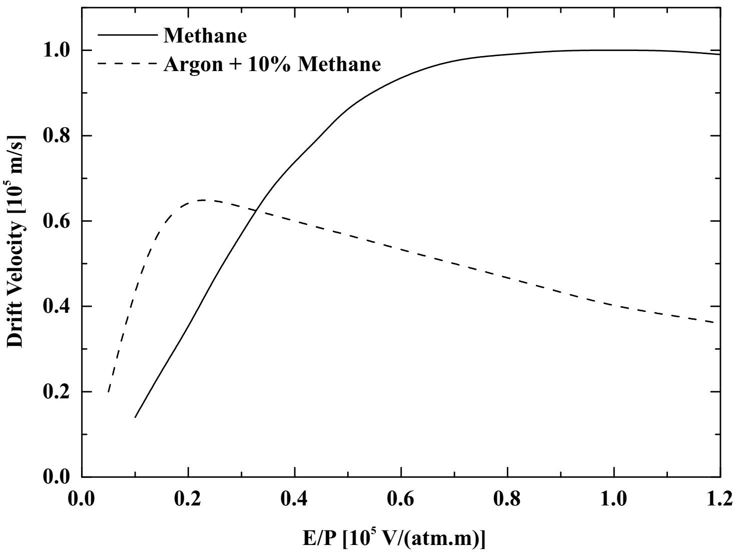

Figure 3.5: The electron drift velocity as a function of $\frac{E}{P}$ [Kno89], data from [Bor57].

Even though methane is not an electronegative gas and therefore no electron capture is possible, there may be impurities in the ionization chamber. O_2 and H_2O for example are more or less always present. They can capture an electron in their molecule which leads to recombination of these negative ions with the positive ions formed by the electron ion pairs [Fer01]. This leads to signal loss. To overcome this problem a continuous gasflow in the detector was used.

As explained before, the ionizing particles need to be stopped in the region between cathode and grid to obtain an anode signal which is independent of the creation place of the electron ion pairs. This imposes restrictions on the choice of the gas pressure as well as on the distance between grid and cathode. The range of α-particles and protons in methane for different gas pressures can be calculated with the computer program SRIM (Stopping and Range of Ions in Matter) [Zie]. This is illustrated in figure 3.6 for gas pressures of 1 atm and 2 atm in CH_4.

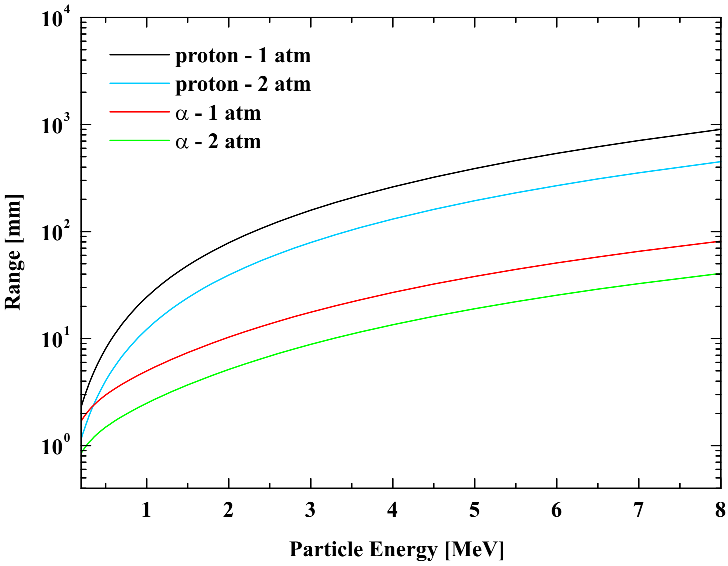

Figure 3.6: Range of α-particles and protons in methane at a pressure of 1 atm and 2 atm. The data are calculated with SRIM [Zie].

A last important point is connected to the Frisch grid. Since the wires have a certain thickness, some electrons will leak away via these wires. To reduce this effect as much as possible, no electric field lines should end on these wires. This is the case if the following condition is fulfilled [Ver90]:

$$\frac{E_A}{E_C} = \frac{\frac{V_A - V_G}{d_{AG}}}{\frac{V_C - V_G}{d_{CG}}} \geq \frac{1 + \frac{2\pi r}{g}}{1 - \frac{2\pi r}{g}}, \tag{3.9}$$

where E_A and E_C are the electric fields at the anode and cathode, d_{AG} and d_{CG} respectively the distance between anode and grid and between cathode and grid, r the wire radius and g the distance between two wires. As mentioned in the previous subsection, the Frisch grid used in this work was made of 0.1 mm thick wires with interval distances of 1 mm. Therefore, the last requirement for the setup of the ionization chamber can be reduced to:

$$\frac{E_A}{E_C} \approx 2. \tag{3.10}$$

It is clear that it is difficult to meet these three requirements. For example, on the one hand the gas pressure needs to be high enough to stop the ionizing particles in the region between cathode and grid, but on the other hand a too high gas pressure can lead to recombination of the electrons and ions. Therefore, the final tuning of the ionization chamber is always a compromise and depends on the specific reaction under investigation. The tuning for the different measurements is mentioned in chapters 4, 5 and 6.

3.3 Data acquisition

A scheme of the electronic setup is shown in figure 3.7. The signals from the anode and cathode are sent to an amplifier (A) via a preamplifier (PA). Next, they are led to an analog-to-digital converter (ADC), where the pulse

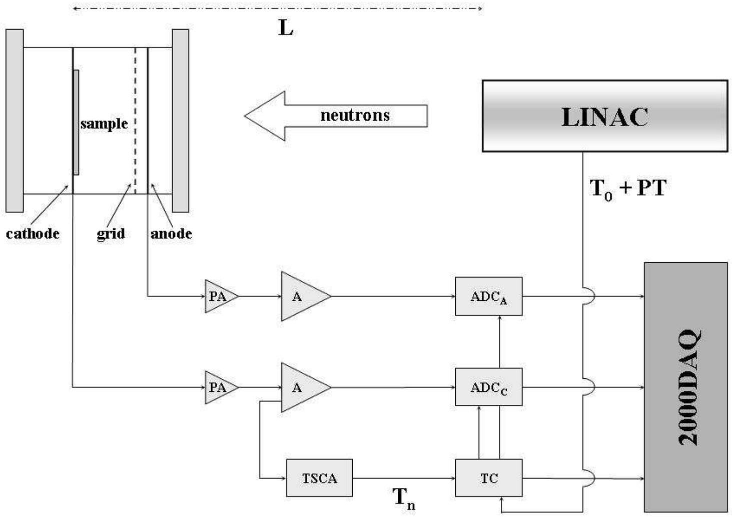

Figure 3.7: Schematic picture of the electronic setup used for the TOF measurements at GELINA.

heights are converted into a channel number. A second signal is sent from the amplifier on the cathode side to a timing single channel analyser (TSCA). The latter imposes a lower and upper level on the incoming signal which permits a first selection on the pulse heights. When the pulse height lies between the predefined levels, a fast signal T_n, which serves as a stop signal, is sent to a time coder (TC). The start signal T_0 is generated by the LINAC and is sent to the time coder just before the electrons impinge on the uranium target. The time coder calculates the difference between T_n and T_0 for each event and converts it into a TOF channel number. Furthermore, the LINAC generates a second signal: the pretrigger (PT). This signal is sent to the time coder 2 μs before and independent of the T_0 signal. It resets the time coder, and prevents that the time coder calculates a TOF during interruptions of the LINAC. In addition to the TOF conversion, the time coder sends an ‘event accept’ signal to both ADCs. The anode signal as well as the cathode signal are each delayed in such a way that both signals coincide with the ‘event accept’ signal. Only when they are coincident, the ADC will handle the signal. At this point both ADC and TOF channel numbers are handled by the data acquisition system 2000DAQ, developed at the IRMM [Gon97] and can be stored on a PC. For each event, a triplet of coincident data (ADC1, ADC2 and TOF) is generated and stored on a disk, enabling an off-line analysis. This way of recording events is called list mode. Moreover, during the experiment, the data acquisition system displays histograms of both ADCs and the TOF on a PC screen, enabling a continuous control of the experiment.

3.4 The time-of-flight method

As mentioned in the beginning of this chapter, the time-of-flight (TOF) method is a very suitable technique to determine the energy of neutrons coming from a pulsed beam with a wide energy range. The neutron energy E_n is derived from the time t a neutron needs to travel a known distance L from the production target to the experimental setup. During the data processing the TOF is converted into neutron energy in a fully relativistic way. However, in this work the neutron energy is below a few hundred keV. This permits to use the non-relativistic approach to write down the neutron energy:

$$E_n \;=\; \frac{1}{2}\, m_n\, v^2$$

$$
\begin{aligned}
&= \frac{1}{2} m_n \left(\frac{L}{t}\right)^2 \\
E_n\,[eV] &= \left(72.298\,\frac{L\,[m]}{t\,[\mu s]}\right)^2, \qquad (3.11)
\end{aligned}
$$

where m_n is the neutron mass, L the flight path length and t the measured time-of-flight. In practice t must be corrected for the delay in the electronics and cables (see section 3.4.2). The neutron production in the target is accompanied by a huge amount of γ-radiation, the so-called γ-flash. This blinds the detector for a certain time - depending on the detector characteristics - and causes a limitation in the energy range at a certain distance. Equation 3.11 shows that, this 'blinding time' being fixed, higher energy ranges can be covered at longer flight paths. From equation 3.11 it is clear that uncertainties on the time measurement (Δt) and on the effective distance travelled by the neutron (ΔL) affect the energy uncertainty as follows:

$$\frac{\Delta E_n}{E_n} = 2\sqrt{\left(\frac{\Delta t}{t}\right)^2 + \left(\frac{\Delta L}{L}\right)^2}. \qquad (3.12)$$

Using equation 3.11, relation 3.12 becomes:

$$\frac{\Delta E_n}{E_n} = \frac{2}{L\,[m]}\sqrt{\frac{E_n\,[eV]}{5227.039}\,\Delta t\,[\mu s]^2 + \Delta L\,[m]^2}. \qquad (3.13)$$

Equation 3.13 clearly shows that the flight path length plays a positive role in the achievable energy range as well as in the energy resolution: the longer the flight path the better the energy resolution. However, the neutron flux is proportional to 1/L^2. Therefore one should always try to find a good compromise between resolution, neutron flux and energy range, depending on the application.

Several phenomena affect the resolution. We can see from equation 3.12 that some are due to uncertainties on the time-of-flight and others on the flight path length. The time dependent component is mainly determined by:

- the finite duration of the electron burst;
- the finite time bin width of the electronics and data acquisition system;
- the promptness of the detector response.

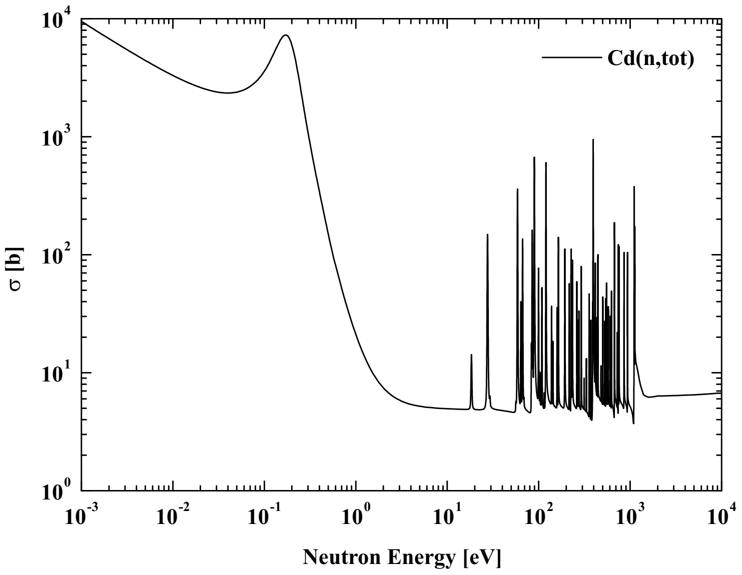

Figure 3.8: The neutron absorption cross section for Cd, taken from ENDF/B-VI [end].

The component depending on the effective flight path length ΔL results from the neutron transport in the moderator. This neutron 'mean free path' in the moderator turns out to be nearly constant as a function of the neutron energy. Therefore, the neutron transport in the moderator is generally taken as an uncertainty in flight path length. This implicates that the resolution strongly depends on the angle between the flight path and the normal to the moderator.

3.4.1 Overlap filter

In TOF measurements one has to make sure that fast neutrons of one pulse do not catch up with the slow neutrons of a previous pulse. At 800 Hz, the frequency mostly used at GELINA, the time span between two bursts is 1.25 ms. Therefore, all the neutrons which need more than 1.25 ms to travel the distance to the sample have to be eliminated from the neutron beam. This is done by placing an overlap filter in the neutron beam, thick enough to stop all the neutrons with a flight time longer than the cycle period of

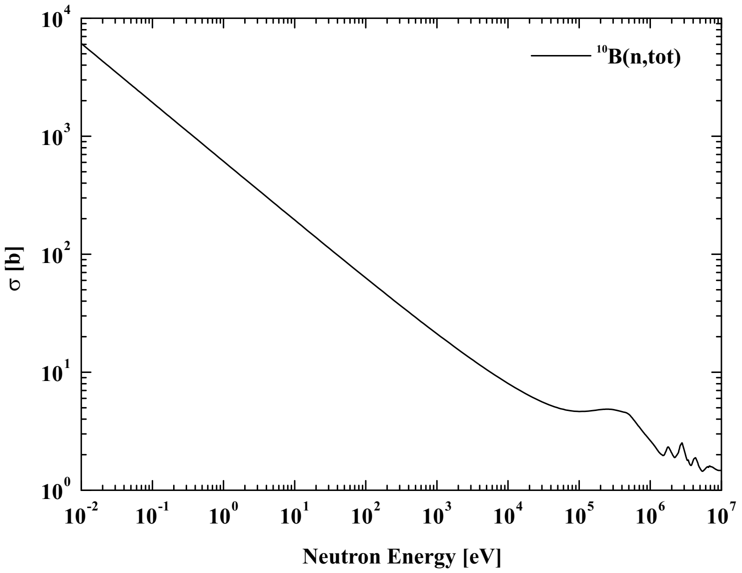

Figure 3.9: The neutron absorption cross section for ^{10}B, taken from ENDF/B-VI [end].

the LINAC, but thin enough to let the other neutrons through as much as possible. At 8.5 m, 1.25 ms corresponds to a neutron energy of 0.24 eV and a Cd filter is used. Figure 3.8 shows that Cd is a good choice, because of the very high neutron absorption cross section below 0.3 eV. For a 30 m flight path however, Cd is not satisfactory, because in this case all the neutrons with an energy below 3 eV have to be filtered out. Here boron is used because it has a very high (n,α) thermal neutron absorption cross section with a 1/v-behaviour up to approximately 100 keV (see figure 3.9).

3.4.2 Timing signals

As explained in section 3.1, a large number of high energy γ-rays is generated when the electrons hit the uranium target. This γ-flash temporarily saturates the detection system. Since the γ-rays have a much higher velocity than the neutrons and hence reach the detector earlier, a delay time T_{delay} may be imposed on the time coder so that no event is recorded during this time interval, avoiding an overload in the associated electronics. Such a delay time

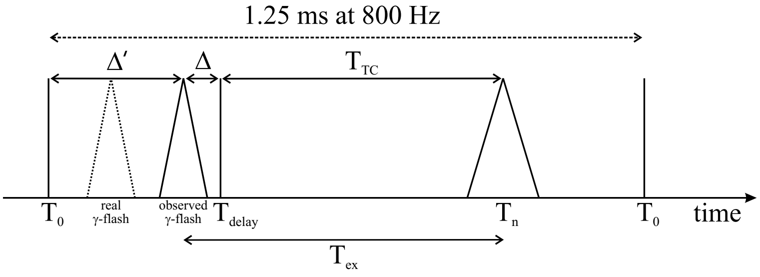

Figure 3.10: The different timing signals during one linac cycle.

must be taken into account when calculating the neutron TOF. The recorded TOF T_{TC} corresponds to the elapsed time between the detection of an event T_n and the T_0 signal, decreased by the imposed delay T_{delay}:

$$T_{TC} = T_n - T_0 - T_{delay}. \tag{3.14}$$

Figure 3.10 shows the different timing signals and events. The T_0 signal from the LINAC corresponds with a time just before the electron beam impact on the uranium target. The γ-flash is produced when the electrons interact with the uranium atoms. Since most neutrons are created by (γ,n) and (γ,f) reactions between these γ-rays and the uranium target, the γ-flash corresponds to the true start of the neutron emission, this is indicated with 'real γ-flash' in figure 3.10. In addition to the neutron TOF, several timing effects delay the recorded TOF, e.g.: the time to collect the electrons and positive ions in the ionization chamber and the time to send the information from the ionization chamber to the DAQ system, strongly affected by the length of the cables used. One can assume that these delay effects are more or less equal for the signals caused by the γ-flash and the ones coming from the charged particles under investigation. As a result, the measured γ-flash, indicated with 'observed γ-flash' in figure 3.10, is the true T_0. Therefore, the exact TOF of the interacting neutron T_{ex} can be calculated as follows:

$$\begin{aligned} T_{ex} &= T_{TC} + T_{delay} - \Delta' \\ &= T_{TC} + \Delta. \end{aligned} \tag{3.15}$$

Equation 3.15 shows two possibilities to determine the unknown factor Δ':

1. By putting $T_{delay} = 0$ and measuring the γ-flash. Because $T_{ex} = 0$ for the γ-flash, equation 3.15 shows that $T_{TC} = \Delta'$.

2. By measuring a well known narrow resonance for which T_{ex} can be calculated from equation 3.11. From the measured T_{TC}, T_{delay} - $\Delta' = \Delta$ is determined.

In this explanation the TOF of the γ-rays has been neglected. However, when the delay factor is determined in the second way using a well known resonance, it is not necessary to include their TOF in the formula.

3.5 Data reduction

The total observed count rate $Y_X(E_n)$ for a neutron induced reaction denoted as X(n,c.p.)Z, with c.p. a proton or α-particle in this work, as a function of the neutron energy is:

$$Y_X(E_n) = \epsilon_X \, N_X \, \sigma_X(E_n) \, \varphi(E_n) + BG_X(E_n), \tag{3.16}$$

with:

- ϵ_X the detector efficiency;
- N_X the number of atoms/cm^2 in the target;
- $\sigma_X(E_n)$ the cross section for the studied reaction as a function of the neutron energy;
- $\varphi(E_n)$ the neutron flux as a function of the neutron energy;
- $BG_X(E_n)$ the number of observed background counts as a function of the neutron energy.

Y_X, φ and BG_X are normalized on the basis of the CM, to rule out fluctuations in φ during the measurement. The cross section as a function of the neutron energy can now be written as:

$$\sigma_X(E_n) = \frac{Y_X(E_n) - BG_X(E_n)}{\epsilon_X \, N_X \, \varphi(E_n)}. \tag{3.17}$$

So, to determine the cross section as a function of the neutron energy, $\varphi(E_n)$, $BG_X(E_n)$ and ϵ_X have to be known. The next paragraphs will explain that in general four different measurements need to be performed to determine $\sigma_X(E_n)$. It is preferable that the experimental conditions for all four measurements are identical.

Material	Energy [eV]
Rh	1.257
Au	4.906
W	18.83
Co	132
Mn	336 and 2370

Table 3.1: Energy position of the black resonance for each filter.

3.5.1 Flux measurement with ^{10}B

The moderated neutrons from the LINAC have a broad neutron energy spectrum (see section 3.1). To determine the energy dependent neutron flux $\varphi(E_n)$, the well known ^{10}B(n,α)^{7}Li reaction cross section is used, by placing a ^{10}B sample with a well defined thickness in the ionization chamber. Following equation 3.16, the observed normalized ^{10}B(n,α) count rate $Y_B(E_n)$ can be written as:

$$Y_B(E_n) = \epsilon_B \, N_B \, \sigma_B(E_n) \, \varphi(E_n) + BG_B(E_n). \tag{3.18}$$

So, the flux $\varphi(E_n)$ can be calculated as follows:

$$\varphi(E_n) = \frac{Y_B(E_n) - BG_B(E_n)}{\epsilon_B \, N_B \, \sigma_B(E_n)}. \tag{3.19}$$

$\sigma_B(E_n)$ is well known and can be taken from an evaluated nuclear data library such as JEFF-3.1 [jef], ENDF/B-VI [end] or JENDL-3.3 [jen]. In equation 3.19 the only unknown terms remaining are $BG_B(E_n)$, the energy dependent background counts, and the detector efficiency ϵ_B. The determination of the detector efficiency ϵ_B for this work is outlined in subsection 3.5.3. Since the background has several origins and since it is energy dependent, it is necessary to determine the background contribution over the whole energy range. The main background sources are the intrinsic background from the detector, unwanted reactions in the target, reactions induced by scattered neutrons, natural background and γ-radiation in the neutron beam.

To find the background contribution in the flux measurement, a second flux measurement with so called black resonance filters in the neutron beam is performed. These filters are materials which have strong neutron absorption resonances at specific energies. To span a broad neutron energy interval, the materials chosen as black resonance filters are: Mn, Co, Rh, Au and W. For each filter, the energy position of the resonance which is used as black resonance is listed in table 3.1. By chosing the appropriate thickness of these materials so that all the neutrons with these well known energies are taken out of the neutron beam, neutrons from the direct burst (thus with these energies) cannot cause any reaction in the sample. If there are counts remaining at these specific energies (or TOF), these counts are due to background. The energy dependent background can now be estimated by fitting a function through the count rates at these energy (TOF) zones. For all the measurements in this work, the fit to the TOF spectra is performed with this power function:

$$BG(t) = a + bt^c, \tag{3.20}$$

with a, b and c adjustable fit parameters. The obtained background can then be subtracted from the flux count rate.

In principle, the moderated neutron flux $\varphi(E_n)$ above a few eV can be described by:

$$\frac{d\varphi(E_n)}{dE} = K{E_n}^{\alpha(E_n)}, \tag{3.21}$$

with K a constant and $\alpha(E_n)$ a function of the energy. K depends on the flight path and the operation mode of the linac. $\alpha(E_n)$ depends on the material and the dimensions of the moderator and can be expressed as:

$$\alpha(E_n) = a_0 + a_1\sqrt{E_n} + a_2 E_n. \tag{3.22}$$

Because in this work the neutron TOF is measured, the flux per unit of TOF $\frac{d\varphi}{dt}$ is obtained. The corresponding expression for the flux can be calculated as follows:

$$\frac{d\varphi(E_n)}{dt} = \frac{d\varphi}{dE}\frac{dE}{dt}. \tag{3.23}$$

Making use of equation 3.11 equation 3.23 becomes:

$$\begin{aligned} \frac{d\varphi(E_n)}{dt} &= K{E_n}^{\alpha(E_n)} C{E_n}^{\frac{3}{2}} \\ &= K'{E_n}^{\alpha(E_n)+\frac{3}{2}} \\ &= K'{E_n}^{\alpha'(E_n)}. \end{aligned} \tag{3.24}$$

So, the neutron flux can be fitted with formula 3.24. The result of a fit through

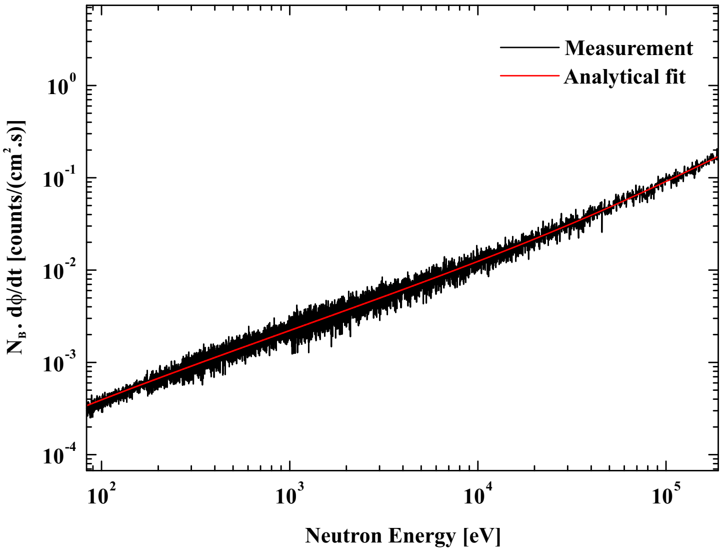

Figure 3.11: The moderated neutron flux multiplied with the number of ^{10}B atoms at 30 m distance from the uranium target with the accelerator operated at 800 Hz.

coefficient	FP12-30m	FP13-8.5m
a_0	6.65×10^{-1}	5.65×10^{-1}
a_1	2.23×10^{-4}	4.46×10^{-4}
a_2	-1.50×10^{-7}	-5.19×10^{-7}

Table 3.2: Coefficients to describe the neutron flux obtained after a fit through the experimental data points.

experimental data points of a ^{10}B flux measurement is shown in figure 3.11. In this figure the moderated neutron flux is multiplied with N_B, the number of ^{10}B atoms/cm^2 in the ^{10}B sample used. The measurement is performed at flight path 12 at a distance of 30 m with the linac operating at 800 Hz. A similar fit is done for flight path 13 at 8.5 m, the second flight path used during the measurements. The obtained parameters for $\alpha'(E_n)$ are listed in table 3.2.

3.5.2 Measurement with the sample to investigate

A third measurement is performed with the sample for which we want to investigate the reaction cross section. As the background can be dependent on the sample, a fourth measurement with black resonance filters is required, from which $BG_X(E_n)$ can be determined in the same way as described above for the flux measurement. Substitution of equation 3.19 in equation 3.17 results in a final expression to determine the differential cross section $\sigma_X(E_n)$ for the reaction of interest:

$$\sigma_X(E_n) = \frac{\epsilon_B}{\epsilon_X} \frac{Y_X(E_n) - BG_X(E_n)}{Y_B(E_n) - BG_B(E_n)} \frac{N_B}{N_X} \sigma_B(E_n). \tag{3.25}$$

ϵ cancels out if the detector efficiency is the same for both reactions. In this work, both reactions have been measured with the same detector and in the same experimental conditions, so $\frac{\epsilon_B}{\epsilon_X}$ is approximately 1. However, the ^{10}B atoms have a light mass and the influence of the COM velocity may not be neglected when the energy of the impinging neutrons becomes high, as this results in a sligthly anisotropic emission of the reaction products. Therefore, ϵ_B is not exactly equal to ϵ_X. Once corrected for this anisotropy, ϵ cancels out. In the next subsection 3.5.3 it is explained how the detector efficiency as a function of the neutron energy is determined.

As seen before, each event is stored as a triplet of data (ADC1, ADC2, TOF). With a first analysis program, a particle selection on the ADC spectra can be performed giving the corresponding TOF spectrum. Then the data processing code AGS (Analysis of Geel Spectra) [Bas97] is used. This program performs the manipulations necessary to derive $\sigma_X(E_n)$ (see equation 3.25) from the obtained TOF spectra such as: background fitting and subtraction, normalization and TOF-to-energy conversion.

3.5.3 Detector efficiency

In section 1.1.2 it was mentioned that for compound nucleus reactions, the emitted particles have an isotropic angular distribution in the COM. However, for light mass nuclei the influence of the COM velocity may not be neglected when the energy of the impinging neutrons becomes high. At those energies, when measuring in an upstream 2π detection geometry, counts fall outside the 2π angle in the LAB system. The velocity of the emitted charged particles c.p., α-particles and protons in this work, in the LAB system is:

$$\vec{v}_{c.p.,LAB} = \vec{v}_{c.p.,COM} + \vec{v}_{COM}, \tag{3.26}$$

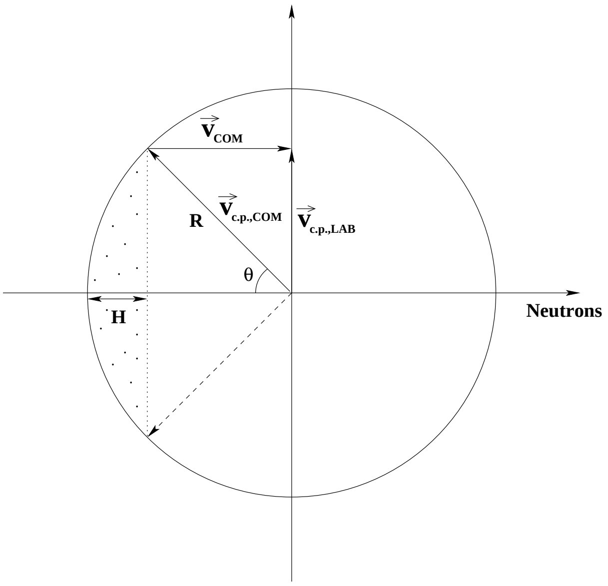

Figure 3.12: Representation of the detector. Only these particles for which $\vec{v}_{c.p.,LAB} \cdot \vec{v}_{n,LAB} \leq 0$ will be detected in a 2π upstream measurement.

and the velocity of the interacting neutrons is:

$$\vec{v}_{n,LAB} = \vec{v}_{n,COM} + \vec{v}_{COM}. \tag{3.27}$$

When the coordinate system is chosen so that the X axis is parallel with the incoming neutron, one has:

$$v_{n,LAB} = v_{n,COM} + v_{COM}. \tag{3.28}$$

To correct for the anisotropy in the LAB system, the efficiency of the detector has to be expressed as a function of the neutron energy. To do this, one should calculate that fraction of the solid angle for which $\vec{v}_{c.p.,LAB} \cdot \vec{v}_{n,LAB} \leq 0$ (see figure 3.12). It is this region which will be seen in the LAB 2π upstream detection. Using the symbols from figure 3.12, the surface S of the dotted part becomes:

$$S = 2\pi RH. \tag{3.29}$$

The fraction F of the solid angle for which $\vec{v}_{c.p.,LAB} \cdot \vec{v}_{n,LAB} \leq 0$ can be written as:

$$\begin{aligned} F &= \frac{2\pi RH}{4\pi R^2} \\ &= \frac{H}{2R} \\ &= \frac{1 - cos\theta}{2} \\ &= \frac{1}{2} - \frac{1}{2}\frac{|v_{COM}|}{|v_{c.p.,COM}|}. \end{aligned} \tag{3.30}$$

If m_T represents the mass of the nuclei in the sample, then it follows from nuclear reaction theory that [Hey99]:

$$\begin{aligned} v_{COM} &= \frac{m_n}{m_T} v_{n,COM} \\ &= \frac{m_n}{m_T}(v_{n,LAB} - v_{COM}) \\ &= v_{n,LAB}\frac{m_n}{m_n + m_T}, \end{aligned} \tag{3.31}$$

For $v_{c.p.,COM}$ the following applies:

$$v_{c.p.,COM} = \sqrt{\frac{2E_{c.p.}}{m_{c.p.}}}c. \tag{3.32}$$

In this work the charged particles are detected in a 2π upstream direction, therefore the efficiency ϵ of the detector as a function of the neutron energy is:

$$\begin{aligned} \epsilon &= \frac{F}{0.5} \\ &= 1 - \frac{v_{COM}}{v_{c.p.,COM}} \\ &= 1 - \frac{\sqrt{m_n m_{c.p.}}}{m_n + m_T}\sqrt{\frac{E_n[eV]}{E_{c.p.}[MeV]}} \times 10^{-3} \\ &= 1 - C\sqrt{E_n[eV]}. \end{aligned} \tag{3.33}$$

By dividing the measured counts with this efficiency, the real counts that should have been measured for a certain neutron energy can be calculated. In

Reaction	C [$\times 10^{-5}$]	E_f [keV]	ϵ [%]
^{10}B(n,α)	13.630	45	97.1
^{10}B(n,α)	13.630	250	93.2
^{26}Al(n,α)	4.6794	45	99.0
^{36}Cl(n,α)	3.6669	250	98.2
^{36}Cl(n,p)	1.9923	250	99.0
^{41}Ca(n,α)	2.2035	45	99.5

Table 3.3: C-values for each reaction studied in this work together with the efficiency of the detector for the upper energy limit E_f of the covered energy region.

table 3.3 the values for C are listed for each reaction studied in this work. In addition, the efficiency of the detector for each reaction for the upper energy limit E_f of the covered energy region is calculated and listed in table 3.3. Based on these values, the efficiency of the detector is taken into account only for the ^{10}B(n,α) flux determinations. For the ^{36}Cl(n,α) reaction, it was not necessary to take the efficiency into account as only for the first resonance at 0.93 keV a significant α-contribution was found. Figure 3.13 shows the efficiency of the detector for the ^{10}B(n,α) reaction. It shows that only for high neutron energies ϵ deviates from 1 and the detector will not detect all the emitted charged particles in the 2π upstream direction. It has been verified that it is not necessary to follow the relativistic approach in this work, as the energy difference for the emitted charged particles is negligible.

3.6 The neutron energy resolution

The measured shape of a resonance does not correspond with its natural shape, as it is broadened during a measurement by several phenomena such as the promptness of the detector response and uncertainties on the flight path length. As a consequence the determination of the resonance parameters requires an accurate description of the resolution of GELINA and a knowledge of the detector resolution [Coa83, Sow88]. Apart from that, the nuclei in the sample are not at rest. The thermal motion of the atoms in the target gives rise to a Doppler broadening which must be taken into account. These broadening effects are represented by Gaussian functions and can be combined quadratically to find the total experimental broadening. A description of the

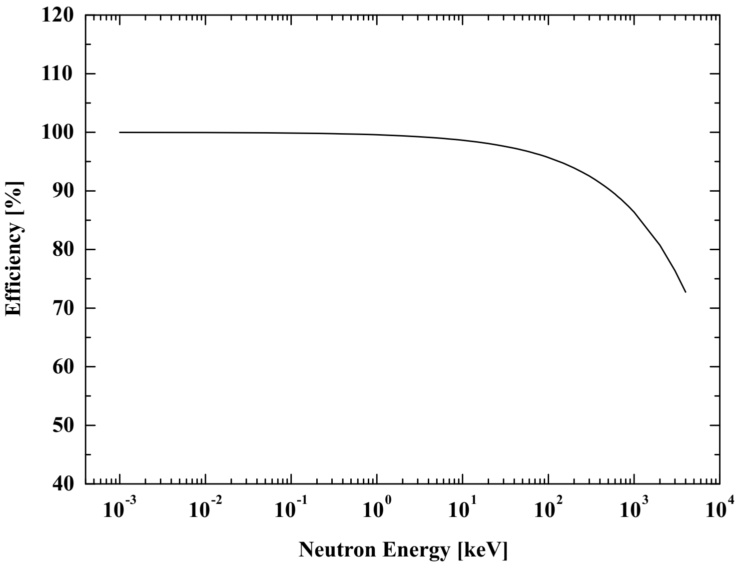

Figure 3.13: Efficiency of the detector for the ^{10}B(n,α) reaction.

three components mentioned is given below. It has to be stressed that the Breit-Wigner expression to describe the resonance cross section does not take into account these experimental broadening effects.

3.6.1 Doppler broadening

As mentioned in the introduction of this section, the target nuclei have a non-negligible thermal motion. They have a distribution of velocities depending on the sample and its temperature, which lead to a Doppler broadening. The Doppler FWHM of the Gaussian distribution at a resonance energy E_{res} is given by Δ_D [Gre99]:

$$\Delta_D[eV] = \sqrt{\frac{16\, ln2\, k\, T_{eff}\, E_{res}}{A}}, \tag{3.34}$$

with k the Boltzmann constant and A the mass number of the target nucleus. The effective temperature of the target T_{eff} in the Debeye model is given by:

$$T_{eff}[K] = \frac{3}{8}\, T_D\, coth\left(\frac{3}{8}\,\frac{T_D}{T}\right), \tag{3.35}$$

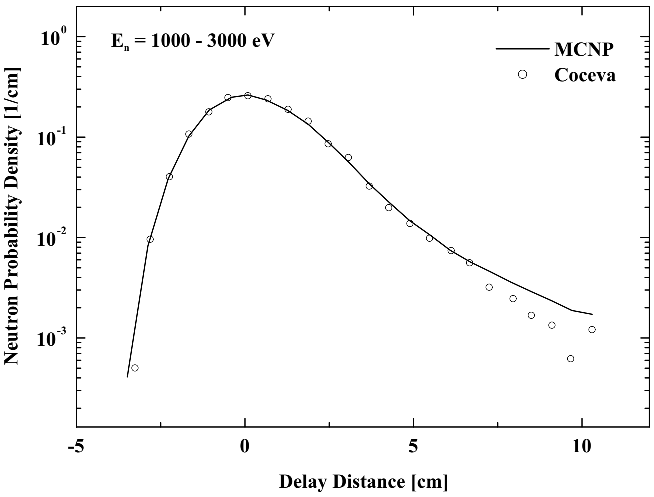

Figure 3.14: Comparison of the resolution function obtained by Coceva and Magnani [Coc96] with the one obtained by Flaska *et al.* [Fla04] from Monte Carlo simulations using MCNP for FP13-8.5m.

where T is the sample temperature and T_D the Debeye temperature, which can be found in [tde].

3.6.2 Resolution of GELINA

The various phenomena which affect this resolution have been listed in section 3.4. The different components are considered to be independent and are convoluted with each other to obtain their total contribution to the experimental broadening as a function of the neutron energy. In this work only on the uncertainty arising from the uranium target and the moderator will be focused, because the other components are more or less negligible, except for the resolution of the ionization chamber which will be discussed in the next subsection (3.6.3). The first description of the resolution of GELINA was based on the analytical expressions of Moxon [Mox91]. Later Coceva and Magnani [Coc96] developed an ad-hoc Monte Carlo code. Recently, similar simulations have been performed by Flaska *et al.* [Fla04] using the MCNP-4C2 code [Bri00]. The results of these calculations are in excellent agreement with the resolution functions proposed by Coceva and Magnani (see figure 3.14). Because these

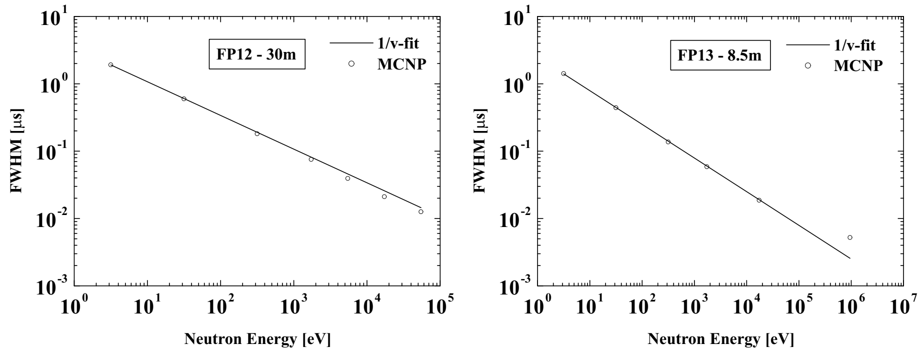

Figure 3.15: Contribution of the GELINA target and moderator to the total experimental broadened resonance width as a function of the neutron energy for the two different flight paths used in this work: FP12-30m (left) and FP13-8.5m (right).

resolution functions are dependent on the angle between the flight path and the normal to the moderator, they must be calculated for each flight path. From these resolution functions, the contribution from the GELINA target and moderator to the experimental broadening can be calculated for different flight paths and as a function of the neutron energy. Figure 3.15 shows the result for the two different flight paths used in this work: FP12-30m and FP13-8.5m. FP12 makes an angle of 117° with the incoming neutron beam, while the angle for FP13 is 108°. For both flight paths, a $1/v$-fit can be performed and the FWHM of the moderator resolution is given by Δ_M:

$$FP12 - 30m, 117^\circ \quad : \quad \Delta_M[\mu s] = \frac{3.3}{\sqrt{E[eV]}}, \tag{3.36}$$

$$FP13 - 8.5m, 108^\circ \quad : \quad \Delta_M[\mu s] = \frac{2.5}{\sqrt{E[eV]}}. \tag{3.37}$$

3.6.3 Resolution of the ionization chamber

In this work ionization chambers are used to detect the charged particles. To determine the resolution of the chamber used, a transmission measurement with a ^{10}B sample in the chamber and a ^{27}Al filter as transmission sample was performed. The experimental conditions are completely the same as for the (n,p) and (n,α) measurements. In a transmission measurement the fraction of

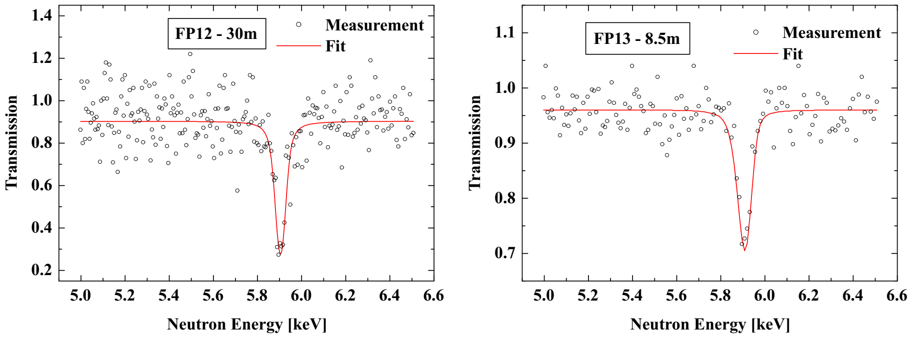

Figure 3.16: A fit by REFIT through the 5.9 keV ^{27}Al transmission to determine the resolution of the ionization chambers used. The plot on the left hand side is the one for the bigger chamber used at FP12-30m while the right hand one is the fit for the small chamber at a lower gas pressure at FP13-8.5m.

the neutron beam that crosses the transmission filter without any interaction is determined. This means that the ratio of the count rates from a filter-in (Y_{in}) and filter-out (Y_{out}) measurement has to be determined. This ratio is called the transmission factor T and is related to the total cross section σ_{tot}:

$$T = \frac{Y_{in}}{Y_{out}} \simeq e^{-n\sigma_{tot}}, \tag{3.38}$$

with n the thickness of the filter in atoms/barn. For the normalization to the same neutron flux, the CM is used. In principle, the background contribution to the count rates must be taken into account. The transmission is then given by:

$$T = \frac{Y_{in} - BG_{in}}{Y_{out} - BG_{out}}. \tag{3.39}$$

The resonance parameters of ^{27}Al are known and are available in the different evaluated nuclear data libraries. A ^{10}B sample is used, because the ^{10}B(n,α)^{7}Li cross section is well known and has a $1/v$-shape, so there is no hindrance from resonances coming from the ^{10}B(n,α) cross section. Except for the time resolution of the ionization chamber used, all the other components affecting the broadening of the measured transmission are known. Under these circumstances the chamber resolution can be determined by fitting the measured transmission. This is done with the REFIT program [Mox91]. It incorporates

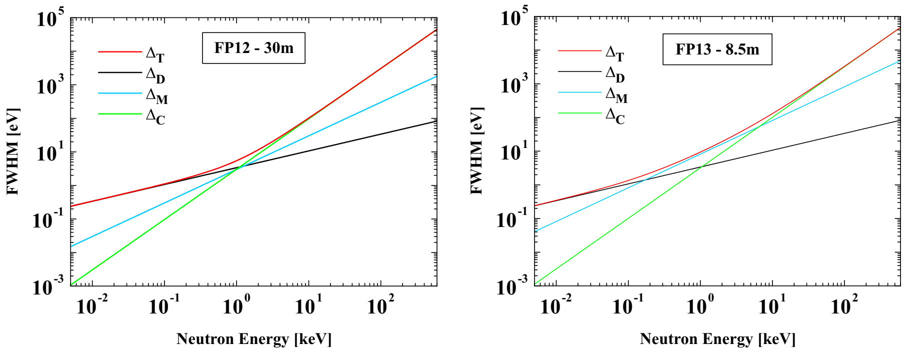

Figure 3.17: Total contribution to the experimental broadening of a measured resonance in the case of ^{27}Al as a function of the neutron energy for the two different flight paths used in this work: FP12-30m (left) and FP13-8.5m (right). The contributions from the different components are shown as well.

all the different components resulting in the broadening function as well as a resonance parameter file for ^{27}Al taken from JENDL-3.3 [jen]. The sharp resonance at 5.9 keV has been chosen for the fit. The time resolution resulting from the used ionization chamber turned out to be 106 ± 18 ns for FP12-30m and 31 ± 8 ns for FP13-8.5m. The fit results are shown in figure 3.16. This difference is caused by the dimensions of the chamber and probably by the gas pressure. For the measurement at FP12 a bigger chamber was used at a higher methane pressure than the measurements performed at FP13. The difference in transmission comes from the difference in thickness of the aluminium filter which was thicker for the FP12 measurement.

3.6.4 Total neutron energy resolution

Insight into the energy dependent total resolution (Δ_T) of an experiment can be obtained by quadratically combining the Doppler broadening, the GELINA resolution (data of M. Flaska [Fla04]) and the resolution of the ionization chamber. This is illustrated in figure 3.17 for the two flight paths used in this work. One can see that for energies higher than 2 keV and 10 keV for FP12-30m and FP13-8.5m respectively, the total resolution is completely determined by the ionization chamber. This shows that knowledge of the ionization chamber resolution is very important in the experiments performed in this work.

A = 27	L = 30m		L = 8.5m	
	Δt [ns]	ΔE [eV]	Δt [ns]	ΔE [eV]
Δ_D	19.6	8.2	5.6	8.2
Δ_M	43.0	18.0	32.5	48.0
Δ_C	106.0	44.3	31.0	45.7
Δ_T	116.1	48.5	45.3	66.8

Table 3.4: Different contributions to the total experimental broadening for the resonance at 5.9 keV in ^{27}Al. The different contributions are compared for the two different flight paths.

As illustration, the different contributions to the experimental broadening at an energy of 5.9 keV are listed in table 3.4 in the case of ^{27}Al for both flight paths.

3.7 Sample preparation

The uncertainty on the total number of atoms in a sample is very often the main source of uncertainty in cross section measurements [Wag89]. Therefore the preparation and subsequent mass determination of the sample used are prerequisites for an accurate determination of the reaction cross section. All samples have an effective area of 6×5 cm^2 and are fixed on a 9.5×8 cm^2 metal frame. The backing material of the samples needs to be conductive, since the samples are placed in the cathode of the ionization chamber (see section 3.2). Moreover, the backing material should not have too many resonances in the energy region of interest. It must be stressed that the deposition of the sample material has to be homogeneous as the weight per cm^2 will be used to determine the reaction cross section. Moreover, inhomogeneity degrades the energy resolution of the emitted particles. All samples used in the experiments were available at the start of this work.

3.7.1 ^{36}Cl sample

The ^{36}Cl sample was prepared at the IRMM by vacuum deposition of silver chloride on an aluminium foil, which ensures the homogeneity of the layer. This resulted in a ^{36}Cl enrichment of 40.50 %. To avoid reaction of the silver chloride with the aluminium foil, the latter is covered with a platinum coating.

No use was made here of sodium or potassium chloride because they are more hygroscopic. They will draw moisture from the atmosphere and eventually they will cristallize.

To determine the number of ^{36}Cl atoms ($N_{36_{Cl}}$), the sample was irradiated with thermal neutrons at the High Flux Reactor of the ILL (France). By detecting the protons (Y_p) of the measured ^{36}Cl(n$_{th}$,p)^{36}S reaction [Wag96], the ^{36}Cl atoms could be calculated from:

$$Y_p = \sigma_{36}\, N_{36}\, \varphi_n, \tag{3.40}$$

with φ_n the neutron flux from the reactor, which was determined via the well known thermal neutron induced fission cross section of ^{235}U, and σ_{36} the known cross section of the ^{36}Cl(n$_{th}$,p)^{36}S reaction. The sample used in this measurement contained $(1.39 \pm 0.07) \times 10^{19}$ ^{36}Cl atoms. More details about the preparation and thickness determination of the ^{36}Cl sample can be found in [Eyk91].

3.7.2 ^{26}Al sample

The preparation of the ^{26}Al sample was done in two steps. First, the ^{26}Al was produced at the Los Alamos National Laboratory (USA) by spallation of a KCl target with a proton beam and purification by ion exchange. This resulted in a ^{26}Al/^{27}Al ratio of 0.1. To deposit as much as possible of the produced ^{26}Al, electrodeposition of the Al solved in a HCl solution was used in a second step at the IRMM. This method has already been applied succesfully several times at the IRMM for the preparation of other samples [Ing97, Ing99]. The method relies on the migration of positive or negative species to a substrate of appropriate polarity and precipitation as a compound. To check wether this method could be used for ^{26}Al as well, several tests were performed with natural aluminium. Because a deposition of ^{27}Al on an aluminium backing cannot be visualised, a nickel foil was chosen as backing material.

The mass determination was done with a germanium detector. It detected the 1.809 MeV γ-rays originating from the deexcitation of ^{26}Mg to its ground state. This ^{26}Mg is formed from the β-decay of ^{26}Al. This resulted in a ^{26}Al sample containing $(2.58 \pm 0.12) \times 10^{17}$ ^{26}Al atoms. A detailed description of the preparation and characterization of the ^{26}Al target can be found in [Ing02].

3.7.3 ^{41}Ca sample

The ^{41}Ca sample was prepared at the IRMM by suspension spraying of CaF_2 in methanol on an aluminium foil. This resulted in a $^{41}CaF_2$ sample with 81.69 % enrichment [Wag89]. Subsequently, the mass determination was performed at the IRMM based on the detection of the 3.3 keV KX-rays emitted by ^{41}K after the decay of ^{41}Ca through electron capture (see [Wag89] and references therein). This resulted in a ^{41}Ca sample containing $(3.36 \pm 0.44) \times 10^{17}$ ^{41}Ca atoms.

Chapter 4

^{26}Al measurement

In this measurement the ^{26}Al(n,α)^{23}Na reaction was studied. Up to now the only neutron induced measurements on ^{26}Al above thermal energy are the ^{26}Al(n,p)^{26}Mg measurement by Trautvetter *et al.* [Tra86] and the ^{26}Al(n,p$_1$)^{26}Mg and ^{26}Al(n,α_0)^{23}Na measurements performed by Koehler *et al.* [Koe97]. Trautvetter *et al.* [Tra86] determined the partial cross section and corresponding reaction rate for four neutron energies. The measurements of Koehler *et al.* [Koe97] resulted in a cross section determination from thermal energy up to 70 keV for the (n,p$_1$) reaction and up to 10 keV for the (n,α_0) reaction. In the (n,α_0) reaction, only one resonance was observed by Koehler *et al.* [Koe97]. The aim of this work was to extend the energy range to observe more resonances, which are predicted through inverse reactions by Skelton *et al.* [Ske87]. Moreover, values are obtained for resonance parameters, such as resonance energy, total and partial level widths, area and spin of the state. These new data are important in the astrophysical network calculations as the ^{26}Al(n,α) reaction is one of the major destruction reactions of ^{26}Al in our Galaxy. The experimental calculated MACS values replace the theoretical values in the network calculations over the measured energy range.

4.1 Experimental setup

The ^{26}Al(n,α)^{23}Na reaction was studied at a 8.5 m flight path (FP13) with the LINAC being operated at 800 Hz and an electron pulse width of 1 ns. This allowed a (n,α) cross section determination from a few hundred eV up to approximately 45 keV. The total measuring time of the experiment was 2873

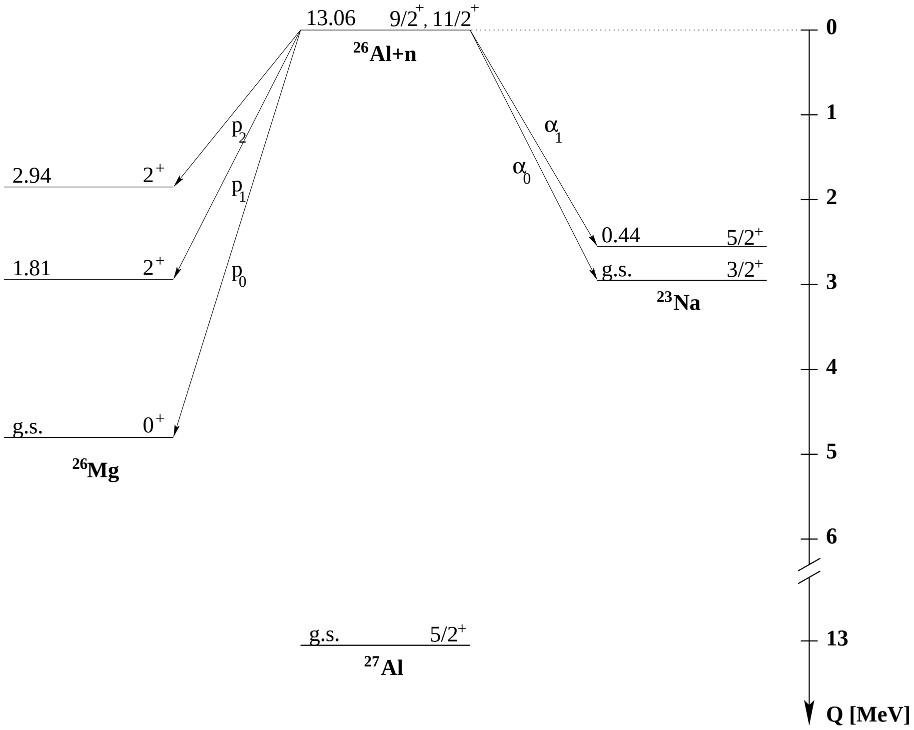

Figure 4.1: Level scheme for the ^{26}Al(n,α_i)^{23}Na and ^{26}Al(n,p$_i$)^{26}Mg reactions. The energies are given in MeV.

hours.

From the level scheme in figure 4.1 it is clear that both (n,p) and (n,α) reactions are possible. Table 4.1 gives the Q-values and corresponding energies of the protons and α-particles mentioned in figure 4.1. In order to study (n,α) reactions, the detector had to be tuned in such a way that only the α-particles were detected. To restrict as much as possible the detection of partially stopped protons with an energy in the neighbourhood of the α-energy, a small ionization chamber was chosen, with electrodes having a 16.2 cm diameter. The α_2-particles were not detected, because the probability that these α-particles penetrate the coulomb barrier is very low. Another requirement for the tuning is due to the presence of a ^{148}Gd impurity in the ^{26}Al sample, which emits α-particles of 3.2 MeV. These α-particles should be stopped completely

	Q-value [MeV]	E [MeV]
p_0	4.78	4.60
p_1	2.98	2.87
p_2	1.85	1.78
α_0	2.97	2.53
α_1	2.53	2.16
α_2	0.89	0.76

Table 4.1: Q-values and corresponding ejectile energies for the possible ^{26}Al(n,α_i)^{23}Na and ^{26}Al(n,p$_i$)^{26}Mg reactions.

in the detector. If this is not the case, partially stopped α-particles from Gd may contribute to the α_0- or α_1-signal from the ^{26}Al(n,α_i) reaction.

The requirements for a good functioning of the Frisch gridded ionization chamber are discussed in subsection 3.2.2. To fulfil all these conditions, the chamber was tuned as follows: V_A = 2000 V, V_C = -2500 V, V_G = 0 V, d_{cg} = 2.4 cm, d_{ag} = 0.6 cm and the methane gas pressure was 1 + 0.15 atm. The charged particles were detected in a 2π geometry in the upstream direction of the neutron beam.

In this configuration the 4.6 MeV protons lose less than 2 MeV in the region between cathode and anode. As a consequence neither the 4.6 MeV nor the 1.78 MeV protons will contribute to the α_i-signal. To be sure that the 2.87 MeV protons do not have any influence, a simulation of the detector was done. Figure 4.2 shows the distribution of the energy loss in the detector between anode and cathode of 10^7 particles emitted randomly. This simulation shows that also partially stopped 2.87 MeV protons do not contribute to the (n,α)-signal.

A last comment should be made on the entrance window of the ionization chamber. Normally this is made of aluminium. Because ^{27}Al has a resonance at 5.9 keV and because it was shown in previous experiments [Koe97, Wag00] that ^{26}Al(n,α_0) has a big resonance around this energy, the aluminium entrance window was replaced by a mylar one.

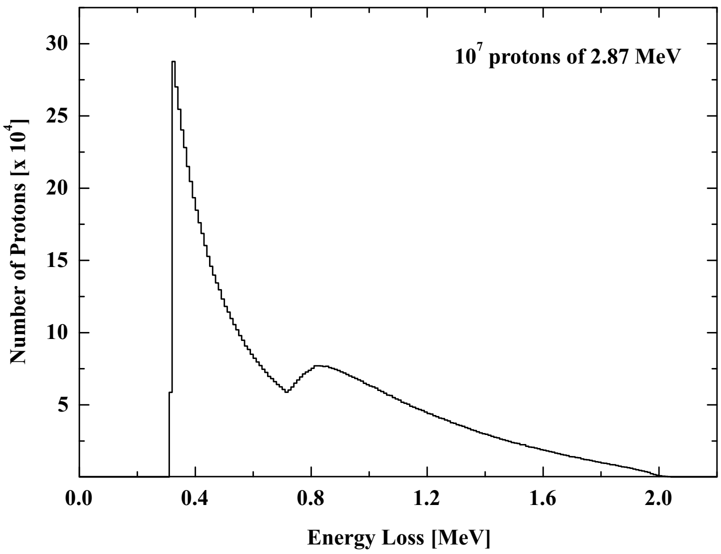

Figure 4.2: Distribution of the energy loss in the ionization chamber between cathode and anode of 10^7 protons with 2.87 MeV and emitted randomly.

4.2 Data analysis

4.2.1 ^{26}Al measurement

The anode versus cathode pulse height spectrum is shown in figure 4.3. The ^{26}Al(n,α_i)-particles are situated in the region in the middle. Because the decay α-particles of Gd have more energy, they can be found at the upper right side of figure 4.3. The counts in the region at the bottom left are attributed to (n,α_i)-particles induced in ^{10}B, which is also present with a non negligible amount in the ^{26}Al sample. The ^{26}Al(n,α_i) reactions can be selected by putting appropriate software windows on the anode and cathode pulse height spectra. In this way, several resonances can be identified in the corresponding TOF spectrum. However, if the anode (or cathode) pulse height spectrum is plotted versus the TOF spectrum for all the (n,α) reactions, a deformation of the electronic baseline can be observed at low TOF values, as is shown in figure 4.4. The main reason for this deformation is the influence of the γ-flash on the ionization chamber and electronics. It shifts the pulse height at low

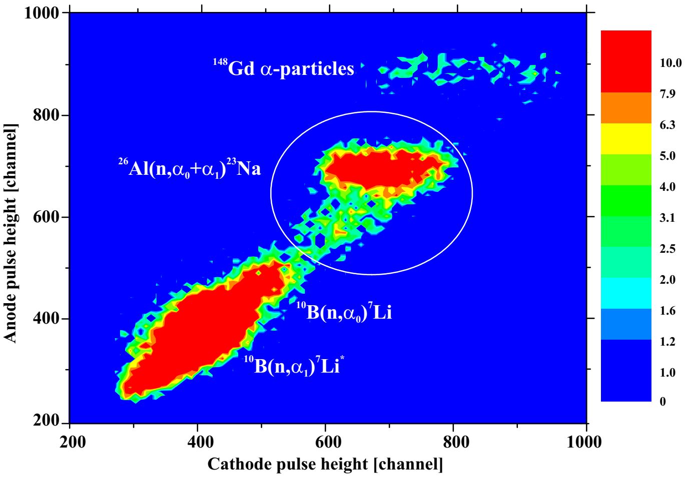

Figure 4.3: Anode versus cathode pulse height spectrum for the ^{26}Al(n,α_i) measurement. The α_i-particles resulting from the ^{26}Al(n,α_i) reaction are situated in the circled region in the middle.

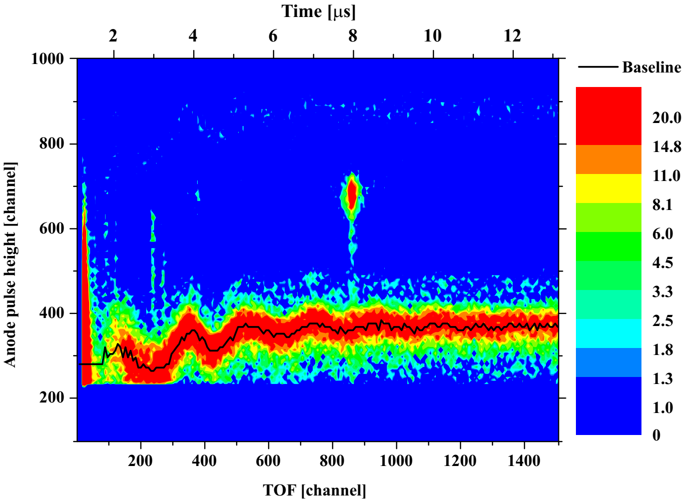

Figure 4.4: Anode versus TOF spectrum for the ^{26}Al(n,α_i) measurement. At low TOF a deformation of the electronic baseline, represented by the black line, can be observed. The α_i-particles from the ^{26}Al(n,α_i) reaction are situated at anode pulse heights between 450 and 750.

TOF values, making a clear particle selection difficult. One should correct for this deformation of the baseline before putting software windows on the pulse heights. This is performed by tracing the pulse height for the α_1-particles from the ^{10}B(n,α) reactions in the sample as a function of the TOF, represented by the black line in figure 4.4. By subtracting the values at low TOF from the value at high TOF where no deformation appears, a correction term for each TOF channel can be calculated. By adding this correction term to the pulse height, the baseline fluctuation is cancelled out. Figure 4.5 shows the anode pulse height versus TOF after correction for the baseline deformation. Several ^{26}Al(n,α_i) resonances can be observed and it shows that it is even possible to seperate the α_0-particles from the α_1-particles. A clear particle selection can now be made. To be sure to pick both α-particles, the selection windows on both ADC's has not been taken too narrow. This resulted in the presence of ^{10}B(n,α_0) particles in the selection window. To correct for these unwanted counts, a fit has been performed on the corresponding background corrected TOF spectrum. For this fit, it is assumed that in the lower energy region ($E_n < 2.2$ keV), where no resonances have been observed, the counts are only coming from the ^{10}B(n,α_0) reaction. A function according to equation 3.24 is chosen. The fitted spectrum is subtracted which results in the final α_i-counts coming from the ^{26}Al(n,α_i) reaction. The corresponding TOF spectrum is shown in figure 4.6.

Figures 4.4 and 4.5 demonstrate that at very low TOF values it is impossible to describe the pulse height and no correction can be carried out. One can assume a 'rule of thumb' which states that below 3 μs it is impossible to measure. This means that for this experiment at 8.5 m the cross section can be determined up to an energy around 45 keV. At higher energies or below 3 μs one can only conclude that there are resonances at specific energies, but a resonance analysis is out of the question. As mentioned in section 3.4 a longer flight path should be chosen to achieve higher energies. However, the neutron flux varies with $1/L^2$ and one should measure very long to obtain good statistics for the ^{26}Al(n,α_i) reaction. So, for this experiment figure 4.6 shows that four resonances remain for a resonance analysis. Whether the resonances are α_0- or α_1-transitions may be seen in figure 4.5. The first resonance, at highest TOF ($\sim$ channel 850), is mainly α_0, the second one (TOF $\sim$ channel 380) only α_0, the third one (TOF $\sim$ channel 280) only α_1 and finally the fourth resonance (TOF $\sim$ channel 250) is a mixture of α_0 and α_1.

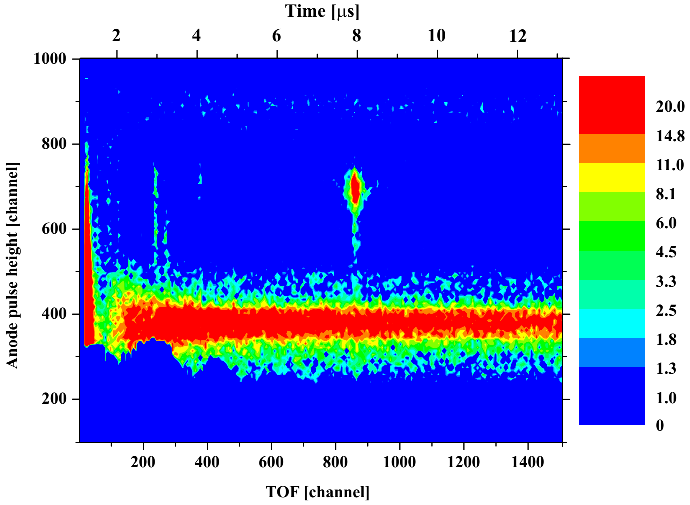

Figure 4.5: Anode versus TOF spectrum for the ^{26}Al(n,α_i) measurement after correction for the baseline distortion.

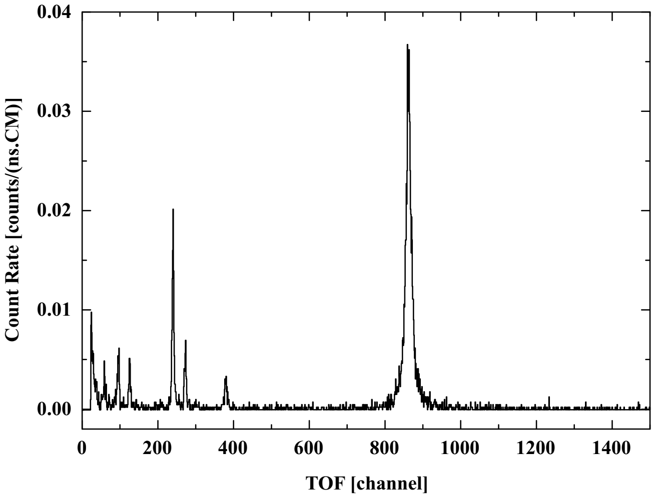

Figure 4.6: TOF spectrum after putting appropriate software windows on the anode and cathode pulse heights and after correction for the background and additional ^{10}B(n,α_0) counts. From TOF channel 100 to 1000, six resonances can be observed.

4.2.2 Flux determination

For the energy dependent flux determination a ^{10}B sample was used. Again a correction for the baseline fluctuation has been carried out before putting software windows to select the α_i-particles. However, figure 4.5 shows that for TOF channels 400, 250 and lower, some counts around anode channel 300 are missing. This is attributed to the lower level of the TSCA, which was put too high. To correct for these missing counts, a fit through the flux counts at higher TOF (lower energies) is made with the help of formula 3.24 and subsequently exptrapolated to the low TOF region.

4.2.3 Background determination

It is outlined in part 3.5 how the background is determined. In this case the five filters (Mn, Au, W, Rh and Co) are put together during one run to determine de background. A fit through the six black resonance points following equation 3.20 ($BG(t) = a + bt^c$) has been made. The result is shown in figure 4.7. Subsequently, this background fit is subtracted from the ^{10}B(n,α) count rate after which the efficiency of the detector has been taken into account.

In the ^{26}Al case however, the background counts were so low, that is was difficult to make a fit. For this reason a constant function has been fitted through the black resonance points.

4.2.4 Determination of the number of atoms in the samples used

As mentioned in section 3.7.2 the ^{26}Al sample contained $(2.58 \pm 0.12) \times 10^{17}$ ^{26}Al atoms. It was determined through the detection of the 1.8 MeV γ-rays from the deexcitation of ^{26}Mg to the ground state.

The number of ^{10}B atoms however was not yet determined accurately. As ^{10}B is a stable isotope, its amount was initially determined by weighing, which is not sufficiently accurate for very small quantities. For this reason an other experiment has been performed at 100 Hz, relative to a ^{235}U sample with a well defined thickness. ^{235}U has a well known neutron induced fission cross section at low energies. This is the reason to perform the measurement at 100 Hz. N_B in formula 3.25 is now the only unknown factor and can thus be determined.

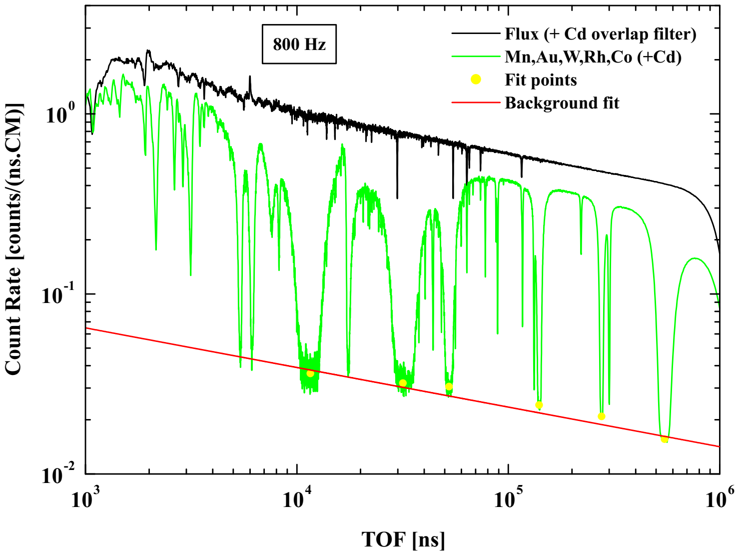

Figure 4.7: Background fit through the black resonance regions, represented by yellow dots, for the flux measurement.

For measurements at 100 Hz, no overlap filter is used. Nevertheless, there is still a non negligible contribution of slow neutrons, which will overlap in the TOF spectrum with the fast neutrons from the next bursts. This can be verified in figure 4.8 where the normalized neutron count rate is plotted for one cycle period of a 100 Hz run (ending at TOF = 10^7 ns) and compared with one of a 40 Hz run with the same ^{10}B sample. The difference between the two lines are the so called overlap neutrons, which don't appear in the 40 Hz run. To take into account these overlap neutrons, an iterative process is used. The overlap neutrons can be represented by an extrapolation of the low energy part of the spectrum obtained at 100 Hz, which is represented by the green line in figure 4.8 and has the following form:

$$y = a_1 t^{a_2}, \tag{4.1}$$

with a_1 and a_2 adjustable parameters. The contribution of these overlap neutrons in de next bursts can be written as:

$$y = a_1 (t + N\,\Delta T)^{a_2}, \tag{4.2}$$

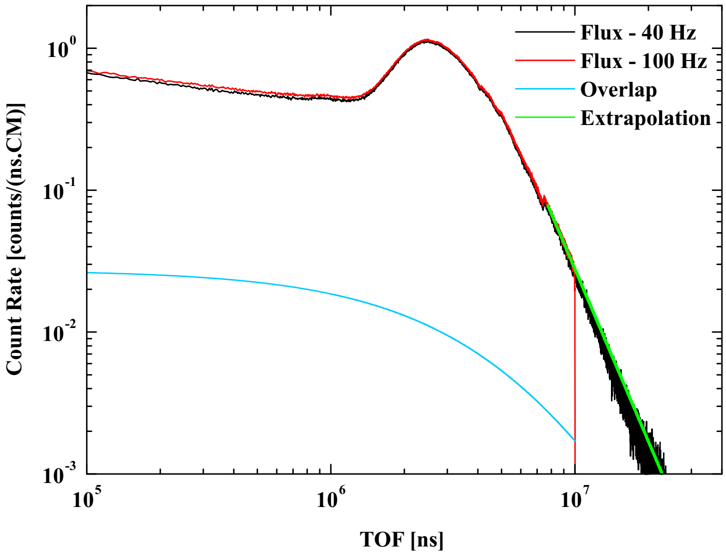

Figure 4.8: Comparison of the ^{10}B(n,α) count rate at 100 Hz (black line) with the count rate at 40 Hz (red line) for the same ^{10}B sample. The difference between these lines are the overlap neutrons appearing during the 100 Hz run (blue line). The contribution of the overlap neutrons at 100 Hz is represented by an extrapolation of the low energy part of the spectrum obtained at 100 Hz (green line).

where N represents the number of bursts following the first one and ΔT the time span between two bursts, which is 10 ms at 100 Hz repetition frequency. The contribution for each N is subtracted from the measured count rate. However, this leads to an overestimation of the overlap contribution. Therefore, the same process needs to be performed on the corrected count rate. This iteration can be repeated several times. However, after the second iteration, the result does not change significantly.

For the determination of the background other than due to overlap neutrons, two seperate runs have been performed: one with a Cd filter for the low energy region and a second run with the Au, Rh, Co, W and Mn filters together to cover the higher energy region. In these two runs, the background filters take all the overlap neutrons out of the beam (see figure 4.9). To determine the energy dependent background it is sufficient to make a fit through the

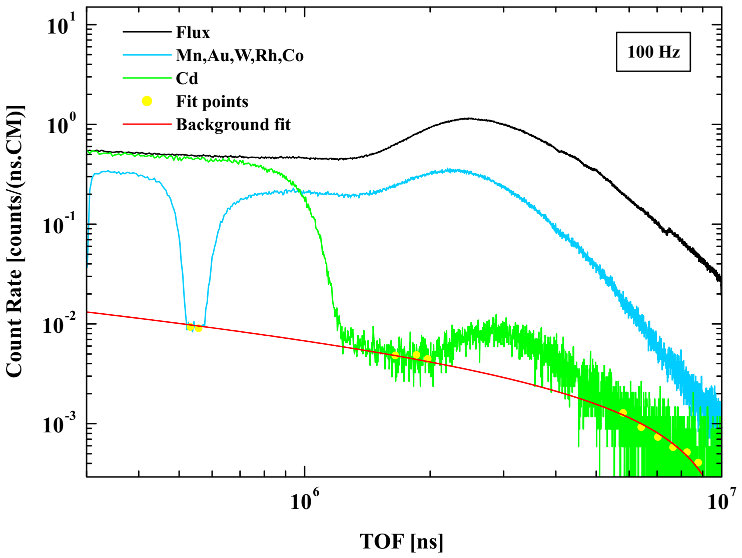

Figure 4.9: Background contribution for the flux measurement at 100 Hz. To determine the low energy background contribution a Cd filter is used, represented by the green line. A second run was performed with Mn, Au, W, Rh and Co as black resonance filters (blue line) to determine the background at higher neutron energies. However, in this figure, only the black resonance due to the rhodium filter is shown as the number of ^{10}B atoms in the sample is determined in the TOF region shown here.

black resonance zones of the measured background count rate. Subsequently this fit can be subtracted from the overlap-corrected count rate ($Y^C_{B/U}$). With the help of formula 3.25, N_B can now be written as follows:

$$N_B = \frac{Y^C_B - BG_B}{Y^C_U - BG_U} N_U \frac{\sigma_U}{\sigma_B}. \tag{4.3}$$

A fit between 0.015 eV and 0.7 eV of the obtained spectrum 4.3 gives the value of $N_B = (6.30 \pm 0.08)$ μg/cm^2 ^{10}B, which corresponds to $(1.14 \pm 0.014) \times 10^{20}$ ^{10}B atoms. The fit is depicted in figure 4.10.

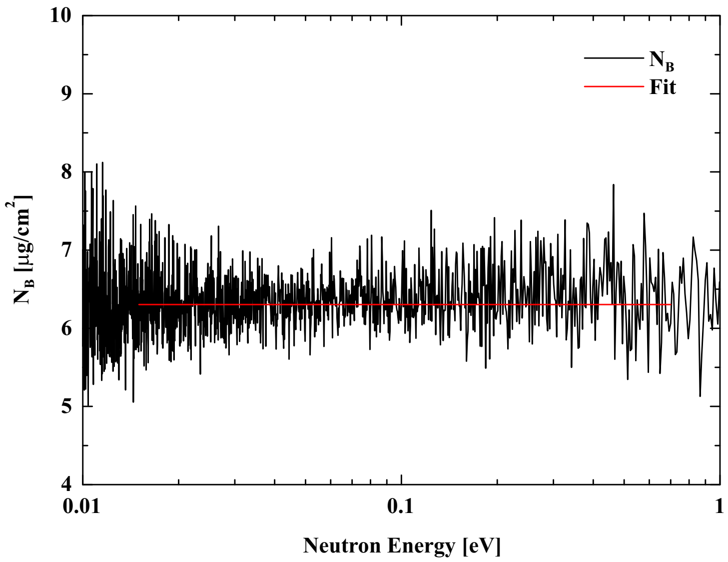

Figure 4.10: Determination of the number of ^{10}B atoms.

4.3 Calculation of the cross section

After combining the count rates following equation 3.25, one just has to convert the TOF channels into energy channels with the help of formula 3.11. As mentioned in subsection 3.4.2 a delay time has to be taken into account. To determine this delay, the second method mentioned in subsection 3.4.2 was used. With the help of the narrow resonances from the Cd overlap filter and the background filters in the flux determination, the delay Δ as well as the exact flight path length were determined.

The obtained ^{26}Al(n,α)^{23}Na cross section is depicted in figure 4.11. It shows that in this work six resonances can be observed, at 5.9 keV, at 22 keV, at 35 keV, at 41 keV, at 84 keV and at 108 keV. As mentioned before, at energies higher than approximately 45 keV, one can only conclude that there must be a resonance at that energy position, but the resonances may not be considered in a resonance analysis. The uncertainty on the cross section values is determined by the statistical uncertainty on the count rates, the uncertainties on the number of atoms in the ^{26}Al and ^{10}B samples and the uncertainty on the ^{10}B(n,α) reference cross section taken from the ENDF/B-VI data base. The

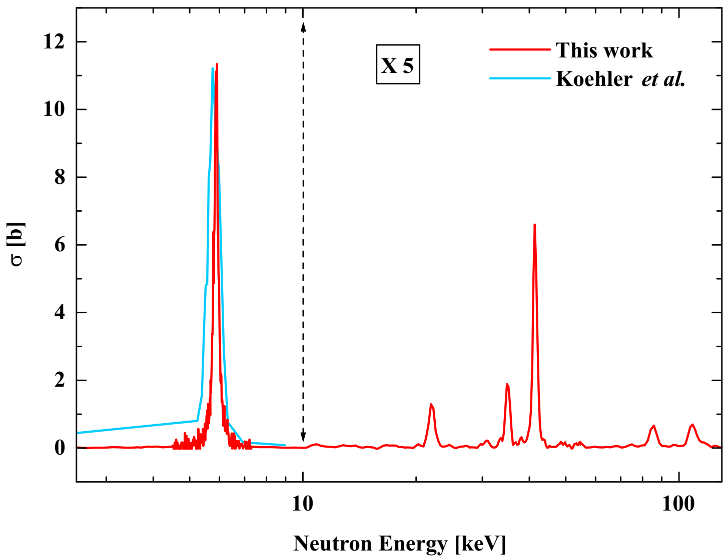

Figure 4.11: ^{26}Al(n,α_0+α_1)^{23}Na cross section determined in this work (red line) compared with the ^{26}Al(n,α_0)^{23}Na cross section obtained by Koehler *et al.* [Koe97] (blue line).

obtained cross section is compared with an experiment performed by Koehler *et al.* at the Los Alamos Neutron Science Center (LANSCE) [Koe97]. They measured the ^{26}Al(n,p_1)^{26}Mg and ^{26}Al(n,α_0)^{23}Na cross sections from thermal energy up to respectively 70 keV and 10 keV. It is clear that the resonance around 6 keV observed by Koehler during the ^{26}Al(n,α_0)^{23}Na cross section measurement has a much bigger area than the one observed in this work.

4.4 Resonance analysis

In subsection 1.1.5 a brief outline is presented how to extract the resonance characteristics from the compound nucleus. As explained before, the resonance analysis is restricted to 45 keV and four resonances remain to investigate.

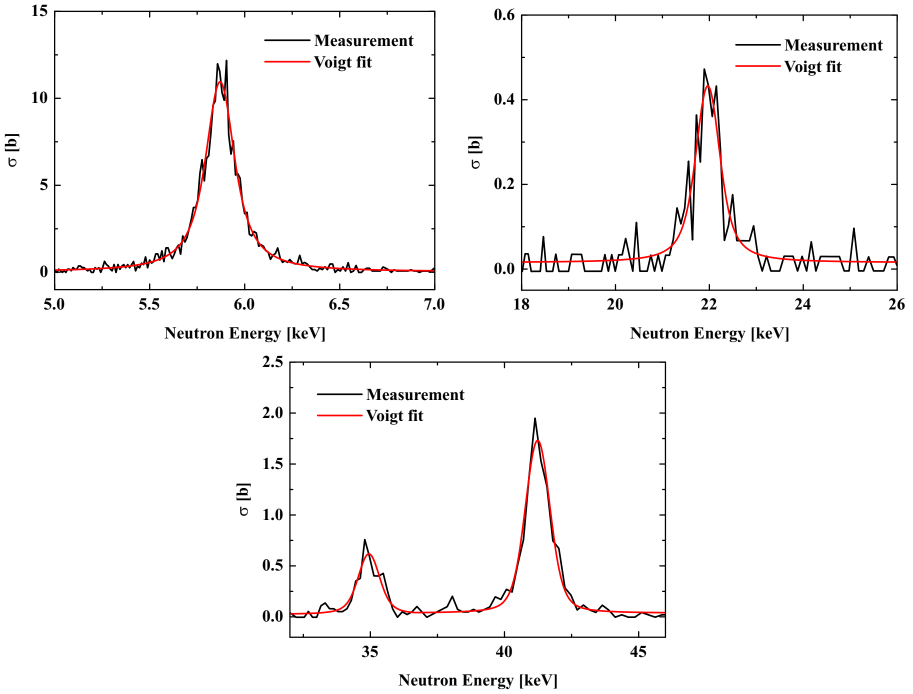

Figure 4.12: Voigt fits to the ^{26}Al(n,α_0+α_1)^{23}Na cross section data for the four resonances.

4.4.1 Fitting procedure

In a first step, each of the four resonances has to be fitted with Breit-Wigner shapes. This gives the resonance position E$_{res}$, the total level width Γ and the resonance strength ω_α which is proportional to the resonance area. However, in section 3.6 it is shown that the measured width of a resonance is broadened. Therefore, the fitted level width Γ does not correspond with the natural width of that level in the compound nucleus. It is explained in section 3.6 which broadening effects have to be taken into account and how to handle them properly. In this way the broadening can be calculated. Because a Breit-Wigner fit does not take into account this experimental broadening, the data in this work are fitted with a Voigt expression. Such a Voigt function is a convolution of a Gauss and a Lorenz function. Since a Lorenz expression is represented by a Breit-Wigner function in the case of compound nucleus re-

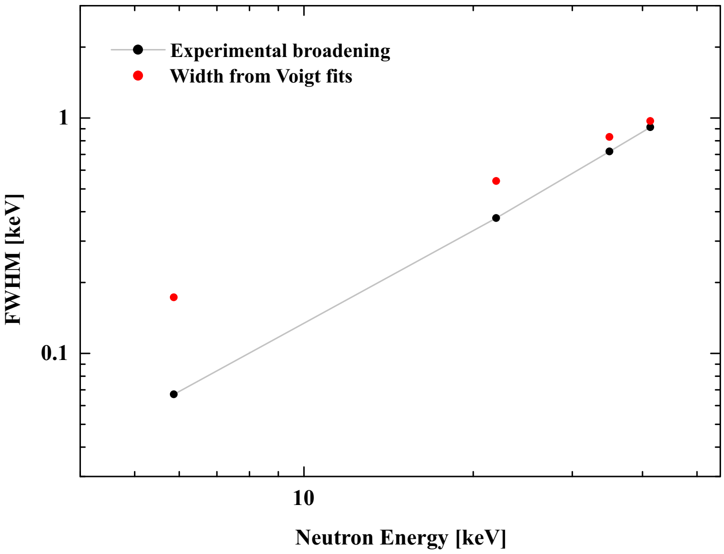

Figure 4.13: The total fitted width represented by red points compared with the calculated experimental broadening for the four observed resonances.

actions and since the experimental broadening can be regarded as a Gaussian contribution, a Voigt function is the ideal expression to fit the data. The fit parameters of a Voigt function are the resonance energy E_{res}, the area of the resonance A_{res}, the Gaussian width Δ_G and the width from the Breit-Wigner contribution Γ_{BW}. The Gaussian width Δ_G or broadening contribution can be calculated and was taken fixed during the fit. The resulting Voigt fits are shown in figure 4.12.

The experimental broadening Δ_G and the total fitted width $\Gamma_V = \sqrt{\Delta_G^2 + \Gamma_{BW}^2}$ are plotted in figure 4.13 at the energy position of each resonance. Only when the total width Γ_V is significantly bigger than the broadening width Δ_G, the fitted natural line width Γ_{BW} can be regarded as the real natural line width of that resonance. Figure 4.13 makes clear that only for the first two resonances and perhaps also the third resonance, the natural line width can be determined. The uncertainties on the natural line width are taken from the fit. If these were too small, a more realistic uncertainty was estimated.

The parameters obtained from the Voigt fits for each resonance are listed in table 4.2. The resonance strength ω_α can be calculated from the resonance area using formula 1.19. They can be compared with the strengths obtained by Skelton *et al.* [Kav] in table 4.3 and obtained by Koehler *et al.* [Koe97] in table 4.4. For two resonances Koehler *et al.* could fit the natural line width, which is listed in table 4.4. Since Koehler *et al.* measured the ^{26}Al(n,α_0) cross section only up to 10 keV, the parameters of the 35.00 keV resonance are deduced from their ^{26}Al(n,p) measurement. The results of Skelton *et al.* are obtained from the inverse reactions ^{26}Mg(p,n)^{26}Al and ^{23}Na(α,n)^{26}Mg [Ske87] via the method of detailed balance [Fow67].

It can be concluded that the uncertainties on the energy position obtained in this work are much better than in the previous data, showing the better energy resolution of the GELINA facility. Secondly, the resonance strengths for the resonances at 5.9 keV and 22 keV as well as the natural line width for the 5.9 keV resonance are in good agreement with the previous measurements. Finally, the resonance parameters for the 35 keV and 41 keV resonances show a notable disagreement, but the disagreement is smaller than 3σ.

4.4.2 Spin assignment

Various possibilities

s-wave (ℓ=0) neutrons impinging on the I$^\pi$ = 5$^+$ ground state of ^{26}Al will populate the J$^\pi$ = $\frac{9}{2}^+$ and J$^\pi$ = $\frac{11}{2}^+$ states of the compound nucleus ^{27}Al, whereas p-wave (ℓ=1) neutrons can populate states from J$^\pi$ = $\frac{7}{2}^-$ through J$^\pi$ = $\frac{13}{2}^-$. The formed states decay to the ground (J$^\pi$ = $\frac{3}{2}^+$) or first excited state (J$^\pi$ = $\frac{5}{2}^+$) of ^{23}Na by emitting α_0- or α_1-particles, respectively. The smallest allowed angular momenta of the emitted α-particles are tabulated in table 4.5.

resonance at 5.87 keV

Formula 1.24 can be used to calculate the thermal contribution of the three resonances of table 4.2 for which the natural line width could be determined. If the calculated value is higher than the thermal cross section, the resonance

Energy [eV]	Area [b.eV]	Γ [eV]	ω_α [eV]
5870 ± 20	2950 ± 250	160 ± 25	4.23 ± 0.36
21980 ± 100	340 ± 50	400 ± 100	1.83 ± 0.27
34950 ± 200	700 ± 100	400 ± 200	5.98 ± 0.86
41300 ± 200	2000 ± 200		20.19 ± 2.02
85200 ± 800			
108500 ± 1100			

Table 4.2: Resonance parameters obtained from the Voigt fits. Note that Γ here denotes the natural line width, which is Γ_{BW} in the text.

Energy [keV]	ω_α [eV]
5.80 ± 2.0	≤ 6.4
22.4 ± 2.0	≤ 2.5
42.0 ± 2.0	14.0 ± 1.4

Table 4.3: Resonance parameters obtained by Skelton *et al.* [Ske87, Kav] from the inverse ^{23}Na(α,n)^{26}Mg reaction.

Energy [keV]	ω_α [eV]	Γ [eV]
5.793 ± 0.040	6.6 ± 1.7	240 ± 200
35.00 ± 0.50		8200 ± 3000

Table 4.4: Resonance parameters obtained by Koehler *et al.* [Koe97]. The uncertainties on the energy position are estimated through the ^{36}Cl(n,p) measurement of Koehler *et al.* [Koe93].

J^π ^{23}Na	J^π ^{27}Al					
	s-wave		p-wave			
	$\frac{9}{2}^+$	$\frac{11}{2}^+$	$\frac{7}{2}^-$	$\frac{9}{2}^-$	$\frac{11}{2}^-$	$\frac{13}{2}^-$
$\frac{3}{2}^+$	4	4	3	3	5	5
$\frac{5}{2}^+$	2	4	1	3	3	5

Table 4.5: Smallest allowed angular momenta of the emitted α-particles from the formed compound nucleus ^{27}Al in the case of impinging s- or p-wave neutrons.

can in principle not be s-wave as only the tails of s-wave resonances contribute to the thermal cross section (see section 1.1.4). With the help of formula 1.24 a thermal contribution of 1045 mb was calculated for the first resonance at 5.87 keV. This resonance is mainly a transition to the ground state of ^{23}Na. This calculated thermal contribution is much higher than the experimentally determined thermal cross section of 261 mb [Wag01]. Therefore, this resonance is classified as a p-wave resonance, with spin J^{π} from $\frac{7}{2}^{-}$ through $\frac{13}{2}^{-}$. A standard optical model routine (CERBERO) [cer81] was used to calculate the averaged resonance areas for each spin assignment [Wei]. By comparing them with the obtained resonance area, a spin assignment of $\frac{9}{2}^{-}$ or $\frac{13}{2}^{-}$ could be chosen, where most probably the $\frac{13}{2}^{-}$ state can be ruled out. However, one should be very careful with this last conclusion because the properties of one specific resonance are compared with an averaged value, which is based on theoretical level densities over a wide energy interval.

Therefore, one can conclude that the first resonance is a p-wave resonance, with spin $J^{\pi} = \frac{7}{2}^{-}$ - $\frac{13}{2}^{-}$ and for which the $\frac{9}{2}^{-}$ state may be more likely than the other states.

resonance at 22 keV

The second resonance at 22 keV is a α_0-transition and has a calculated thermal contribution of 41 mb, which is lower than the measured (n_{th},α_0) value of 261 mb. So, this resonance can be classified as a s-wave resonance with spin $J^{\pi} = \frac{9}{2}^{+}$ or $\frac{11}{2}^{+}$. Comparison with the optical model calculation tends to take the $\frac{11}{2}^{+}$ state, but again this has to be handled with caution.

resonance at 35 keV

The third resonance at 35 keV gives a thermal cross section contribution of 44 mb and is a α_1-transition. The experimentally determined thermal α_1 cross section is 74 mb [Wag01], so this resonance is s-wave and the spin of the state is $\frac{9}{2}^{+}$ or $\frac{11}{2}^{+}$. Again prudence is called for when comparing the measured data with the optical model calculations which lead to a spin of $\frac{9}{2}^{+}$ in the case of a s-wave resonance.

	J^π		
Energy [keV]	This work	Koehler *et al.* [Koe97]	Doukellis [Dou89]
5.87	$[\frac{7}{2}^- - \frac{13}{2}^-]$	$[\frac{7}{2}^- - \frac{13}{2}^-]$	$\frac{11}{2}^+$
21.98	$[\frac{9}{2}^+ - \frac{11}{2}^+]$		$\frac{11}{2}^+$
34.95	$[\frac{9}{2}^+ - \frac{11}{2}^+]$	$[\frac{7}{2}^- - \frac{13}{2}^-]$	$\frac{9}{2}^+$

Table 4.6: Spin assignments obtained in this work compared with the spin assignments derived by Koehler *et al.* [Koe97] and by Doukellis [Dou89].

conclusions

In table 4.6 the spin assignments of this work are compared with the ones obtained by Koehler *et al.* [Koe97] and by Doukellis [Dou89]. The difference in spin assignment for the third resonance around 35 keV between Koehler and this work can be explained through the big difference in natural line width. Taking the value of Koehler *et al.* [Koe97] to calculate the thermal contribution in the case of a s-wave resonance leads to a thermal contribution which exceeds tremendously the measured value of 74 mb.

In principle, interference effects can reduce the contribution to the thermal cross section, leaving open the possibility of a different spin assignment for some resonances. However, this would lead to a non 1/v-behaviour of the cross section at low energies which is not the case, as measured by Koehler *et al.* [Koe97].

4.4.3 Determination of the partial level widths

For the determination of the partial level widths, only two equations are available:

$$\Gamma = \Gamma_\gamma + \Gamma_n + \Gamma_p + \Gamma_\alpha, \tag{4.4}$$

and

$$A_{res} = 2\left(\frac{\pi}{k_{res}}\right)^2 g\,\frac{\Gamma_n\,\Gamma_\alpha}{\Gamma}. \tag{4.5}$$

Even if it is assumed that the spin assignments made before are correct so that g is known and that the often used value for $\Gamma_\gamma = 1$ eV in this mass region is supposed [Mug81], even so three parameters are left to be fixed: Γ_n, Γ_p and Γ_α. With only two equations, it is not possible to solve this system

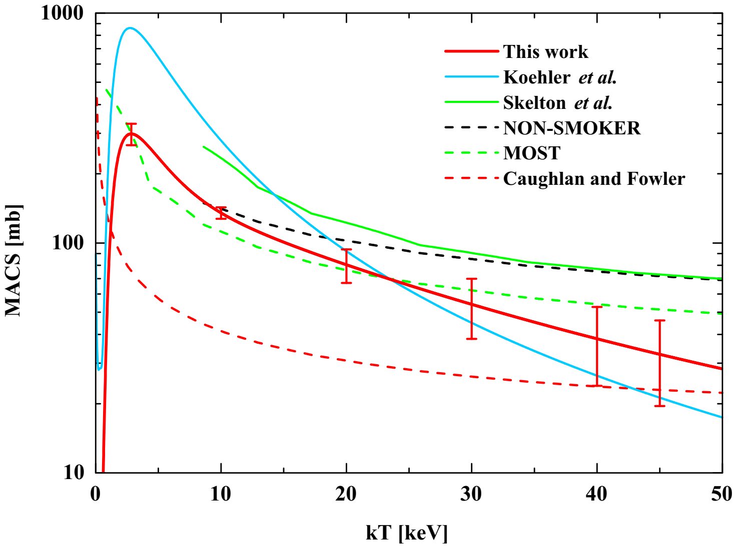

Figure 4.14: The ^{26}Al(n,α_0+α_1)^{23}Na MACS values calculated by numerical integration of the obtained cross section data (red line). A comparison is made with other experimental values from Koehler *et al.* [Koe97] and Skelton *et al.* [Ske87] and with theoretical values. The latter ones are represented by dotted lines.

of equations unambiguously. For this reason no partial level widths could be determined. Additional measurements are necessary, for instance ^{26}Al(n,γ), ^{26}Al(n,p) or total cross section measurements leading to the same compound nucleus. They will provide more equations so that the partial level widths can be determined. Then they may be used as input parameters in RSA programs to well define the spin and total and partial level widths of the states in the compound nucleus.

4.5 Astrophysical implications

4.5.1 Determination of the MACS

Numerical integration of the obtained cross section data using equation 1.29 leads to the ^{26}Al(n,α) MACS values. They are compared in figure 4.14 with the experimental values of Koehler *et al.* [Koe97] and Skelton *et al.* [Ske87]

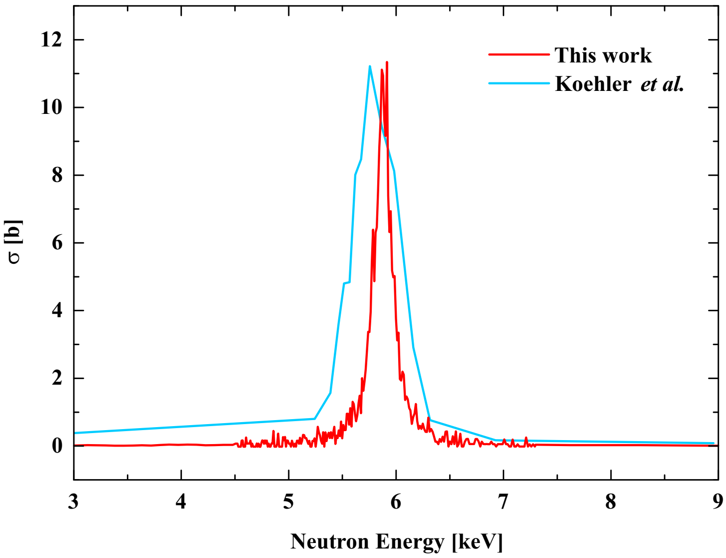

Figure 4.15: The obtained cross section data for the first resonance at 5.9 keV (red line) compared with the data of Koehler *et al.* [Koe97] (blue line). It shows that the resonance area obtained by Koehler is much higher than the area obtained in this work.

and with the theoretical calculations MOST [Gor], NON-SMOKER [Rau] and older theoretical values of Caughlan and Fowler [Cau88]. In this work, the (n,α) cross section determination ranged up to E$_f$ $\cong$ 45 keV. As a resonance at E$_{res}$ has its maximum contribution to the MACS values at kT = E$_{res}$/2 (see section 1.2), the obtained MACS values have to be considered as lower limits for kT above E$_f$ $\cong$ 22 keV. The obtained MACS values in this energy region (kT $\leq$ 22 keV) do not agree with the values obtained by Koehler *et al.* [Koe97]. However they are in reasonable agreement with the newest theoretical values. It is easily explained why the MACS values of Koehler *et al.* [Koe97] around 3 keV are much higher than the ones obtained in this work: the resonance area or strength for the resonance at 5.87 keV in the experiment of Koehler *et al.* [Koe97] is much higher, as shown in figure 4.15 and listed in tables 4.2 and 4.4. Because Koehler *et al.* [Koe97] measured only up to approximately 10 keV, their MACS values are lower limits for kT above 5 keV.

4.5.2 Destruction of ^{26}Al

The obtained MACS values do not differ significantly from the ones currently used in stellar models by the group of Gallino [Gal05], which are based on preliminary measurements performed at IRMM [Wag00]. The present results confirm and improve the accuracy of these preliminary data. Gallino *et al.* [Gal05] conclude that ^{26}Al is indeed severely depleted by neutron captures in AGB stars. In their models, the major destruction channel is the ^{26}Al(n,p) reaction which is 3.74 times more important than the ^{26}Al(n,α) reaction. However, when comparing the (n,p) MACS value at 31 keV obtained by Trautvetter *et al.* [Tra86] (137 mb) with the (n,α) MACS value obtained in this work (52 mb), a factor of 2.63 is calculated. Taking into account that the (n,α) MACS value from this work is a lower limit (see subsection 4.5.1), the factor of 2.63 is an upper limit. The question arises whether the (n,p) MACS values used at present are reliable. This shows that a new experimental determination of the ^{26}Al(n,p)^{26}Mg cross section over an energy interval as large as possible is necessary.

Chapter 5

^{36}Cl measurement

In this measurement the ^{36}Cl(n,p)^{36}S and ^{36}Cl(n,α)^{33}P reactions are studied. So far, two measurements of the energy dependence of the ^{36}Cl(n,p)^{36}S cross section were performed. Gledenov *et al.* [Gle85] observed three resonances up to 10 keV. Koehler *et al.* [Koe93] identified eight resonances in the energy region between 900 eV and 70 keV. However, both measurements suffered from a poor energy resolution. Therefore, a new measurement of the energy dependence at the GELINA facility was of interest. The purpose of this work was to extend the energy range in order to observe more resonances and at the same time to improve the experimental MACS values used in stellar model calculations to trace the origin of ^{36}S.

5.1 Experimental setup

The neutron induced charged particle reactions on ^{36}Cl were measured at a 30 m flight path (FP12), with a linac frequency of 800 Hz and an electron pulse width of 1 ns. The (n,p) and (n,α) cross section could be determined up to approximately 250 keV.

The level scheme from figure 5.1 shows that both (n,p) and (n,α) reactions are possible. The Q-values and corresponding particle energies are listed in table 5.1. From this table it is clear that a good separation of protons and α-particles will be difficult, because they have almost the same energy. In addition, the table shows that the α_1- and α_2-particles have low energies, so their probability to penetrate the Coulomb barrier is very small. These transitions were not observed in this experiment. This was neither the case

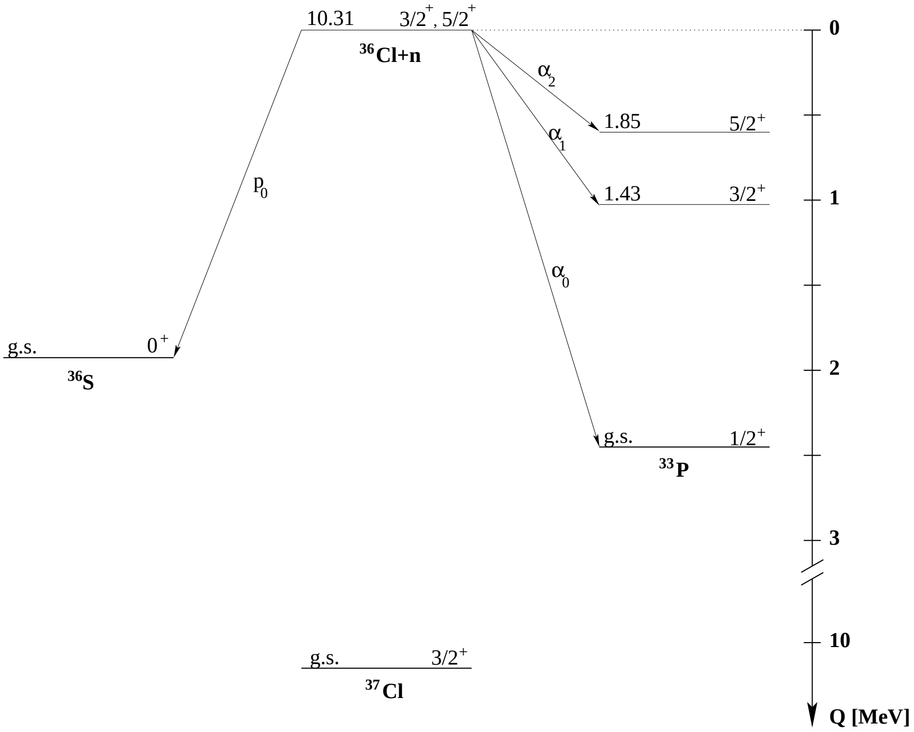

Figure 5.1: Level scheme for the ^{36}Cl(n,p)^{36}S and ^{36}Cl(n,α_i)^{33}P reactions.

in the thermal measurement performed by Wagemans *et al.* at the ILL in Grenoble [Wag96].

The detector is tuned in such a way that both protons and α-particles are detected. The Frisch gridded ionization chamber used had the following characteristics: V_A = 3600 V, V_C = -5000 V, V_G = 0 V, d_{cg} = 5.0 cm, d_{ag} = 1.0 cm and the methane gas pressure was 1 + 1 atm. Again the charged particles were detected in a 2π upstream direction.

	Q-value [MeV]	E [MeV]
p_0	1.924	1.872
α_0	2.462	2.196
α_1	1.030	0.919
α_2	0.614	0.548

Table 5.1: Q-values and corresponding energies for the possible ^{36}Cl(n,p)^{36}S and ^{36}Cl(n,α_i)^{33}P reactions.

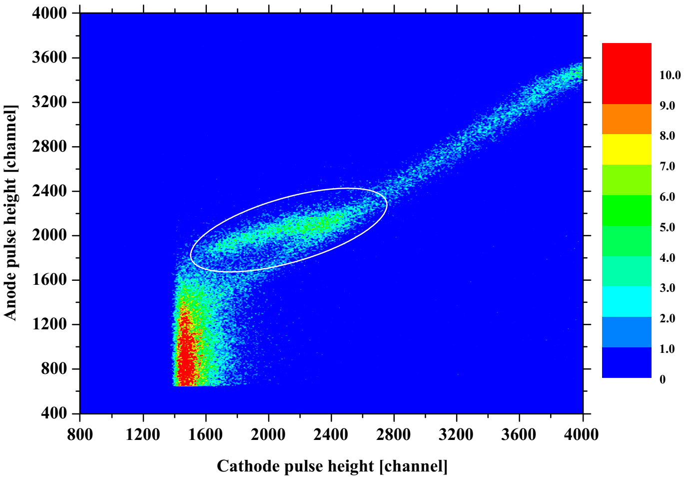

Figure 5.2: Anode versus cathode pulse height spectrum for the ^{36}Cl(n,p)^{36}S and ^{36}Cl(n,α)^{33}P reactions. The protons and α-particles from the neutron induced reactions on ^{36}Cl are situated in the circled region.

5.2 Data analysis

5.2.1 ^{36}Cl measurement

The marked region in the anode versus cathode pulse height spectrum in figure 5.2 indicates the detected protons and α-particles. They can be selected by putting appropriate software windows on the anode and cathode pulse heigths. In the corresponding TOF spectrum, several resonances appear (see figure 5.3).

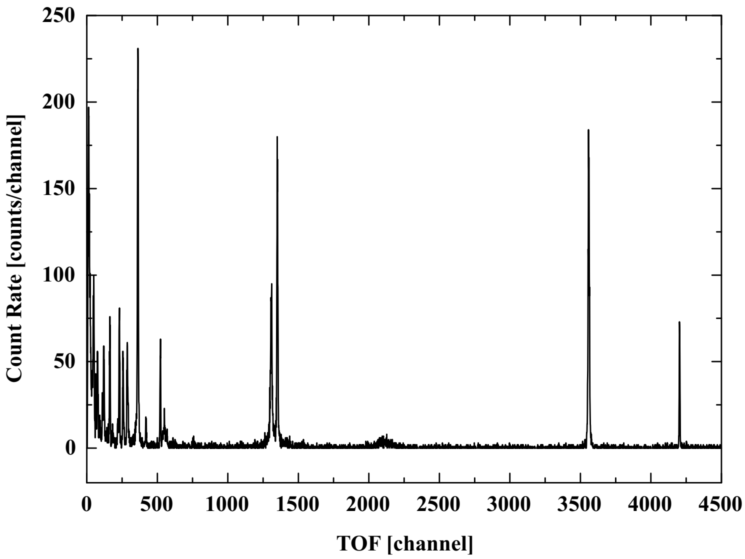

Figure 5.3: TOF spectrum after putting appropriate software windows on the anode and cathode pulse heights. Several resonances can be observed.

Figure 5.4 depicts a cathode versus TOF spectrum. Contrary to the ^{26}Al measurement, a determination of the baseline is not possible with the ^{36}Cl sample, since it contains no ^{10}B. However, figure 5.4 shows that in this case it is not necessary to correct for the baseline fluctuation, because, by putting slightly bigger software windows to select all the charged particles, shifted in pulse height by the baseline fluctuation at low TOF, no other particles than the ones that have to be detected, will be selected.

Figure 5.2 illustrates that separating protons and α-particles is indeed not easy. However, in a previous experiment performed by Koehler *et al.* [Koe93] at the Neutron Scattering Center (LANSCE) in Los Alamos, only for the lowest energy resonance at 0.93 keV (TOF $\sim$ channel 4250) a significant α-contribution was found. This can be observed in figure 5.4. The anode versus cathode pulse height spectrum for the first two resonances is plotted left in figure 5.5 against the anode versus cathode spectrum of figure 5.2. The first resonance at 0.93 keV (TOF $\sim$ channel 4250) is represented by the red dots, while the yellow dots represent the second resonance at 1.34 keV (TOF $\sim$ channel 3500). As explained in section 3.2 (equations 3.5 and 3.6), the anode pulse

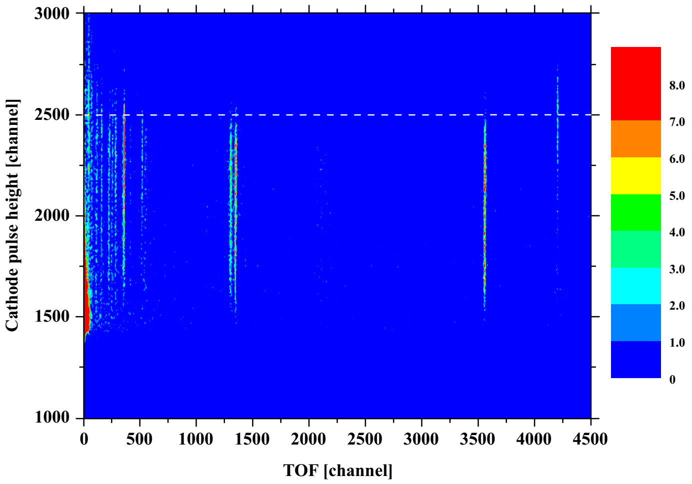

Figure 5.4: Cathode versus TOF spectrum after putting appropriate software windows on anode and cathode pulse heights. The dashed line illustrates that only the first resonance at highest TOF (∼ channel 4250) has a significant α-contribution, as the other resonances have no counts above this line.

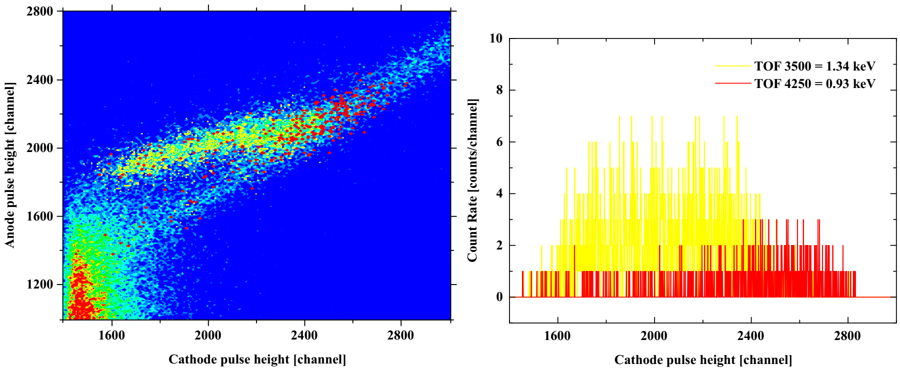

Figure 5.5: *Left:* Anode versus cathode pulse height spectrum for the first two resonances plotted against the anode versus cathode spectrum of figure 5.2. The red dots represent the counts from the first resonance at 0.93 keV (TOF ∼ channel 4250) and the yellow dots are the counts from the second resonance at 1.34 keV (TOF ∼ channel 3500).
Right: Cathode spectrum for the first two resonances. This plot shows that the first resonance at 0.93 keV indeed mainly consists of α-particles.

height gives only information on the total energy of the particles, while the cathode pulse height is proportional to X(E), the distance from the origin to the center of the ionization track. From figure 3.6 it can be deduced that the 1.87 MeV protons are completely stopped in the detector after travelling 35 mm, while the 2.19 MeV α-particles have a range of only 5.8 mm. This difference causes a 6 times larger X(E) for the protons than for the α-particles, which leads to a broader proton distribution in the cathode pulse height spectrum. The plot on the right of figure 5.5 compares the cathode spectra for the first two resonances. It shows that the first resonance at 0.93 keV has counts at higher channel numbers than the second resonance at 1.34 keV. In addition, the second resonance has a broader distribution. This makes clear that the first resonance indeed mainly consists of α-particles, while the second resonance mainly is a proton transition. Eventually, an α-contribution in the first resonance of (76 ± 7) % has been estimated. All the other resonances do not show this enhancement at higher pulse heights, therefore they are regarded as proton resonances with a negligible α-contribution. This can be verified in figure 5.4, where only the first resonance at TOF $\sim$ channel 4250 has a significant amount of counts in the cathode pulse height spectrum above channel number 2500, which is represented by the dotted line. In the TOF region below channel number 500, some counts appear above the dotted line. This is mainly due to the kinetic energy of the inducing neutrons which has to be taken into account in this energy region. It leads to a slightly higher energy for the emitted particles than the energy listed in table 5.1, which results in counts appearing at a higher cathode channel number. A second reason why some counts appear above cathode channel number 2500 at low TOF channel numbers is the fluctuation of the electronic baseline as has been observed in the ^{10}B(n,α) flux measurement.

The α-contribution of (76 ± 7) % for the first resonance is in agreement with the experiment performed by Koehler *et al.* [Koe93]. They found for this resonance that (n,α)/(n,p) = 3.0 and for the other resonances the (n,α)-contribution appeared to be very small.

5.2.2 Flux determination

Again a ^{10}B sample is used to determine the energy dependent neutron flux. Here a correction for the baseline fluctuation is performed before putting software windows for the α_i-selection. After subtracting the background contribution from the flux count rate, the efficiency of the detector has been taken into account as explained in subsection 3.5.3. After this correction and after conversion from TOF to energy, a fit through the resulting flux count rate has been performed with the help of the power function 3.24.

5.2.3 Background determination

In this experiment, only a Mn filter has been put in the neutron beam to determine the energy dependent background. A fit through the black resonance points has been performed with the help of formula 3.20. In the case of ^{36}Cl, the black resonance counts were so low, that a constant function through the black resonance zones is fitted.

5.2.4 Determination of the number of atoms in the samples used

The ^{36}Cl sample contained $(1.39 \pm 0.07) \times 10^{19}$ ^{36}Cl atoms, as mentioned in subsection 3.7.1.

A different ^{10}B sample from the one in the ^{26}Al measurement was used. In the same way as explained in subsection 4.2.4 an experiment at 100 Hz with a ^{235}U sample has been performed at a 8.3 m flight path (FP17). Again the overlap neutrons have been taken into account and a fit from 0.015 eV to 0.7 eV determined the value of $N_B = (3.97 \pm 0.07)$ μg/cm^2 ^{10}B. This corresponds to a ^{10}B sample containing $(7.17 \pm 0.13) \times 10^{19}$ atoms.

5.3 Calculation of the cross section

For the determination of the delay Δ, a seperate run is performed with a thin Al filter placed in the neutron beam. The aluminium resonances give rise to dips in the flux count rate spectrum. Aluminium has three energy standards, which are used to determine Δ as well as the exact flight path length. With these two values, the TOF can be converted into energy with the help of formula 3.11.

This gives the ^{36}Cl(n,p) + (n,α) cross section as a function of the neutron energy, which is shown in figure 5.6. The uncertainty on the values is a combination of statistical uncertainties on the count rates, uncertainties on the number of atoms in the samples used and the ^{10}B(n,α) reference cross section uncertainty, taken from the ENDF/B-VI nuclear data library. A comparison with the obtained cross section in the measurement of Koehler *et al.* [Koe93]

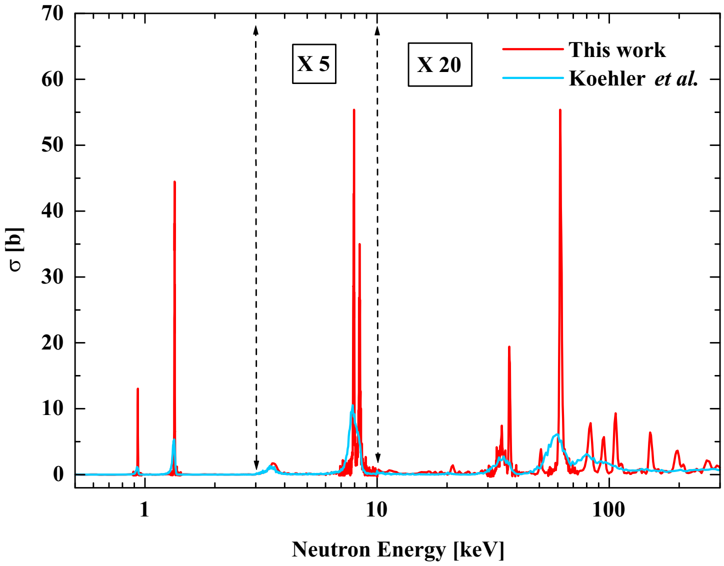

Figure 5.6: ^{36}Cl(n,p)^{36}S plus ^{36}Cl(n,α)^{33}P cross section determined in this work (red line) compared with the obtained cross section of Koehler *et al.* [Koe93].

is plotted in figure 5.6. Due to the better energy resolution of the GELINA facility, much more resonances could be observed in this work.

5.4 Resonance analysis

5.4.1 Fitting procedure

The resonances are fitted with Voigt functions to determine the energy position, the area and the total level width. It is explained in subsection 4.4.1 how the experimental broadening is taken into account. This broadening was calculated and held fixed during the fit. For some resonances the Voigt fits are shown in figure 5.7. The total width obtained from the Voigt fit is plotted with the experimental broadening for each resonance position in figure 5.8. From this plot it is clear that there are only a few resonances for which the total width is bigger than the experimental broadening. Only for these resonances the natural line width is calculated and listed in table 5.2 together with the two other fit parameters, the peak position E_{res} and the resonance area A_{res}.

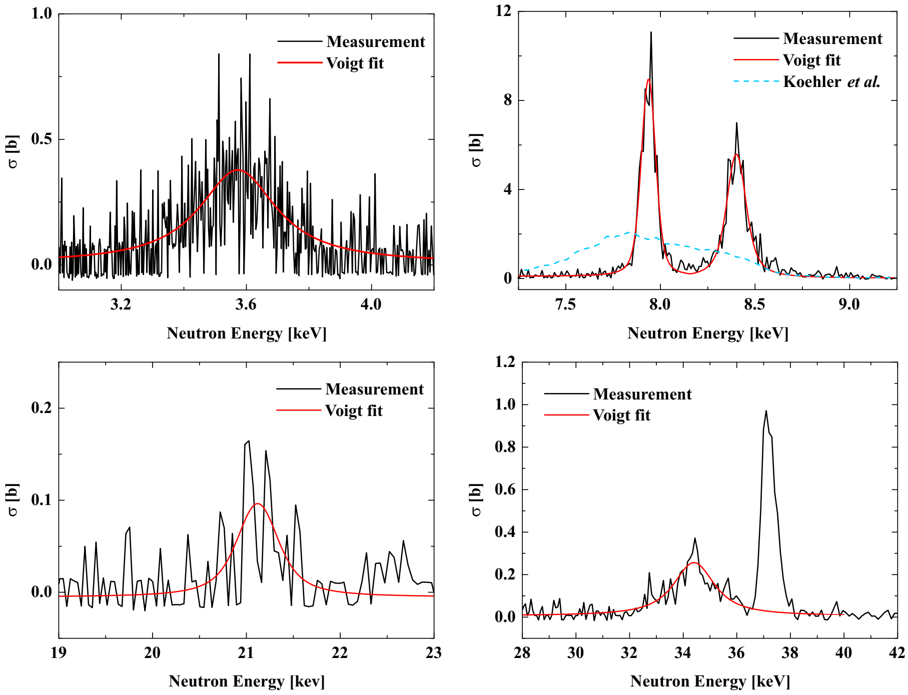

Figure 5.7: Voigt fits to the ^{36}Cl(n,p) + ^{36}Cl(n,α) cross section data for some resonances. For the doublet at about 8 keV, the data obtained in this work are compared with the data of Koehler *et al.* [Koe93], which is represented by the blue dashed line.

5.4.2 Spin assignment

s-wave neutrons hitting the $I^\pi = 2^+$ ground state of ^{36}Cl can populate $J^\pi = \frac{3}{2}^+$ or $\frac{5}{2}^+$ states. For p-wave neutrons, states from $J^\pi = \frac{1}{2}^-$ through $\frac{7}{2}^-$ can be excited. As shown in the level scheme in figure 5.1, proton decay to the ground state ($J^\pi = 0^+$) of ^{36}S is allowed, but proton decay to the excited states of ^{36}S is energetically forbidden in the neutron energy range of this work. On the other hand, α-decay to the ground state ($J^\pi = \frac{1}{2}^+$) and to the first two excited states ($J^\pi = \frac{3}{2}^+$ and $J^\pi = \frac{5}{2}^+$) of ^{33}P is allowed. However, decay to the excited states of ^{33}P is less favoured because of the smaller penetrability

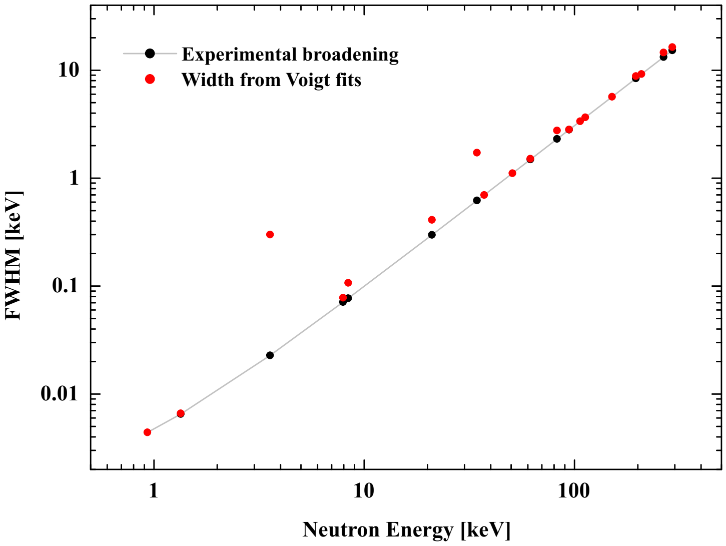

Figure 5.8: The total width obtained from the Voigt fits (red points) compared with the calculated experimental broadening for each observed resonance.

through the Coulomb barrier for the lower energetic α-particles. The smallest allowed angular momenta for the different decay possibilities are listed in table 5.3.

Whether the excited level is populated by a s-wave neutron or not can be determined by calculating its contribution to the thermal cross section with formula 1.24. For the four resonances for which the natural line width is listed in table 5.2, this contribution is calculated. Only the resonance around 21 keV stays far below the measured thermal cross section of 47 mb [Wag96], and is taken to be s-wave. The thermal contribution for the other three resonances is much higher than 47 mb, so they are expected to be p-wave.

5.4.3 Determination of the partial level widths

Apart from the measurement of Koehler *et al.* [Koe93], there are only two measurements reported from which information can be derived about the resonances. The first one is a ^{36}S(p,γ)^{37}Cl measurement by Nooren *et al.*

Energy [eV]	Area [b.eV]	Γ [eV]
931 ± 1	57 ± 8	
1341 ± 2	345 ± 30	
3570 ± 50	140 ± 50	300 ± 30
7937 ± 15	985 ± 80	
8400 ± 20	1000 ± 100	75 ± 25
21100 ± 300	50 ± 25	300 ± 250
34400 ± 200	500 ± 120	1600 ± 1000
37200 ± 100	625 ± 50	
50750 ± 200	255 ± 70	
61700 ± 200	4600 ± 400	
82700 ± 800	1500 ± 800	
94400 ± 800	1500 ± 600	
106500 ± 500	1600 ± 400	
112700 ± 1000	300 ± 200	
151000 ± 1500	1800 ± 600	
196000 ± 1500	2000 ± 1000	
208500 ± 3000	500 ± 300	
265500 ± 4000	3500 ± 2000	

Table 5.2: Resonance parameters obtained from the Voigt fits. The natural line width Γ is calculated only for these resonances for which the total fitted width is bigger than the experimental broadening.

Final state	J^π ^{37}Cl compound nucleus					
	s-wave		p-wave			
	$\frac{3}{2}^+$	$\frac{5}{2}^+$	$\frac{1}{2}^-$	$\frac{3}{2}^-$	$\frac{5}{2}^-$	$\frac{7}{2}^-$
^{36}S: 0^+ (p_0)	2	2	1	1	3	3
^{33}P: $\frac{1}{2}^+$ (α_0)	2	2	1	1	3	3
^{33}P: $\frac{3}{2}^+$ (α_1)	0	2	1	1	1	3
^{33}P: $\frac{5}{2}^+$ (α_2)	2	0	3	1	1	1

Table 5.3: Smallest allowed angular momenta of the emitted particles from the formed compound nucleus ^{37}Cl in the case of impinging s- or p-wave neutrons.

[Noo84]. They observed three resonances corresponding with a neutron energy between 0 and 8 keV in the laboratory system, for which the resonance strength $\omega_\gamma = (2J+1)\frac{\Gamma_\gamma \Gamma_p}{\Gamma}$ is reported. Comparison with the data obtained in this work indicates that they did not resolve the 0.93 keV and 1.34 keV doublet nor the 7.94 keV and 8.40 keV doublet. The second measurement is a ^{36}S(p,γ)^{37}Cl measurement by Vodin *et al.* [Vod96]. Their proton energy ranged up to approximately 1 MeV neutron energy and they reported the resonance strengths ω_γ for the resonances observed in their measurement. Once again they did not resolve the doublets around 1 keV and 8 keV. The resonance strengths listed by Vodin *et al.* [Vod96] for the three resonances observed by Nooren *et al.* [Noo84] are comparable. Therefore, it is assumed that the resonance strengths reported by Vodin *et al.* [Vod96] may be used for the determination of the partial level widths for the four resoncances of this work for which the natural line width could be calculated (see table 5.2).

For these four resonances, three equations are available:

$$\begin{aligned}
\Gamma &= \Gamma_n + \Gamma_\gamma + \Gamma_p \\
\omega_p &= g\frac{\Gamma_n \Gamma_p}{\Gamma} = \frac{2J+1}{10}\frac{\Gamma_n \Gamma_p}{\Gamma} \\
\omega_\gamma &= (2J+1)\frac{\Gamma_\gamma \Gamma_p}{\Gamma}.
\end{aligned}$$

Combining them leads to the following solutions for the unknown Γ_γ, Γ_n and Γ_p:

$$\begin{aligned}
\Gamma_\gamma &= \frac{\Gamma \pm \sqrt{\Gamma^2 - \frac{4\Gamma}{2J+1}\left(10\omega_p + \omega_\gamma\right)}}{2\left(10\frac{\omega_p}{\omega_\gamma} + 1\right)} \qquad (5.1) \\
\Gamma_n &= 10\frac{\omega_p}{\omega_\gamma}\Gamma_\gamma \\
\Gamma_p &= \frac{\omega_\gamma \Gamma}{(2J+1)\Gamma_\gamma}.
\end{aligned}$$

For the doublet around 8 keV, which was not resolved in the data of Vodin *et al.* [Vod96], the reported ω_γ is split up in two equal parts for each resonance. So, for each J-value, two sets of partial widths are possible. Based on the systematics for excited levels in this mass region, the positive sign of the square root in equation 5.1 may for most of the cases be ruled out because Γ_γ

will be too high. For the moment J is not determined unambiguously, therefore no partial level widths are listed. However, by trying all the possibilities for J and by taking the negative square root, it turned out that in every case Γ_p almost equals Γ. In addition, by increasing J, Γ_p approaches more and more Γ. This means that:

$$\omega_p = g\,\frac{\Gamma_n \Gamma_p}{\Gamma} \sim g\,\Gamma_n, \tag{5.2}$$

or the resonance strength or the area of the resonance determines completely Γ_n.

Once J is determined through additional measurements leading to the same ^{37}Cl compound nucleus, the partial widths can be deduced from the set of equations listed above. Then these deduced partial widths and accompanying spin may be used as input parameters in RSA programs to well define the total and partial level widths of the states in the compound nucleus.

5.4.4 Discussion

Firstly, by measuring the ^{36}Cl(n,p) + ^{36}Cl(n,α) reactions as a function of the neutron energy eighteen resonances are observed in the energy region up to approximately 250 keV, which is much more than the eight observed before by Koehler *et al.* [Koe93]. This is due to the better energy resolution at GELINA by which resonances could be resolved from each other. This is nicely shown in figure 5.6, e.g. the doublet around 8 keV and the higher energy region.

Secondly, in table 5.4 the spin assignments, level widths and resonance strengths for each of the four resonances obtained in this work are compared with the ones obtained in the work of Koehler *et al.* [Koe93] and Gledenov *et al.* [Gle85]. The table shows that the energy precision obtained in this work is better than before. Furthermore, the obtained resonance parameters are in excellent agreement with the data of Koehler *et al.* [Koe93] and Gledenov *et al.* [Gle85]. Only the spin assignment for the resonance at 8.4 keV is different from the one derived by Koehler *et al.* [Koe93]. However, their resonance strength and level width Γ are about two times smaller than those obtained in this work. Furthermore, the thermal contribution in the case of a s-wave resonance is proportional to both parameters (see formula 1.24), and by taking the parameters listed by Koehler *et al.* [Koe93] the contribution stays below the thermal value, indeed leading to a s-wave. Nevertheless, in the cross section data of Koehler *et al.* [Koe93] it was difficult to resolve the doublet around 8 keV. Therefore it can be possible that the distribution of the areas and the

	Energy [eV]	ℓ	Γ [eV]	ω_p [eV]
This work	3570 ± 50	1	300 ± 30	0.122 ± 0.044
	8400 ± 20	1	75 ± 25	2.05 ± 0.21
	21100 ± 300	0	300 ± 250	0.26 ± 0.13
	34400 ± 200	1	1600 ± 1000	4.21 ± 1.01
Koehler *et al.* [Koe93]	3510 ± 40	1	$280\ ^{+140}_{-80}$	0.096 ± 0.019
	8300 ± 45	0	$40\ ^{+80}_{-31}$	0.95 ± 0.19
	20495 ± 500	0	$1140\ ^{+2660}_{-1040}$	0.11 ± 0.05
	34675 ± 540	1	$2090\ ^{+1160}_{-790}$	6.4 ± 1.5
Gledenov *et al.* [Gle85]	3500 ± 300			0.08 ± 0.03
	8200 ± 900			1.7 ± 0.3

Table 5.4: Comparison of the resonance parameters obtained in this work with the parameters reported by Koehler *et al.* [Koe93] and Gledenov *et al.* [Gle85].

Γ's over the two resonances is incorrect in the work of Koehler *et al.* [Koe93], explaining the difference in spin assignment.

Finally, it can be concluded that the resonance parameters obtained in this work are in agreement with the previous measurements. But the accuracy obtained in this work is better leading to more reliable resonance parameters and MACS values.

5.5 Astrophysical implications

5.5.1 Determination of the MACS

The obtained MACS values shown in figure 5.9 are calculated by numerical integration of the obtained cross section. They are compared with the values obtained by Koehler *et al.* [Koe93] and a reasonable agreement is found between both. This is not surprising since the poorer resolution in the experiment of Koehler *et al.* [Koe93] does not affect the MACS computation. The calculated MACS values are compared with theoretical values of MOST [Gor] and NON-SMOKER [Rau]. A good agreement with the NON-SMOKER calculations can be observed.

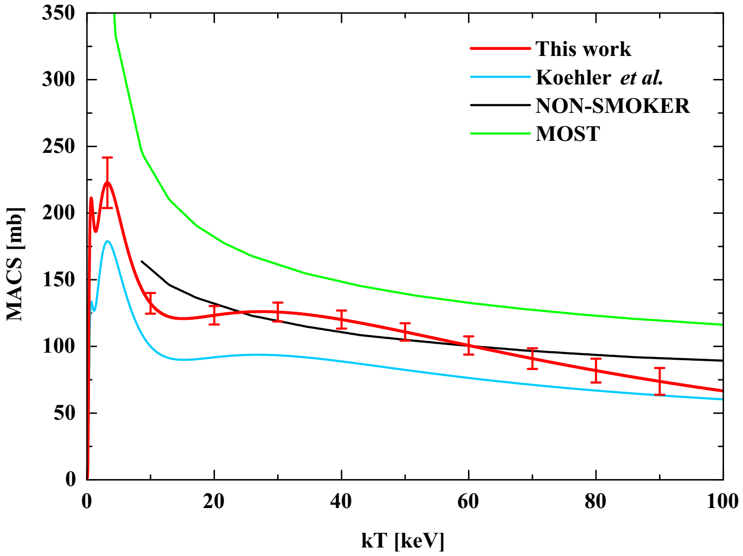

Figure 5.9: The ^{36}Cl(n,p)^{36}S plus ^{36}Cl(n,α)^{33}P MACS values represented by the red line obtained by numerical integration of the obtained cross section data. A comparison is made with the data of Koehler *et al.* [Koe93] (blue line) and with theoretical values.

5.5.2 Origin of ^{36}S

The discussion on the influence of these new MACS values on the origin of ^{36}S can be found in subsection 6.5.2.

Chapter 6

^{41}Ca measurement

In this measurement the ^{41}Ca(n,α)^{38}Ar reaction was studied. No measurements at all are reported on the ^{41}Ca(n,α)^{38}Ar reaction in the resonance region. This measurement is the first in a series of experiments planned to determine the ^{41}Ca(n,α)^{38}Ar cross section from subthermal up to about 200 keV.

6.1 Experimental setup

The ^{41}Ca(n,α)^{38}Ar reaction was measured at the same flight path as the ^{26}Al(n,α)^{23}Na reaction, at 8.5 m (FP13). The frequency of the LINAC was 800 Hz with an electron pulse width of 1 ns. The cross section could be measured from some hundreds eV up to approximately 45 keV.

The depicted level scheme in figure 6.1 shows that both (n,p) and (n,α) reactions are possible. The Q-values and corresponding particle energies for the reactions shown in figure 6.1 are listed in table 6.1.

During the (n,p) and (n,α) measurements at thermal energy performed at the ILL in Grenoble by Wagemans *et al.* [Wag98], the presence of several transitions in between the α_0- and α_1-transtitions were observed. They were interpreted as ^{41}Ca(n,$\gamma\alpha_0$)^{38}Ar transitions, a two step decay facilitated by the large Q$_{\alpha_0}$-value. The α-energy lies in between those of the α_0- and α_1-particles. These reactions may also be expected in the resonance region. In the level scheme of figure 6.1, the level feeded by γ-decay is depicted with a dashed line as several level energies are possible.

An optimal functioning of the ionization chamber was ensured by using the

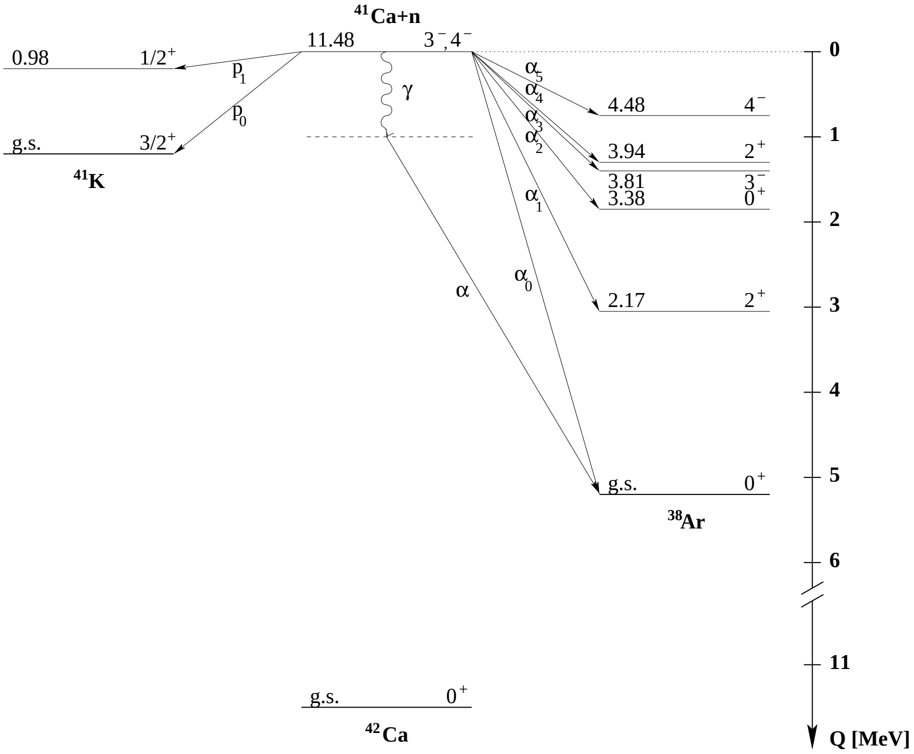

Figure 6.1: Level scheme for the ^{41}Ca(n,p$_i$)^{41}K and ^{41}Ca(n,α_i)^{38}Ar reactions. The energies are in MeV.

	Q-value [MeV]	E [MeV]
p_0	1.20	1.17
p_1	0.22	0.21
α_0	5.22	4.72
α_1	3.05	2.76
α_2	1.84	1.66
α_3	1.41	1.28
α_4	1.28	1.16
α_5	0.74	0.67

Table 6.1: Q-values and corresponding energies for the possible ^{41}Ca(n,p$_i$)^{41}K and ^{41}Ca(n,α_i)^{38}Ar reactions.

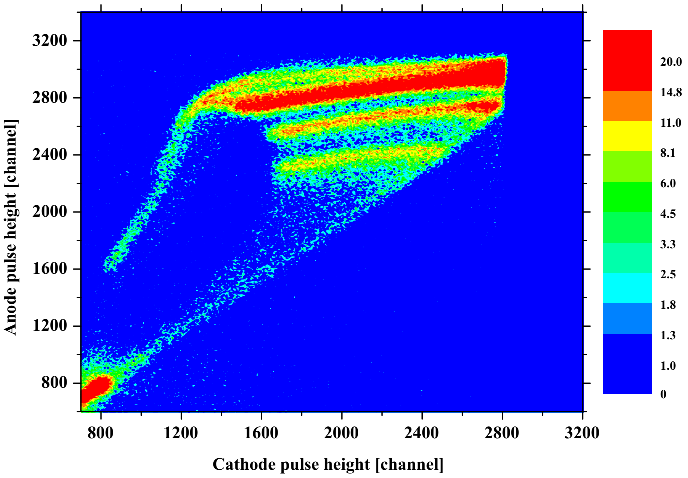

Figure 6.2: Anode versus cathode spectrum for the first ^{41}Ca(n,α_i)^{38}Ar measurement.

following parameters: V_A = 1950 V, V_C = -3100 V, V_G = 0 V, d_{cg} = 3.9 cm, d_{ag} = 1.2 cm and the methane gas pressure was 1 + 0.2 atm. Once again the charged particles were detected in a 2π upstream direction. The same ionization chamber as in the ^{26}Al measurement was used. However, for this measurement there is no particular need to use this little chamber.

6.2 Data analysis

6.2.1 ^{41}Ca measurement

The anode versus cathode pulse height spectrum is depicted in figure 6.2. Several reactions can be observed. According to the electronic setup settings of this measurement, the α_0-particles should appear in the anode spectrum around channel number 2725, the α_1-particles are expected around channel number 1540 and the α_2-particles in channel 875. Figure 6.2 makes clear that apart from the expected α-particles other charged particles are detected. To find out if they are neutron induced charged particle reactions on other nuclei present in the ^{41}Ca sample or decay reactions from impurities in the sample or in the ionization chamber, a measurement without neutrons was

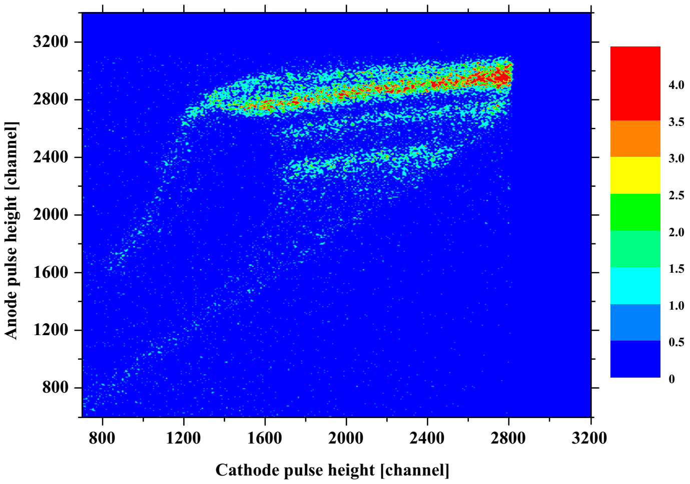

Figure 6.3: Anode versus cathode spectrum for the measurement without neutrons. The counts registered are originating from the decay of impurities present in the ^{41}Ca sample.

performed. The resulting anode versus cathode spectrum is shown in figure 6.3. It makes clear that some unstable nuclei other than ^{41}Ca are present in the sample. They emit charged particles with comparable energy as the α_0-particles from the ^{41}Ca(n,α_0) reaction and are thus detected by the ionization chamber. Because decay is not affected by the 800 Hz LINAC frequency, the 'decay counts' appear randomly in the TOF spectrum, leading to a constant contribution. By fitting this TOF spectrum with a constant function, after putting the same anode and cathode software windows as in the measurement with LINAC and after normalization to the same measuring time, the counts coming from the decay can be subtracted from the ^{41}Ca TOF spectrum. In this way, the detected 'decay counts' do not contribute to the final ^{41}Ca(n,α) cross section.

Figure 6.2 shows that counts at cathode channel number 2800 seem to be cut off. This is due to a too high amplification of the cathode signal. To check if α_0-particles are lost with this setup, a new measurement has been performed for which the amplification of both cathode and anode signals was lowered. As a consequence, other charged particles from decaying nuclei in the ^{41}Ca sample or in the ionization chamber were detected, which can be seen

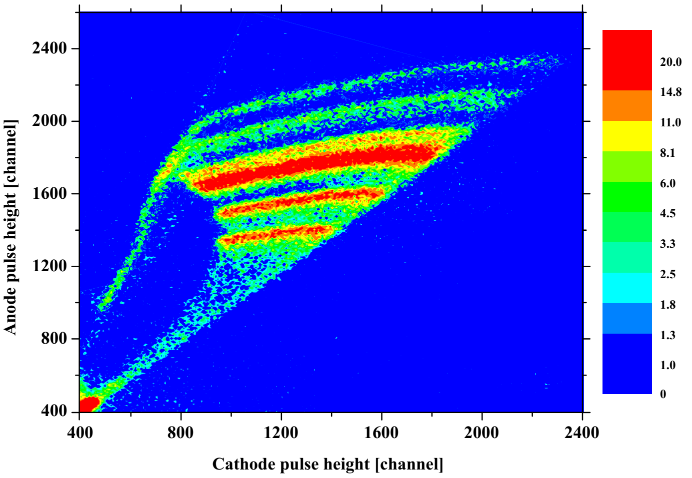

Figure 6.4: Anode versus cathode spectrum for the second ^{41}Ca(n,α_i)^{38}Ar measurement. No software windows have been put.

in figure 6.4. For both measurements a selection on one specific resonance in the TOF spectrum has been made and the corresponding anode counts are summed. This is done for several resonances. After comparing both sums for the different resonances, it is concluded that in the first measurement, no counts were lost due to the amplification factor. Therefore, both TOF spectra may be summed to determine the ^{41}Ca(n,α) cross section. However, due to the different amplifications, the anode and cathode software windows will be different. Also the TOF fit coming from the 'decay counts' will be different. As a result, an additional 'decay' background measurement was done with the lowered amplifications.

To separate the different α-particles from the ^{41}Ca(n,α) reaction, a baseline correction has been performed first. For the same reason as in the ^{36}Cl measurement, it was impossible to determine the baseline in a proper way in the measurement with the ^{41}Ca sample. Therefore the baseline correction function of the corresponding flux measurement, with a ^{10}B sample, has been used. Once more, one should remark that different correction functions are used for the two measurements with different amplification factors.

In a second step, in order to separate the different α-particles, a selection of the four biggest resonances in the TOF spectrum has been made. The cor-

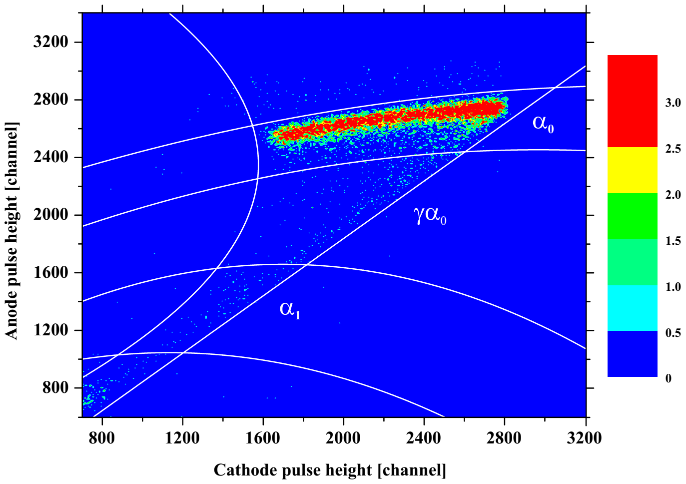

Figure 6.5: Anode versus cathode spectrum after selection in TOF for the four biggest resonances appearing. The lines represent the software windows which are put to select the different ^{41}Ca(n,α_i) reactions.

responding anode versus cathode spectrum is shown in figure 6.5. To minimize the number of counts not coming from the ^{41}Ca(n,α_i) reaction, the software windows on anode and cathode are chosen as shown in figure 6.5 with white lines. As can be seen in figure 6.5 the determination of the borderline between ^{41}Ca(n,α_0) and ^{41}Ca(n,$\gamma\alpha_0$) and the borderline between ^{41}Ca(n,$\gamma\alpha_0$) and ^{41}Ca(n,α_1) was not clear, because of the low count rate for the (n,$\gamma\alpha_0$) and (n,α_1) reactions. The used borderlines are based on the calculated channel numbers in the anode spectrum (based on the particle energies) and on the shape of the upper level borderline for the ^{41}Ca(n,α_0) reaction. The anode spectrum for the four biggest resonances appearing in the TOF spectrum obtained after selection of the different α-particles is shown in figure 6.6. The different colours indicate the different α-particles. In figure 6.7 the anode versus TOF spectrum after selection of all the α-particles is depicted. A careful look on the plot shows a broad continuous anode signal for each resonance, which means that there are indeed ^{41}Ca(n,$\gamma\alpha_0$) counts, as observed with thermal neutrons by Wagemans *et al.* [Wag98].

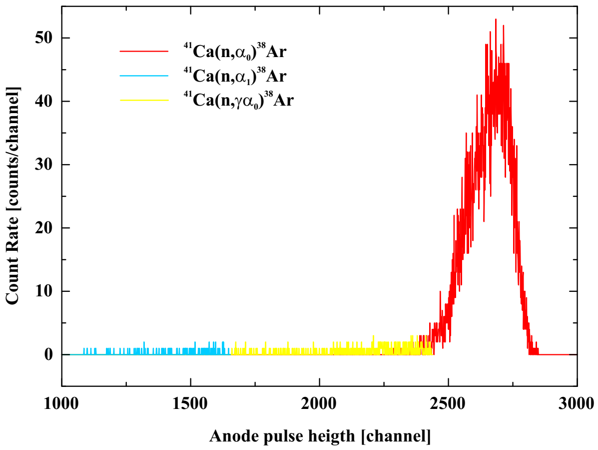

Figure 6.6: Anode spectrum for the four biggest resonances appearing in the TOF spectrum after selection of the different α-particles, each of them is represented with a different colour.

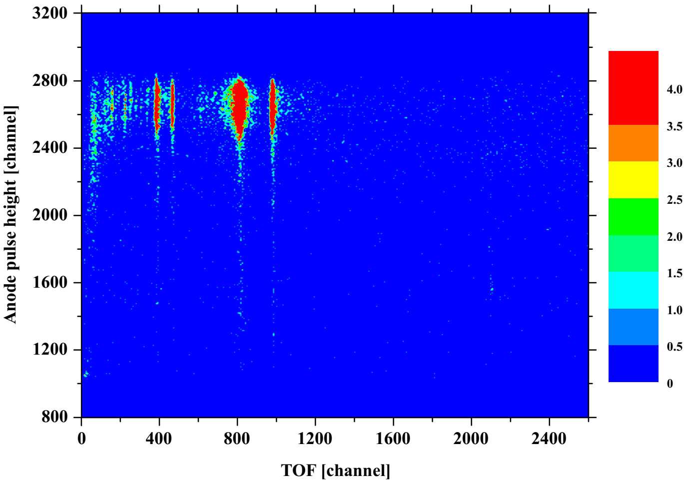

Figure 6.7: Anode versus TOF spectrum after selection in anode and cathode pulse heights of all the α-particles from the ^{41}Ca(n,α_i) reactions. For each resonance, a broad continuous anode signal can be observed. These are the ^{41}Ca(n,$\gamma\alpha_0$) reactions. Remark the faint region of counts around TOF 2100 and anode channel 1600, representing a resonance consisting of α_1-particles, but no α_0-particles.

6.2.2 Flux determination

As mentioned in the previous subsection, a ^{10}B sample is used for the determination of the energy dependent neutron flux. A baseline correction has been performed before putting software windows on the anode and cathode pulse heights to select the α_i-particles. After background subtraction, the efficiency of the detector has been accounted for as explained in subsection 3.5.3.

6.2.3 Background determination

For the determination of the energy dependent background, two runs have been performed: one with a Mn filter and one with Au, Rh, Co and W filters. Using formula 3.20, a fit through the black resonance points has been performed. In the case of the ^{41}Ca measurement, the counts in the black resonance zones were so low, that a power function with the same form as the one used for the determination of the flux background has been chosen. This means that the fit parameter c in formula 3.20 is fixed to the fit value from the flux background fit. However, for the background determination of the ^{41}Ca(n,α_1) and ^{41}Ca(n,$\gamma\alpha_0$) reaction, the count rate in the black resonance zones was too low to fit with the power funtion 3.20 and therefore a constant fit was used.

6.2.4 Determination of the number of atoms in the samples used

In subsection 3.7.3 it has been mentioned that the ^{41}Ca sample contained $(3.36 \pm 0.44) \times 10^{17}$ ^{41}Ca atoms.

The same ^{10}B sample as used during the ^{36}Cl measurement has been used. It contained $(7.17 \pm 0.13) \times 10^{19}$ atoms (see subsection 5.2.4).

6.3 Calculation of the cross section

The delay Δ and the exact flight path length are determined with the help of Al resonances during a seperate run with a thin Al filter in the neutron beam. The narrow resonances from the Cd overlap filter and the background filters during the flux measurements are used to check the delay Δ and the flight path length. After conversion from TOF to energy and after combination of the count rates following equation 3.25, the total ^{41}Ca(n,α)^{38}Ar cross section could be determined, as shown in figure 6.8. The uncertainty on the cross section

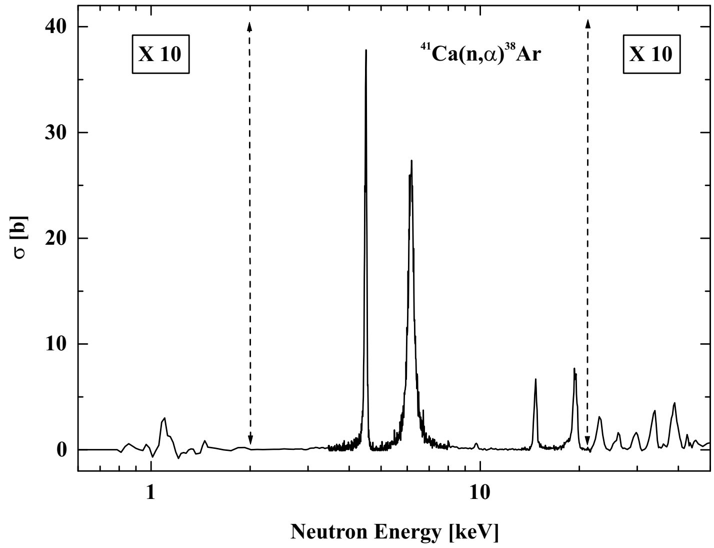

Figure 6.8: The ^{41}Ca(n,α)^{38}Ar cross section.

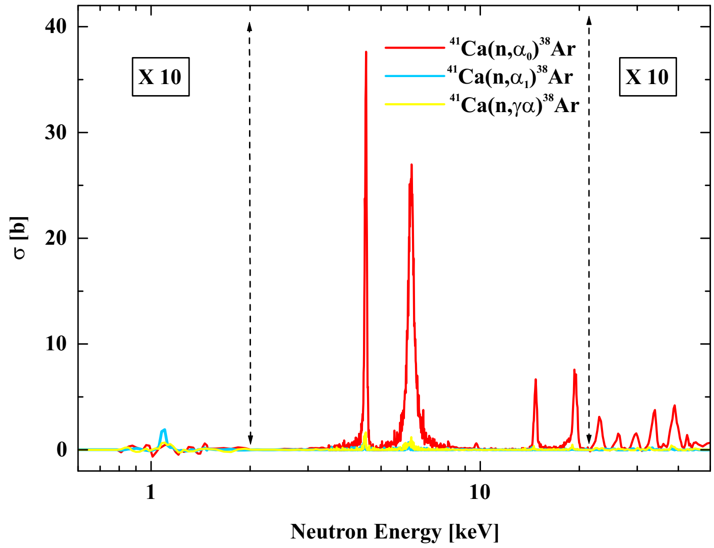

Figure 6.9: The partial ^{41}Ca(n,α_i) reaction cross sections.

Energy [eV]	Area [b.eV]	Γ [eV]
1090 ± 70	30 ± 15	
4490 ± 10	3400 ± 300	40 ± 20
6170 ± 60	11350 ± 950	260 ± 26
9725 ± 75	170 ± 60	125 ± 100
14725 ± 75	2500 ± 300	175 ± 140
18450 ± 300 [a]		
19430 ± 150	5800 ± 600	420 ± 100
23080 ± 200	400 ± 150	600 ± 200
26100 ± 800 [b]		
29700 ± 700	250 ± 100	1250 ± 1000
33700 ± 700	550 ± 220	1000 ± 600
38850 ± 1200	900 ± 300	2000 ± 1200

[a] The resonance at 19.43 keV is a double resonance with a first level at 18.45 keV.
[b] Too low counting statistics, so the area has not been fitted.

Table 6.2: Resonance parameters obtained from the Voigt fits. The natural line width Γ is calculated only for these resonances for which the total fitted width is much bigger than the experimental broadening and for these resonances for which the Voigt fit was good.

values is a combination of the statistical uncertainties on the count rates, uncertainties on the number of atoms in the samples used and the uncertainty on the ^{10}B(n,α) reference cross section taken from the ENDF/B-VI nuclear data library.

The partial cross sections are plotted in figure 6.9. For all of them, the same analysing procedure has been followed to determine the cross section. From figure 6.9 it is clear that the resonance at 1.1 keV is due to a (n,α_1) reaction. The other resonances are mainly due to (n,α_0) reactions.

6.4 Resonance analysis

6.4.1 Fitting procedure

As explained in subsection 4.4.1 the obtained cross section values for ^{41}Ca(n,α)^{38}Ar are fitted with Voigt shapes to determine the energy position, the area and the total level width. The results of these Voigt fits are listed in table 6.2. The uncertainties are taken from the fit. If these were too small,

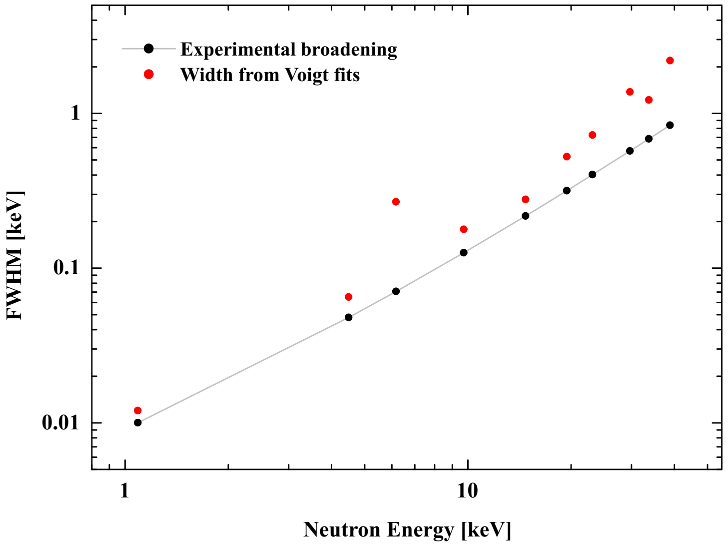

Figure 6.10: The total broadened width obtained from the Voigt fits (red points) compared with the calculated experimental broadening contribution for each observed resonance.

a more realistic uncertainty was estimated. Again the experimental broadening for the resonances was calculated and kept fixed during the fit. This experimental broadening is plotted in figure 6.10 together with the total width obtained from the Voigt fit at the energy position of each resonance. Figure 6.10 makes clear that, in principle, it should be possible to calculate the natural line width for each resonance. However, for some resonances the quality of the Voigt fit was poor. For these cases, a conservative uncertainty on the natural line width was adopted. The resulting Voigt fits are shown in figure 6.11 for the resonances at 4.49 keV, 6.17 keV, 14.7 keV and 19.4 keV. The second plot illustrates that the peak at 19.4 keV consists of two resonances.

6.4.2 Spin assignment

various possibilities

s-wave (ℓ=0) neutrons impinging on ^{41}Ca, ground state $I^\pi = \frac{7}{2}^-$, will populate the $J^\pi = 3^-$ and $J^\pi = 4^-$ states of the compound nucleus ^{42}Ca, whereas p-

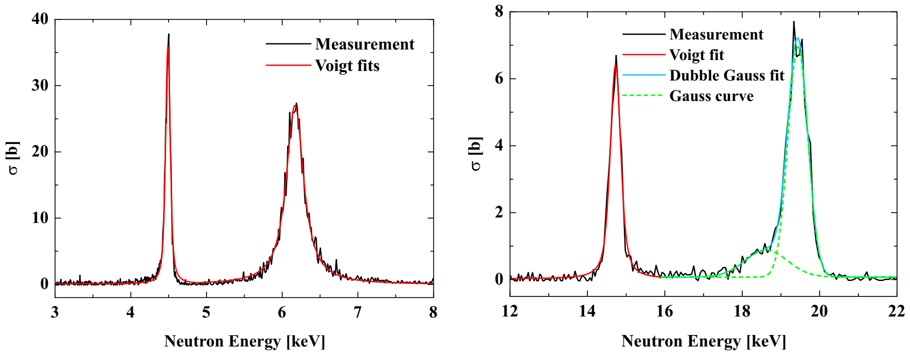

Figure 6.11: Voigt fits to the measured ^{41}Ca(n,α) cross section data for some resonances.

wave (ℓ=1) neutrons can populate states from J$^{\pi}$ = 2^{+} through J$^{\pi}$ = 5^{+}. The formed states decay to the ground (J$^{\pi}$ = 0^{+}) or first excited state (J$^{\pi}$ = 2^{+}) of ^{38}Ar by emitting α_0- or α_1-particles, respectively, as illustrated in figure 6.1. The smallest allowed angular momenta of the emitted α-particles are tabulated in the upper part of table 6.3.

In the special case of (n,$\gamma\alpha$) transitions, Wagemans *et al.* [Wag94] concluded that the γ-decay is a M1-transition. Following the selection rules, the parity of the initial and final state needs to be the same for a M1-transition: $\pi_i = \pi_f$. Therefore, for s-wave neutrons from the 3^{-} state in ^{42}Ca, 2^{-}, 3^{-} and 4^{-} states in ^{42}Ca are possible after γ-decay, while from the 4^{-} state, 3^{-}, 4^{-} and 5^{-} states may be populated. For p-wave neutrons, intermediate states from 1^{+} to 6^{+} are possible. In this work only (n,$\gamma\alpha_0$) transitions could be measured, because for the other (n,$\gamma\alpha_i$) transitions, the final α-particles had not enough energy to be detected with the used amplification in the electronic setup. For that reason only the (n,$\gamma\alpha_0$) transitions will be discussed here. The allowed angular momenta for α_0-decay from the intermediate states of ^{42}Ca to the ground state of ^{38}Ar are tabulated in the lower part of table 6.3.

assignments based on this work

As mentioned before, Wagemans *et al.* [Wag98] measured the ^{41}Ca(n,α_i) reaction cross section with thermal neutrons. These thermal cross sections are

J^π ^{38}Ar	J^π ^{42}Ca compound nucleus					
	s-wave		**p-wave**			
	3^-	4^-	2^+	3^+	4^+	5^+
0^+ (α_0)	3	p.f.	2	p.f.	4	p.f.
2^+ (α_1)	1	3	0	2	2	4

J^π ^{38}Ar	J^π intermediate state									
	2^-	3^-	4^-	5^-	1^+	2^+	3^+	4^+	5^+	6^+
0^+ ($\gamma\alpha_0$)	p.f.	3	p.f.	5	p.f.	2	p.f.	4	p.f.	6

p.f. = parity forbidden

Table 6.3: *Upper part:* smallest allowed angular momenta of the emitted α-particles from the formed compound nucleus ^{42}Ca in the case of impinging s- or p-wave neutrons.
Lower part: angular momenta of the α_0-particles in the case of $\gamma\alpha_0$-transitions to the ground state of ^{38}Ar.

Transition	Thermal Cross Section [mb] [Wag98]
α_0	42 ± 6
α_1	130 ± 25
$\gamma\alpha$	10 ± 2

Table 6.4: Thermal cross sections for the different α-reactions determined by Wagemans *et al.* [Wag98].

listed in table 6.4. From the calculated total natural line width, the contribution from a s-wave resonance to the thermal cross section can be calculated with formula 1.24. If this calculated value is higher than the measured thermal cross section, the resonance is taken as a p-wave. On the basis of these calculations it is concluded that only the resonances around 1.1 keV and 10 keV may be s-wave, because for all the other resonances the thermal extrapolation is much higher than the measured thermal cross section. Although the natural line width could not be determined for the resonance at 1.1 keV, it can be deduced that its thermal contribution in the case of a s-wave will not exceed the measured thermal cross section.

Figure 6.7 shows that the resonance at 1.1 keV is a transition only to the first excited state of ^{38}Ar, because neither in the ^{41}Ca(n,α_0) nor in the

^{41}Ca(n,$\gamma\alpha_0$) cross section this resonance appears. Taking into account the spin assignments for s-wave neutrons, the only possibility is that this resonance corresponds to a 4^- state of ^{42}Ca.

On the contrary, the 10 keV resonance appears in (n,α_0), (n,α_1) as well as in (n,$\gamma\alpha_0$) transitions, although it is hard to recognize a peak around 10 keV in the (n,α_1) and (n,$\gamma\alpha_0$) cross section because of the low count rate. With the help of table 6.3, it is concluded that the 10 keV resonance is a 3^- state in ^{42}Ca.

All the other resonances are considered to be p-wave. Because (n,α_0), (n,$\gamma\alpha_0$) and (n,α_1) transitions are observed in all of them, these resonances are most probably 2^+ states as 3^+ and 5^+ states are ruled out by parity constraints and the 4^+ state is less probable because the higher orbital momentum of the α-particle reduces the penetrability through the centrifugal barrier.

In principle, interference effects between two neighbouring resonances with the same spin can reduce the contribution to the thermal cross section, leaving open the possibility of a different spin assignment for some resonances. This would lead to a non 1/v-behaviour of the cross section at low neutron energy. The experimental cross section obtained in this work shows some possible interference effects between the resonances at 4.5 keV and 6.2 keV and between 14.7 keV and the doublet around 19 keV. This can be observed in figure 6.11, where the Voigt fit for the resonance at 4.5 keV is not fitting well the experimental data at the high energy tail [Mox05]. The same effect appears for the resonance at 14.7 keV at its low energy tail. The fact that the experimental cross section between the resonances at 14.7 keV and 19 keV does not fall to zero, gives a second hint of interference between both resonances [Mox05].

6.4.3 Determination of the partial level widths

The only additional information on ^{42}Ca compound levels in the covered energy range was obtained in a proton induced reaction on ^{41}K by Meijer and Van Gasteren [Mei70]. They reported a list of $\omega_p = (2J+1)\Gamma_p\Gamma_{\alpha_0}/\Gamma$ values for the measured ^{41}K(p,α_0)^{38}Ar reaction. The Γ_p-value from their work corresponds with p$_0$-decay in the case of neutron induced reactions on ^{41}Ca. From the level scheme in figure 6.1 it can be deduced that in the case of a neutron induced reaction on ^{41}Ca only p$_0$- and p$_1$-decay to ^{41}K is possible, so $\Gamma_p = \Gamma_{p_0} + \Gamma_{p_1}$. However, the probability that the p$_1$-particles penetrate the

Energy [eV]	ω_α [eV]	ω_p [eV] [Mei70]	$\frac{\Gamma_n}{\Gamma_p}$
4490 ± 10	3.73 ± 0.33	7.4	8.07 ± 0.71
9725 ± 75	0.40 ± 0.14	9.2	0.70 ± 0.25
14725 ± 75	9.00 ± 1.08	2.1	68.57 ± 8.24
19430 ± 150	27.55 ± 2.86	1.6	275.5 ± 28.6
23080 ± 200	2.26 ± 0.85	2.8	12.90 ± 4.84
29700 ± 700	1.82 ± 0.73	2.4	12.10 ± 4.85
33700 ± 700	4.53 ± 1.82	5.7	12.72 ± 5.09
38850 ± 1200	8.55 ± 2.86	2.9	47.16 ± 15.79

Table 6.5: $\frac{\Gamma_n}{\Gamma_p}$ for the resonances observed in this work which correspond to resonances observed by Meijer and Van Gasteren [Mei70].

Coulomb barrier is very low. Therefore, it can be assumed that $\Gamma_p = \Gamma_{p_0}$ in a neutron induced measurement. Consequently, Γ_p from the measurement of Meijer and Van Gasteren [Mei70] is equal to Γ_p from this work. By dividing the fitted resonance strength ω_α obtained in this work ($\omega_\alpha = g\frac{\Gamma_n\Gamma_\alpha}{\Gamma} = \frac{(2J+1)}{16}\frac{\Gamma_n\Gamma_\alpha}{\Gamma}$ and is proportional to the resonance area), by the reported ω_p-value of Meijer and Van Gasteren [Mei70], a value for $\frac{\Gamma_n}{\Gamma_p}$ is obtained. The values for $\frac{\Gamma_n}{\Gamma_p}$ for the resonances observed in this work which correspond to resonances observed by Meijer and Van Gasteren [Mei70] are listed in table 6.5.

The partial widths may be calculated through combining the expressions for ω_p and ω_α mentioned above, and the expression for the total width $\Gamma = \Gamma_n + \Gamma_\gamma + \Gamma_p + \Gamma_\alpha$. Taking $\Gamma_\gamma = 1$ eV, which is a generally adopted value in this mass region [Mug81], the Γ_p partial width can be calculated from the following equation:.

$$\Gamma_p = \frac{\Gamma - \Gamma_\gamma \pm \sqrt{(\Gamma - \Gamma_\gamma)^2 - \frac{4\omega_p\Gamma}{2J+1}\left(16\frac{\omega_\alpha}{\omega_p} + 1\right)}}{2\left(16\frac{\omega_\alpha}{\omega_p} + 1\right)}. \tag{6.1}$$

Once Γ_p is known, Γ_n is determined via the $\frac{\Gamma_n}{\Gamma_p}$ ratio and finally Γ_α follows from:

$$\Gamma_\alpha = \Gamma - \Gamma_\gamma - \Gamma_n - \Gamma_p. \tag{6.2}$$

In this way, for every J-value two sets of partial widths are obtained. The requirement that the quantity under the square root must be greater than

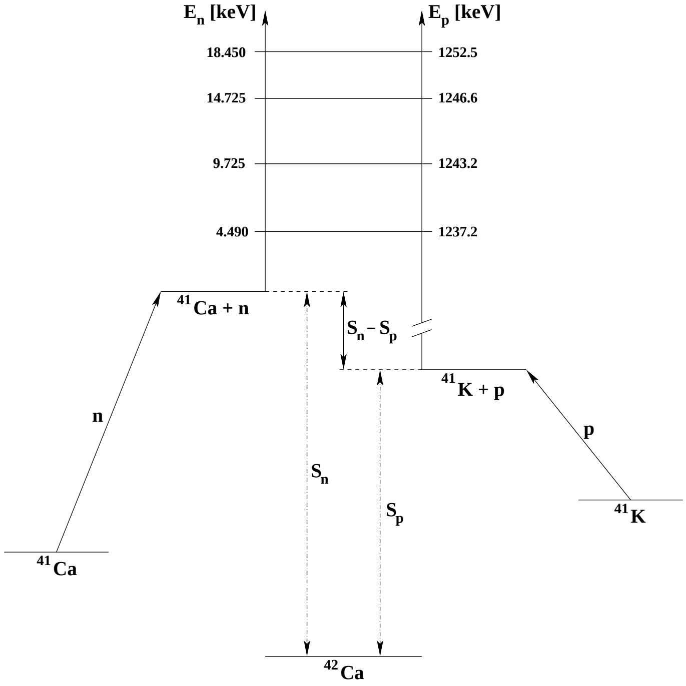

Figure 6.12: Determination of $S_n - S_p$ from ^{42}Ca levels excited through ^{41}Ca(n,α)^{38}Ar and ^{41}K(p,α_0)^{38}Ar reactions. The resonance energies are taken from the experimental data and have to be transformed into COM units.

zero, sets a lower limit on the possible J-values. In this work, the uncertainties on Γ are too high to calculate meaningfull partial widths. Additional cross section measurements with reactions leading to the ^{42}Ca compound nucleus are needed to obtain more accurate values for Γ, a value for $\Gamma_n\Gamma_\alpha/\Gamma$, and an unambiguous spin determination. When this information is available, the partial widths can be calculated and used as input parameters in RSA codes. This will lead to the final values for the resonance parameters and to the fit to the experimental cross section data.

6.4.4 Nuclear binding energies

Other interesting information that can be extracted from the proton induced reaction on ^{41}K leading to the same ^{42}Ca compound nucleus is information

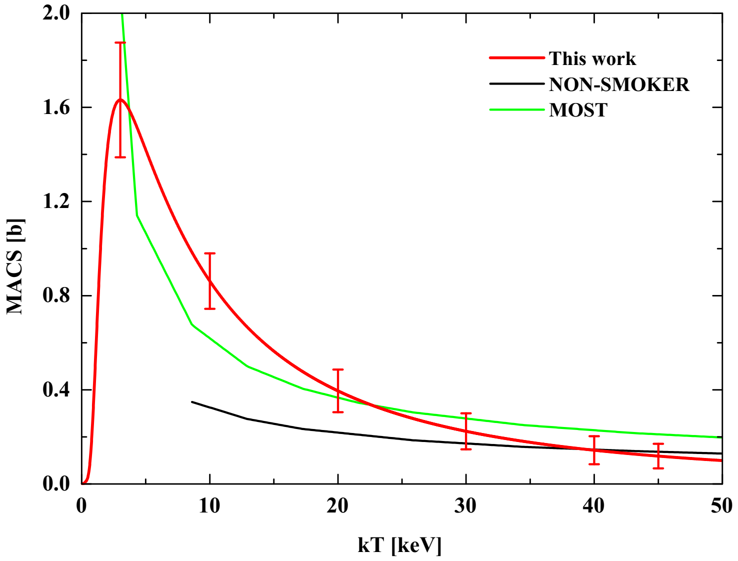

Figure 6.13: The ^{41}Ca(n,α_0+$\gamma\alpha_0$+α_1)^{38}Ar MACS values obtained by numerical integration of the obtained cross section data (red line). A comparison is made with theoretical values.

on nuclear binding energies. From the ^{41}Ca(n,α)^{38}Ar measurement and the ^{41}K(p,α_0)^{38}Ar measurement, the difference between the neutron and proton binding energy can be calculated. Figure 6.12 shows how $S_n - S_p$ can be obtained for ^{42}Ca by combining the observed resonance peak positions from ^{41}Ca(n,α) with the peak positions from the ^{41}K(p,α_0) measurement. After transforming the resonance peak energies to COM units, a value for $S_n - S_p$ of (1203.62 ± 1.5) keV is obtained. This value is in perfect agreement with the evaluated value of (1203.66 ± 0.20) keV [Aud03].

6.5 Astrophysical implications

6.5.1 Determination of the MACS

The ^{41}Ca(n,α) MACS values are obtained by numerical integration of the determined cross section and are shown in figure 6.13. Because in this work the cross section is obtained up to an energy of approximately 45 keV and because a resonance at E$_{res}$ has its maximum contribution at kT = E$_{res}$/2 (see section 1.2), the obtained MACS values above 22 keV are lower limits. As this ^{41}Ca(n,α) measurement is the first ever reported in the resonance region, the calculated MACS values can only be compared with theoretical values. In figure 6.13 the comparison is made with the values obtained from the MOST [Gor] and the NON-SMOKER [Rau] codes. In the energy region covered by the experiment, two stellar temperatures are of interest in s-process network calculations: 8 keV and 25 keV. For 8 keV, it is clear from figure 6.13 that the theoretical models strongly underestimate the MACS value. The MOST value is about half of the value obtained in this work and the NON-SMOKER value is even three times smaller. At 25 keV, the MOST value is in agreement with the measured MACS value, but still, the NON-SMOKER value is about half of the value obtained in this work.

6.5.2 Origin of ^{36}S

As described in section 2.3, ^{36}S is believed to be synthesized during the s-process, in particular during the weak s-process. To check this hypothesis, nucleosynthesis network calculations in the mass region between $28 \leq A \leq 42$ are necessary. This s-process network is shown in figure 2.5 on page 29. It can be seen that both measured reactions, ^{36}Cl(n,p)^{36}S as well as ^{41}Ca(n,α)^{38}Ar, are of importance in the network. The ^{36}Cl(n,p) reaction influences the ^{36}S abundance in a direct way, while the ^{41}Ca(n,α) reaction recycles to ^{36}S via the following reaction chain: ^{41}Ca(n,α)^{38}Ar(n,γ)^{39}Ar(n,α)^{36}S.

Although the ^{39}Ar(n,α)^{36}S channel is less important than the ^{36}Cl(n,p)^{36}S channel for the production of ^{36}S, it is included in the stellar models. Moreover, the ^{41}Ca(n,α)^{38}Ar reaction is considered as the most important neutron induced reaction on ^{41}Ca in the temperature range of the weak s-process. As a second part of the weak s-process occurs around 86 keV, an additional measurement on a longer flight path at the GELINA facility is planned in order to extend the energy range covered by this experiment. Therefore, the obtained ^{41}Ca(n,α) MACS values are not yet used in the stellar models, which still have to rely on the theoretical MACS values.

On the other hand, the new ^{36}Cl(n,p)^{36}S MACS values are used in stellar model calculations by the group of R. Gallino at the university of Torino. They concluded that the Galactic contribution from the main s-process, occurring in AGB stars during the convective He pulses, to solar ^{36}S is very minor. On the other hand, the weak s-process, occuring in massive stars during convective He-core burning followed by convective C-shell burning, can be ascribed to account for almost the entire production of solar ^{36}S. However, it turns out that some additional ^{36}S contribution is needed to explain the total solar ^{36}S abundance. At present, it is assumed that improved network calculations, and pre-supernova and explosive nucleosynthesis may account for this missing solar ^{36}S contribution [Gal05, Mau04]. The calculations to confirm these assumptions are in full progress.

6.5.3 The ^{40}K cosmic clock

Besides the importance in the search for the origin of ^{36}S, the recycling of ^{41}Ca towards ^{38}Ar is important in dating the age of the chemical elements. An in depth discussion on nucleocosmochronology or dating the age of the chemical elements can be found in [Rol88].

Since radioactive isotopes like ^{40}K exist naturally, they must have been produced some finite time ago, otherwise ^{40}K should have been decayed by now. Nucleocosmochronology uses the observed relative abundances of radioactive nuclei to determine time scales for the nucleosynthesis of these nuclei. As the Sun only transforms hydrogen into helium, the heavy elements present in the solar system were synthesized elsewhere. Therefore, the origin of the solar system elements must date back to a time prior to the formation of the solar system ($\sim 4.6 \times 10^9$ y). So, radioactive nuclei with lifetimes of the order of the age of the solar system are useful as cosmic clock.

Starting from a s-process origin for ^{40}K, Beer and Penzhorn [Bee87] deduced an upper limit for the age of the elements of 9.6×10^9 y. However, in their paper, the ^{39}Ar branching was identified as one of the remaining uncertainties in the determination of the age of the elements. As ^{39}Ar is formed after n-captures on ^{38}Ar and ^{38}Ar in turn is partly formed through (n,α) reactions on ^{41}Ca, the studied reaction in this work is of importance in dating the age of the elements.

Chapter 7

Conclusions and outlook

In this work (n,p) and (n,α) reactions on ^{26}Al, ^{36}Cl and ^{41}Ca are studied as a function of the neutron energy. The measurements were performed at the GELINA time-of-flight facility of the IRMM in Geel, Belgium, where high resolution data can be obtained. Besides the nuclear physics information obtained from the resonance analysis of the reaction cross sections, the studied reactions are of importance in the understanding of the observed ^{36}S and ^{26}Al abundances.

In the case of ^{26}Al, the ^{26}Al(n,α)^{23}Na partial cross section up to 45 keV has been determined. Six resonances are observed with a good accuracy. For three of them, the total level width and the spin of the state formed in the compound nucleus could be calculated. For most of the resonances the obtained resonance parameters are in agreement with previous data [Koe97, Ske87, Kav, Dou89]. The calculated MACS values used in stellar model calculations confirm that ^{26}Al is indeed severely depleted by neutron captures in AGB stars. In this respect, the ^{26}Al(n,p) reaction is of importance too. It even turns out that the (n,p) reaction is more important than the (n,α) reaction. However, many different factors are used for the (n,p)/(n,α) importance, arising the question whether the (n,p) MACS values used at present are reliable. So, to understand the abundance of ^{26}Al in our Galaxy, a new ^{26}Al(n,p)^{26}Mg measurement which covers the neutron energy region up to approximately 300 keV is desirable in the near future.

In the (n,p) + (n,α) measurements on ^{36}Cl eighteen resonances are observed with a high accuracy. This is more than twice as was identified before [Koe93]. Only the lowest energy resonance at 0.93 keV shows a significant (n,α)-contribution of (76 ± 7) %, which is in perfect agreement with the value reported before [Koe93]. Furthermore, for four resonances, the resonance strength, the spin, the total width Γ and the partial width Γ_p could be determined. They are in good agreement with previous data [Koe93, Gle85], but the achieved accuracy is better. The calculated MACS values are used in stellar model calculations to trace the origin of ^{36}S. The new MACS values reveal that the weak component of the s-process occurring in massive stars accounts for almost the entire production of solar ^{36}S.

The ^{41}Ca(n,α)^{38}Ar measurement is the first ever reported in the resonance region. During this measurement the α-decay to the ground state as well as to the first excited state of ^{38}Ar is measured. The presence of several transitions in between the α_0- and α_1-transitions, observed during a thermal cross section measurement [Wag98], is confirmed. These transitions are interpreted as a two step transition: first γ-decay to a lower excited state in the compound nucleus ^{42}Ca followed by α-decay to the ground state of ^{38}Ar, ^{41}Ca(n,$\gamma\alpha_0$)^{38}Ar. Twelve resonances are observed in the energy region up to 45 keV. For most of them the total width and the spin are determined. The lowest energy resonance at 1.1 keV appears to be only a transition to the first excited state of ^{38}Ar, while all the other resonances show (n,α_0), (n,α_1) as well as (n,$\gamma\alpha_0$) transitions. To extend the energy range and in the meantime to improve the energy resolution, a complementary measurement on a longer flight path needs to be performed at GELINA.

References

[Aud03] G. Audi, A. H. Wapstra, and C. Thibault, Nucl. Phys. A **729** (2003).

[Bas97] C. Bastian, *AGS, a Set of UNIX Commands for Neutron Data Reduction*, Proc. Int. Conf. on Neutron Research and Industry, 1996, Crete, Greece, 1997.

[Bee85] H. Beer and R. L. Macklin, Phys. Rev. C **32** (1985) 738.

[Bee87] H. Beer and R.-D. Penzhorn, Astron. Astrophys. **174** (1987) 323.

[Bee92] H. Beer, F. Voss, and R. R. Winters, The Astrophysical Journal Supplement Series **80** (1992).

[Ber04] C. A. Bertulani and P. Danielewicz, *Introduction to Nuclear Reactions*, Institute of Physics Publishing, Bristol and Philadelphia, 2004.

[BJ84] C. Budtz-Jorgensen and H.-H. Knitter, Nucl. Instr. & Meth. in Physics Research **223** (1984) 295.

[Böc90] K. H. Böckhoff, A. D. Carlson, O. A. Wasson, J. A. Harvey, and D. C. Larson, Nucl. Sci. & Eng. **106** (1990) 192.

[Boh36] N. Bohr, Nature **137** (1936) 344.

[Bor57] T. E. Bortner, G. S. Hurst, and W. B. Stone, Rev. Sci. Instrum. **28** (1957) 103.

[Bri00] J. Briesmeister, *MCNP - A General Monte Carlo N-Particle Transport Code - Version 4C2*, 2000, LA-13709-M.

[Bur57] E. M. Burbidge, G. R. Burbidge, W. A. Fowler, and F. Hoyle, Reviews of Modern Physics **29,4** (1957) 547.

[Bur63] W. E. Burcham, *Nuclear Physics an Introduction*, Longmans Green and Co LTD, London, 1963.

[Cam57] A. G. W. Cameron, Astronomical Society of the Pacific **29** (1957) 547.

[Cau88] G. R. Caughlan and W. A. Fowler, Atomic Data Nucl. Data Tables **40** (1988) 283.

[cer81] *NEANDC - 152 A*, 1981.

[Cla61] D. D. Clayton, W. A. Fowler, T. E. Hull, and B. A. Zimmerman, Ann. Phys. **12** (1961) 331.

[Cla67] D. D. Clayton and M. E. Rassbach, The Astrophysical Journal **148** (1967) 69.

[Cla68] D. D. Clayton, *Principles of Stellar Evolution and Nucleosynthesis*, McGraw - Hill, New York, 1968.

[Cla74] D. D. Clayton and R. A. Ward, The Astrophysical Journal **193** (1974) 397.

[Coa83] M. S. Coates, D. B. Gayther, G. D. James, M. C. Moxon, B. H. Patrick, M. G. Sowerby, and D. B. Syme, *Can we do more to achieve accurate nuclear data?*, Proceedings of the International Conference on Nuclear Data for Science and Technology, Antwerp, Belgium, 1983, p. 977.

[Coc96] C. Coceva and M. Magnani, *Resolution rotary target*, 1996, IRMM Internal Report GE/R/ND/06/96.

[Din01] T. Ding, S. Valkiers, and H. Kipphardt *et al.*, Geochim. Cosmochim. Acta **54** (2001) 2433.

[Dou89] G. Doukellis, Il Nuovo Cimento **101 A 4** (1989) 651.

[end] http://t2.lanl.gov/cgi-bin/nuclides/endind.

[Eva55] R. D. Evans, *The Atomic Nucleus*, McGraw - Hill Book Company INC, New York, 1955.

[Eyk91] R. Eykens, A. Goetz, A. Lamberty, J. Van Gestel, J. Pauwels, C. Wagemans, S. Druyts, and P. D'hondt, Nucl. Instr. & Meth. in Physics Research A **303** (1991) 152.

[Fer01] H. Ferdinande, *Kernfysische instrumentatie*, 2001, Vakgroep Subatomaire en Stralingsfysica, Universiteit Gent.

[Fla04] M. Flaska, A. Borella, D. Lathouwers, L. C. Mihailescu, W. Mondelaers, A. J. M. Plompen, H. van Dam, and T. H. J. J. van der Hagen, Nucl. Instr. & Meth. A **531** (2004) 392.

[Fow67] W. A. Fowler, G. R. Cauglan, and B. A. Zimmerman, Annu. Rev. Astron. Astrophys. **5** (1967) 525.

[Fri] Frisch, Unpublished report BR-49, British atomic energy project.

[Frö00] F. H. Fröhner, *Evaluation and Analysis of Nuclear Resonance Data*, 2000, AEN-NEA JEFF Report 18.

[Gal90] R. Gallino, M. Busso, G. Picchio, and C. M. Raiteri, *Chemical and Dynamical Evolution of Galaxies*, 1990, F. Matteucci, F. Ferrini, J. Franco editor.

[Gal98] R. Gallino, C. Arlandini, M. Busso, M. Lugaro, C. Travaglio, O. Straniero, A. Chieffi, and M. Limongi, The Astrophysical Journal **497** (1998) 388.

[Gal05] R. Gallino, 2005, private communication.

[Gle85] Y. M. Gledenov, Y. P. Popov, and V. I. Salatsky, Z. Phys. A - Atoms and Nuclei **322** (1985) 685.

[Goe01] G. Goeminne, *Investigation of the (n,p) and (n,α) reactions on ^{36}Cl, ^{37}Ar and ^{39}Ar and their astrophysical relevance*, Ph.D. thesis, Vakgroep Subatomaire en Stralingsfysica, Universiteit Gent, 2001.

[Gon97] J. Gonzales, C. Bastian, S. de Jonge, and K. Hofmans, *Modular MultiParameter Multiplexer MMPM. Hardware Description and User Guide*, 1997, IRMM Internal Report GE/R/INF/06/97.

[Gor] S. Goriely, http://www-astro.ulb.ac.be/Html/ncap.html.

[Gre99] V. Gressier, Ph.D. thesis, CEA, 1999.

[Gri03] J. Gribbin, *Science a History*, Penguin Books, London, 2003.

[Hau52] W. Hauser and H. Feshbach, Phys. Rev. A **87** (1952) 366.

[Hei03] M. Heil, *Synthesis of Trans-Iron Elements*, 2003, Invited Talk on Second European Summer School on Experimental Nuclear Astrophysics, Santa Tecla (Italy).

[Hey99] K. Heyde, *Basic Ideas and Concepts in Nuclear Physics*, second ed., Institute of Physics Publishing, Bristol and Philadelphia, 1999.

[How72] W. M. Howard, W. D. Arnett, D. D. Clayton, and S. E. Woosley, The Astrophysical Journal **175** (1972) 201.

[Ing97] C. Ingelbrecht, A. Moens, R. Eykens, and A. Dean, Nucl. Instr. & Meth. in Physics Research A **397** (1997) 34.

[Ing99] C. Ingelbrecht, J. Ambeck-Madsen, K. Teipel, P. Robouch, G. Arana, and S. Pomme, Nucl. Instr. & Meth. in Physics Research A **438** (1999) 36.

[Ing02] C. Ingelbrecht, A. Moens, J. Wagemans, B. Denecke, T. Altzitzoglou, and P. Johnston, Nucl. Instr. & Meth. in Physics Research A **480** (2002) 114.

[jef] http://www.nea.fr/html/dbdata/JEFF.

[jen] http://wwwndc.tokai-sc.jaea.go.jp/jendl/jendl.html.

[Käp82] F. Käppeler, H. Beer, K. Wisshak, D. D. Clayton, R. L. Macklin, and R. A. Ward, The Astrophysical Journal **257** (1982) 821.

[Käp89] F. Käppeler, H. Beer, and K. Wisshak, Rep. Prog. Phys. **52** (1989) 945.

[Kar03] A. I. Karakas and J. C. Lattanzio, *Mg and Al Yields from Low and Intermediate Mass AGB stars*, Proceedings of the Carnegie Observatories Centennial Symposium IV on the Origin and Evolution of the Elements, Pasadena, 2003.

[Kau99] W. J. Kaufmann and R. A. Freedman, *Universe*, fifth ed., W. H. Freeman and Company, New York, 1999.

[Kav] R. Kavanagh, private communication.

[Kno89] G. F. Knoll, *Radiation Detection and Measurement*, second ed., John Wiley & Sons, Singapore, 1989.

[Koe93] P. E. Koehler, S. M. Graff, H. A. O'Brien, Yu M. Gledenov, and Yu P. Popov, Phys. Rev. C **47** (1993) 2107.

[Koe97] P. E. Koehler, R. W. Kavanagh, R. B. Vogelaar, Yu M. Gledenov, and Yu P. Popov, Phys. Rev. C **56** (1997) 1138.

[Lan58] A. M. Lane and R. G. Thomas, Reviews of Modern Physics **30** (1958) 257.

[Lar03] N. M. Larson, *Updated Users' guide for SAMMY: Multilevel R-Matrix Fits to Neutron Data Using Bayes' Equation*, July 2003, ORNL/TM-9179/R6 ENDF-364.

[Lat] J. C. Lattanzio and C. A. Frost, *The Asymptotic Giant Branch*, Proceedings of IAU Symposium 189 on Fundamental Stellar Properties: The Interaction between Observation and Theory, Sydney, January 1997.

[Lat02] J. C. Lattanzio, New Astronomy Reviews **46** (2002) 469.

[Led78] C. M. Lederer and V. S. Shirley, *Table of Isotopes*, seventh ed., Wiley, New York, 1978.

[Mac65] R. L. Macklin and J. H. Gibbons, Reviews of Modern Physics **37** (1965) 166.

[Mah84] W. A. Mahoney, J. C. Ling, W. A. Wheaton, and A. S. Jacobson, The Astrophysical Journal **286** (1984) 578.

[Mau96] R. Mauersberger, C. Henkel, N. Langer, and Y.-N. Chin, Astron. & Astrophys. Letters **313** (1996) L1.

[Mau04] R. Mauersberger, U. Ott, C. Henkel, J. Cernicharo, and R. Gallino, Astron. & Astrophys. **426** (2004) 219.

[Mei70] R. J. Meijer and J. J. M. Van Gasteren, Nucl. Phys. A **148** (1970) 62.

[Mey93] G. Meynet and M. Arnould, *Wolf-Rayet Stars as Generators of* ^{26}*Al*, Origin and Evolution of the Elements, Paris , France, 1993, p. 539.

[Mow98] N. Mowlavi, *Nucleosynthesis in Low- and Intermediate-Mass Stars: An Overview*, Tours Symposium on Nuclear Physics III, AIP Conf. Proc. 425, 1998, p. 507.

[Mox91] M. C. Moxon and J. B. Brisland, *GEEL REFIT, A least squares fitting program for resonance analysis of neutron transmission and capture data computer code*, 1991, AEA-InTec-0630, AEA Technology.

[Mox05] M. Moxon, 2005, private communication.

[Mug81] S. F. Mughabghab, M. Divadeenam, and N. E. Holden, *Neutron Cross Sections*, Academic Press, New York, 1981.

[neu] http://www-outreach.phy.cam.ac.uk/camphy/neutron/neutron_index.htm.

[Noo84] G. J. L. Nooren and C. van der Leun, Nucl. Phys. A **423** (1984) 197.

[Obe97] U. Oberlack, *On the nature of Galactic* ^{26}*Al Sources - Investigation of the 1.8 MeV Sky with COMPTEL*, Ph.D. thesis, Technische Universität München, 1997.

[Rai93] C. M. Raiteri, R. Gallino, M. Busso, D. Neuberger, and F. Käppeler, The Astrophysical Journal **419** (1993) 207.

[Rat04] U. Ratzel, C. Arlandini, F. Käppeler, A. Couture, M. Wiescher, R. Reifarth, R. Gallino, A. Mengoni, and C. Travaglio, Phys. Rev. C **70** (2004) 065803.

[Rau] T. Rauscher, http://quasar.physik.unibas.ch/∼tommy/reaclib.html.

[Rau97] T. Rauscher, F.-K. Thielemann, and K.-L. Kratz, Phys. Rev. C **56** (1997) 1613.

[Rei00] R. Reifarth, K. Schwarz, and F. Käppeler, The Astrophysical Journal **528** (2000) 573.

[Rho86] R. Rhodes, *The Making of the Atomic Bomb*, Touchstone, Simon & Schuster Inc., New York, 1986.

[Rol88] C. E. Rolfs and W. S. Rodney, *Cauldrons in the Cosmos*, University of Chicago Press, Chicago, 1988.

[Ros49] B. B. Rossi and H. H. Staub, *Ionization Chambers and Counters*, McGraw-Hill Book Company Inc., New York, 1949.

[Sal81] J. M. Salomé and R. Cools, Nucl. Instr. & Meth. **179** (1981) 13.

[Sal86] J. M. Salomé, Physicalia magazine **8** (1986) 261.

[Sat90] G. R. Satchler, *Introduction to Nuclear Reactions*, second ed., Macmillan Education LTD, 1990.

[Sch95] H. Schatz, S. Jaag, G. Linker, R. Steininger, F. Käppeler, P. E. Koehler, S. M. Graff, and M. Wiescher, Phys. Rev. C **51** (1995) 379.

[Ske87] R. T. Skelton, R. W. Kavanagh, and D. G. Sargood, Phys. Rev. C **35** (1987) 45.

[Sow88] M. G. Sowerby and F. Corvi, *Matters Related to the NEANDC Task Forces on* ^{238}U *and* ^{56}Fe *Resonances*, Proc. Int. Conf. Nuclear Data for Science and Technology, MITO, Japan, 1988, p. 37.

[Str95] O. Straniero, R. Gallino, M. Busso, A. Chieffi, C. M. Raiteri, and M. Limongi, The Astrophysical Journal Letters **440** (1995) L85.

[Str05] O. Straniero, R. Gallino, and S. Cristallo, Nucl. Phys. A (2005), in press.

[tde] http://www.qivx.com/ispt/ptw_st.php.

[Tra86] H. P. Trautvetter, H. W. Becker, U. Heinemann, L. Buchmann, C. Rolfs, F. Käppeler, M. Baumann, , H. Freiesleben, H. J. Lütke-Stetzkamp, P. Geltenbort, and F. Gönnenwein, Z. Phys. A - Atomic Nuclei **323** (1986) 1.

[Tro85] D. Tronc, J. M. Salomé, and K. H. Böckhoff, Nucl. Instr. & Meth. **228** (1985) 217.

[Ver90] F. Verhaeghen, *Studie en ontwikkeling van een multiparameterdetectiesysteem in het kader van het ternair-fissie-onderzoek*, Master's thesis, Faculteit toegepaste wetenschappen, Universiteit Gent, 1990.

[Vod96] A. N. Vodin, A. S. Kachan, V. M. Mishchenko, and R. P. Slabospitsky, Bulletin of the Russian Academy of Sciences: Physics **60** (1996) 1821.

[Wag89] C. Wagemans, Nucl. Instr. & Meth. in Physics Research A **282** (1989) 4.

[Wag94] C. Wagemans, P. Schillebeeckx, H. Weigmann, and S. Druyts, Proceedings of the 8th International Symposium on Capture Gamma-Ray Spectroscopy and Related Topics, Fribourg, Switzerland, 1994, p. 638.

[Wag96] C. Wagemans, R. Bieber, and P. Geltenbort, Phys. Rev. C **54** (1996) 389.

[Wag98] C. Wagemans, R. Bieber, H. Weigmann, and P. Geltenbort, Phys. Rev. C **57** (1998) 1766.

[Wag00] J. Wagemans, *Study of the (n,p) and (n,α) reactions on ^{14}N, ^{17}O and ^{26}Al*, Ph.D. thesis, Vakgroep Subatomaire en Stralingsfysica, Universiteit Gent, 2000.

[Wag01] J. Wagemans, C. Wagemans, G. Goeminne, P. Geltenbort, and A. Moens, Nucl. Phys. A **696** (2001) 31.

[Was05] G. J. Wasserburg, M. Busso, R. Gallino, and K. M. Nollett, Nucl. Phys. A (2005), in press.

[Wei] H. Weigmann, private communication.

[Zei88] M. Zeilik, *Astronomy, The Evolving Universe*, sixth ed., John Wiley & Sons, Inc., 1988.

[Zie] J. F. Ziegler, http://www.srim.org.

Samenvatting

Tijdens een mensenleven, dat gekenmerkt wordt door geboren worden, verouderen en sterven, zijn de sterren duidelijk en onbetwistbaar aanwezig aan de hemel. Het lijkt alsof ze er altijd al geweest zijn en er voor eeuwig zullen blijven. Al sinds ons bestaan vragen we ons af waar we vandaan komen en wat ons lot is. Zo ontstonden de scheppingsverhalen. Geen enkel scheppingsverhaal echter vertelt, verklaart of vermeldt het begin van het heelal en het ontstaan van de elementen waaruit wij allen zijn opgebouwd. Een antwoord op deze vragen wordt gegeven in de nucleaire astrofysica. Dit is een samensmelting van twee takken van de wetenschap: de astrofysica en de kernfysica. Het eerste beschrijft de immens grote structuren en eigenschappen van het heelal terwijl de kernfysica zich bezighoudt met de beschrijving van de allerkleinste deeltjes en hun onderlinge wisselwerking. Het ontstaan van de elementen, ook wel nucleosynthese genoemd, werd pas een halve eeuw geleden verklaard en vandaag de dag is het algemeen aanvaard dat ze worden aangemaakt via kernreacties in het binnenste van sterren. Toch verklaart dit nucleosyntheseproces nog niet volledig de waargenomen abundanties van bepaalde elementen. Nucleosyntheseberekeningen steunen op een netwerk van kernreacties. Bij deze berekeningen is het van groot belang de snelheid van deze kernreacties onder welbepaalde stellaire omstandigheden, zoals druk, temperatuur en dichtheid, te kennen. De reactiesnelheid wordt dan weer berekend door reactie werkzame doorsnedes te bepalen in een bepaald energiegebied. Wanneer geen experimentele gegevens voorhanden zijn, wordt een beroep gedaan op theoretisch bepaalde waarden. De theoretisch bepaalde werkzame doorsnedes leveren doorgaans goede resultaten; voor lichte kernen echter zijn ze minder betrouwbaar.

Daarom levert dit werk experimenteel bepaalde reactie werkzame doorsnedes voor door neutronen geïnduceerde reacties op de lichte kernen ^{26}Al, ^{36}Cl en ^{41}Ca bij relevante stellaire temperaturen. Bovendien zijn deze reacties van belang bij het ontstaan of bij de afbraak van twee astrofysisch interessante isotopen, namelijk ^{36}S en ^{26}Al. Daarmee levert dit werk een bijdrage tot het oplossen van bepaalde astrofysische vraagstukken over het ontstaan van de elementen.

Na een korte inleiding over de ontdekking van het neutron wordt in een eerste hoofdstuk een theoretische achtergrond gegeven over door neutronen geïnduceerde reacties. Vertrekkend van de onafhankelijkheidshypothese, gepostuleerd door Bohr in 1936, wordt een uitdrukking opgesteld voor de differentiële werkzame doorsnede voor door neutronen geïnduceerde reacties. Deze wordt de Breit-Wigner formule genoemd en beschrijft het typisch resonant verloop voor de werkzame doorsnede van zo'n reactie. De resonanties komen overeen met de tussenkern (X+n) die gevormd wordt tijdens een reactie X(n,b)Y. De eigenschappen van de gevormde tussenkern zoals resonantieënergie, spin en (partiële) niveaubreedte(s), zitten vervat in de Breit-Wigner formule. Het eerste hoofdstuk wordt afgesloten met de introductie van het begrip Maxwelliaans gemiddelde werkzame doorsnede, kortweg MACS. Deze is evenredig met de reactiesnelheid en dus belangrijk in nucleosynthesenetwerkberekeningen. Er wordt aangetoond hoe de MACS kan berekend worden uit de experimenteel bepaalde reactie werkzame doorsnede.

Het volgend theoretisch hoofdstuk is volledig gewijd aan het belang van de bestudeerde reacties voor de astrofysica. Er wordt gestart met een algemeen overzicht van de stellaire nucleosynthese, waarna het s-proces onder de loep wordt genomen. Tijdens het s-proces worden een groot deel van de elementen zwaarder dan ijzer gevormd door een opeenvolging van door neutronen geïnduceerde reacties en β-verval. Hoewel de elementen lichter dan ijzer normaal gevormd worden tijdens de thermonucleaire verbrandingsfasen in een ster, worden sommige neutronenrijke elementen door deze reacties overgeslagen. Eén van die elementen is ^{36}S. Doordat ^{36}S zo neutronenrijk is, wordt het s-proces naar voor geschoven als mogelijke kandidaat om de oorsprong van ^{36}S te verklaren. Om dit na te gaan zijn nucleosynthesenetwerkberekeningen nodig in het massagebied $28 \leq \mathrm{A} \leq 42$. Zoals vermeld in het begin van deze samenvatting vereisen deze berekeningen MACS waarden bij bepaalde stellaire temperaturen. De bestudeerde reacties ^{36}Cl(n,p)^{36}S, ^{36}Cl(n,α)^{33}P en ^{41}Ca(n,α)^{38}Ar spelen een rol in deze netwerkberekeningen.
Een tweede actueel thema in de astrofysica is het ontstaan van ^{26}Al in de melkweg, daar dit informatie kan geven over de evolutie van de melkweg, over het ontstaan van het zonnestelsel en tevens over stellaire nucleosynthese. Dit alles wordt uitvoerig besproken in dit werk. Tot op heden zijn er vele mogelijke astrofysische scenario's voorgesteld voor het ontstaan van ^{26}Al. Onlangs werden

Asymptotic Giant Branch (AGB) sterren als voornaamste aanmakers van ^{26}Al gekatalogeerd. Dit zijn zware sterren op het einde van hun leven, die een zeer rijke nucleosynthese doormaken. Doch om de waargenomen abundantie van ^{26}Al goed te begrijpen, is het van essentieel belang de afbraakmechanismen goed te kennen, want indien ^{26}Al op een bepaalde plaats efficiënt wordt aangemaakt en de stellaire temperatuur op dat moment of in een volgende fase net goed is om de afbraakreacties in gang te zetten, zal niet veel ^{26}Al overblijven. In dit opzicht is de kennis van door neutronen geïnduceerde reacties op ^{26}Al van groot belang. In dit werk werd de ^{26}Al(n,α)^{23}Na reactie onderzocht.

Het tweede deel van dit werk omvat het voornaamste gedeelte, namelijk de bepaling van door neutronen geïnduceerde reactie werkzame doorsnedes op ^{26}Al, ^{36}Cl en ^{41}Ca. Om deze te bepalen is een neutronenbron nodig, die neutronen uitzendt in een breed energiegebied, daar het de bedoeling is de werkzame doorsnede in functie van de neutronenenergie te bepalen. De metingen besproken in dit werk zijn alle uitgevoerd aan de lineaire elektronenversneller GELINA van het Instituut voor Referentiematerialen en -metingen (IRMM) te Geel, België. Deze produceert gepulste neutronenbundels. De GELINA faciliteit wordt gekenmerkt door zijn uitstekende energieresolutie en door zijn mogelijkheid om meerdere experimenten tegelijkertijd uit te voeren. GELINA beschikt immers over twaalf verschillende vluchtpaden met variërende vluchtpadlengte. Afhankelijk van de repetitiefrequentie van de linac, 1 Hz tot 800 Hz, en van de gekozen vluchtpadlengte hebben de uitgestuurde neutronen, na moderatie, een energie gaande van enkele meV tot enkele MeV. Om de energie te bepalen van een interagerend neutron wordt een beroep gedaan op vluchttijdsmetingen. Uit de tijd die een neutron nodig heeft om de gekende afstand af te leggen tussen zijn aanmaakpositie en de plaats waar het gedetecteerd wordt, wordt zijn overeenkomstige energie berekend met de klassieke formule $E_n = \frac{1}{2}\, m_n\, v^2 = \frac{1}{2}\, m_n \left(\frac{L}{t}\right)^2$. In principe wordt het reactieproduct b uit X(n,b)Y gedetecteerd, daar het neutron zelf niet kan gedetecteerd worden omdat het gereageerd heeft met de kernen op het meetplaatje. De detectie van b zorgt dan voor het stopsignaal. Uit de formule blijkt dat de keuze van de vluchtpadlengte zeer belangrijk is voor vluchttijdsmetingen. Niet alleen wordt het bereikte neutronenenergiegebied groter bij langere vluchtpaden, ook de energieresolutie (dE$_n$/E$_n$) wordt beter naarmate het vluchtpad langer wordt. Zoals gewoonlijk is er echter een keerzijde aan de medaille, want de neutronenflux varieert met $\frac{1}{L^2}$. Daardoor zal dus altijd een compromis moeten gevonden

worden tussen het energiebereik, de energieresolutie en de neutronenflux die men wil verkrijgen bij een experiment.
De geladen deeltjes, protonen en α-deeltjes in dit werk, werden dus gedetecteerd. Daarvoor werd voor alle experimenten een ionisatiekamer gebruikt die uitgerust is met een Frisch rooster. De noodzaak van dit rooster wordt uitgelegd in dit werk. Tevens wordt dieper ingegaan op de afstelling van de ionisatiekamer zoals gasdruk, hoogspanning en afstand tussen de platen, opdat deze optimaal zou functioneren.
Verder wordt een uitdrukking opgesteld voor de experimentele bepaling van de differentiële werkzame doorsnede en worden de mogelijke oorzaken van de experimentele verbreding van een resonantie behandeld. Er wordt uitgelegd hoe deze experimentele verbreding bepaald kan worden en hoe ze in rekening moet worden gebracht bij het bepalen van de natuurlijke breedte van een resonantie.
Als laatste punt bij de algemene situering en beschrijving van de uitgevoerde metingen wordt kort ingegaan op de bereiding van de meetplaatjes en de bepaling van het aantal aanwezige atomen.

In de volgende en tevens laatste hoofdstukken worden de uitgevoerde metingen behandeld. De ^{26}Al(n,α)^{23}Na reactie is de eerste reactie die besproken wordt. Er wordt uitvoerig uiteengezet hoe de door neutronen geïnduceerde werkzame doorsnede stap voor stap bepaald werd. In het energiegebied van 1 keV tot 45 keV werden vier resonanties waargenomen, waar voordien slechts (n,α) gegevens voor één enkele resonantie beschikbaar waren. In een eerste stap om de fysische eigenschappen van deze resonanties te bepalen, werden de resonanties gefit met Voigtfuncties. Dit zijn curves die samengesteld zijn uit een Breit-Wignergedeelte en een Gaussisch gedeelte. De Breit-Wignervorm beschrijft de natuurlijke breedte terwijl de Gausscurve de experimentele verbreding, hierboven vermeld, in rekening brengt. Zo'n Voigtfit levert de energiepositie, de oppervlakte en de natuurlijke breedte van de resonantie op. Deze werden vergeleken met waarden uit de literatuur. Om de partiële breedtes alsook de spin van een gevormde tussenkern te bepalen, wordt een beroep gedaan op fitprocedures zoals REFIT. In het geval van de ^{26}Al(n,α)-meting echter waren niet voldoende gegevens voorhanden om een éénduidige oplossing te vinden voor het bepalen van de spin en de partiële breedtes. Daarom is geen fitprocedure uitgevoerd. Toch is er een poging gedaan om de spin via theoretische berekeningen te bepalen. De resultaten moeten echter met grote voorzichtigheid aangenomen worden, daar in dit geval de eigenschappen van één specifieke resonantie vergeleken werden met gemiddelde waarden, gebaseerd op theoretisch bepaalde niveaudichtheden over een breed energiegebied. Uit de bepaalde werkzame doorsnede werden tenslotte de MACS waarden berekend. Ze werden vergeleken met waarden uit de literatuur en met theoretisch bepaalde waarden. Uit deze MACS waarden blijkt dat de ^{26}Al(n,α)-reactie inderdaad zorgt voor een sterke afbraak van het aangemaakt ^{26}Al in AGB sterren.

Vervolgens worden de ^{36}Cl(n,p) en ^{36}Cl(n,α) metingen besproken. Deze werden uitgevoerd aan een langer vluchtpad, waardoor de werkzame doorsnede kon bepaald worden tot ongeveer 250 keV. Er werden achttien resonanties waargenomen, waarvan de meeste nog nooit eerder geobserveerd werden. Bovendien bleek enkel de laagst energetische resonantie een α-bijdrage te vertonen van 76%. De zeventien andere resonanties bleken gedomineerd te zijn door de (n,p) reactie. Opnieuw werden, waar mogelijk, de resonanties gefit met Voigtcurves, waardoor de natuurlijke breedte en de oppervlakte van de resonanties bepaald konden worden. Nadat de MACS waarden uit de bekomen werkzame doorsnede berekend en vergeleken werden met andere experimentele en theoretische waarden, werd de invloed van deze bijgewerkte MACS waarden op de aanmaak van ^{36}S onder de loep genomen. De MACS waarden bekomen in dit werk bevestigen dat ^{36}S hoofdzakelijk aangemaakt wordt tijdens het ‘zwakke’ s-proces. Dit proces doet zich voor in zware sterren tijdens de He-kernverbranding gevolgd door de C-schilverbranding.

De laatste bepaalde werkzame doorsnede is deze voor de ^{41}Ca(n,α)^{38}Ar reactie. Deze werd opgemeten op hetzelfde korte vluchtpad als de ^{26}Al(n,α)^{23}Na meting. Daardoor kon een neutronenenergiegebied bestreken worden van enkele honderden eV tot ongeveer 45 keV. Deze meting werd nog nooit eerder gerapporteerd. De waargenomen ^{41}Ca(n,$\gamma\alpha_0$)-reacties tijdens de thermische metingen aan het ILL in Grenoble konden bevestigd worden in het resonantiegebied. De gevonden resonanties werden opnieuw gefit met Voigtfuncties. Voor de meeste resonanties werd, naast de oppervlakte en de totale breedte van de resonanties, ook de spin en een waarde voor de verhouding van Γ_n op Γ_p bepaald. Tenslotte werden de MACS waarden berekend. Om de resolutie van de twaalf gevonden resonanties te verbeteren en vooral om een groter energiegebied te bestrijken wordt een bijkomende meting op een langer vluchtpad gepland. Hierdoor werden de berekende MACS waarden nog niet gebruikt in nucleosynthesenetwerken. Toch blijkt nu al door de hoge MACS waarden dat de ^{41}Ca(n,α)^{38}Ar reactie niet te verwaarlozen zal zijn in de zoektocht naar de oorsprong van ^{36}S.